APPENDIX:

ROADS TO REMOVAL: OPTIONS FOR CARBON DIOXIDE REMOVAL IN THE UNITED STATES

Table of Contents

APPENDIX—CHAPTER 1

This paper intentionally left blank.

APPENDIX—CHAPTER 2

Forest Management Options for CO_2 Removal

There is a wide range of forest management practices that could increase forest CO_2 removal rates (**Table A2-1**). Some practices may have increased benefits, for carbon and other services that forests provide to humans, depending on the forest type and hence specific region of the United States. Professional foresters should always be involved in writing forest management plans and assisting in selecting regionally appropriate forest management treatments.

Table A2-1. Management practices and benefits.

Management Practice	Target Forests	Considerations
Extended Rotation: Lengthening the total time between harvests	Forest Type: Commercial forests (natural and plantation) currently managed for timber production Ownership & Region(s): Private, corporate forestland owners in northern New England, Pacific Northwest, or Southeast	Potential increased revenue for larger, more valuable timber; Risks of lost revenue if forest is disturbed during deferral period; Risk of "leakage" harvesting activities on other forested land to make up for lost wood production in deferral years; Potential for increased, longer-lived wood products.
Release Treatments: Cutting or treating shrubs that can suppress regeneration; or vines that can "suffocate" the canopy of mature forests	Forest Type: Urban, riparian, and agricultural forest fragments that are repeatedly disturbed and/or "high-graded" for timber, which is preferential harvest for valuable trees without regard for the residual forest Ownership & Region: Primarily private or municipal land in eastern North America	Potential release of successional development; Increased sequestration of carbon from higher growth rates.
Low Thinning: Removing some trees from forest to reduce total tree density, which can alleviate competition among trees and increase remaining tree growth rates and Crown Thinning: Removing some trees from the forest canopy that are usually of the same species as the remaining canopy trees to alleviate over-stocking, increase individual tree	Forest Type: Natural forests that are considered 'over-stocked' for their growing region Ownership & Regions: Most of the dry western United States forests are considered overstocked, and most of this land is owned by Federal agencies Forest Type: Natural, even-aged second growth forests comprising stratified mixed species growing at different rates Ownership & Regions: Most hardwood and mixed-wood forests of eastern US that are privately owned and that originate from	Potential revenue or additional carbon benefits if low-valued, thinned trees have available market for biomass; Low thinning/removing smaller trees making up the subcanopy and understory can reduce fuel loads for forests with high wildfire risk, potentially reducing the impact of wildfires on remaining forest trees; Potential increased revenue from remaining trees that can produce higher-quality dimensional timber or can store carbon for longer periods of time within a more vigorous forest capable of greater stability with abiotic disturbances and greater endurance to stresses from insects and disease.

vigor and reduce self-thinning processes; and to accelerate succession and increase tree size	agricultural cessation or heavy exploitive cutting in the early part of the past century	
Multi-age Regeneration* Treatments: Regeneration practices that leave mature standing trees within a harvested forest as seed and shelter sources for new forest trees and to increase the age, composition, and structural diversity of the future forest at the site (*also referred to as "partial harvests" or "uneven-aged management" in the literature)	Forest Type: Non-commercial or commercial forests in regions with existing timber infrastructure and economic markets (wood mills, logging companies, etc.) Ownership & Regions: Generally, privately owned forests in the eastern US or Pacific Northwest that are monodominant and/or even-aged—often second growth native forests or plantations—to create multi-aged forests	In regions with high-development pressure for commercial or residential properties, sustainable logging income could keep landowners from selling forestlands for development of other land uses; Greater composition, structure, and age-class diversity can provide increased resilience to abiotic and biotic stressors, in some circumstances; Not all forestlands should be or would need to be managed for timber. Management may not be appropriate for forests currently managed for specific biodiversity needs, cultural values, or other ecosystem services that could be compromised by tree harvest and removal.
Best Management Practices for Harvest: Specific logging practices that reduce damage to remaining trees in logged forest, minimize soil disturbance, and retain 'coarse woody debris' including tree stumps, downed trees, and snags through careful planning of operations	Forest Type: Any forest harvested for timber	These best practices should be implemented in all forest management and logging operations, with enforcement and accreditation as combined tools that already protect and increase carbon, being expanded to all operations; Most states have their own regulatory and voluntary guidelines specific to forest management in that state, but they are developed to different extents.
Tree Planting: Planting new trees within existing forestlands to increase the total CO_2 removal capacity of existing forestlands	Forest Type: Any forestland identified as 'understocked' or poorly stocked. A higher proportion of forestland is understocked in the Pacific Northwest and southeastern United States (see Domke et al. 2020 [63] for detailed map of forest stocking densities)	Adding (or removing) trees from a forest should be done in consultation with a professional forester to determine target stocking densities. Determining the 'correct' stocking density for a given forest stand is influenced by environmental and ecological conditions, as well as human decisions on what services they wish to prioritize—such as different types of biodiversity, timber production, or aesthetics—from a given forest; Understocked and overstocked forests can both lead to unhealthy forests, decreased forest resilience to natural disturbances, or lower CO_2 removal rates.

Supporting Information for Section 3.1: Reforestation and Afforestation with Southeastern Pine Plantations

We used a multi-scale dynamic life cycle assessment (LCA) framework developed by [1] to quantify the net greenhouse gas emissions and carbon stock change of pine plantations over 100 years in the southern United States. This framework integrates a GIS model, forest growth model, soil organic carbon turnover model, and process-based wood product model. Different scenarios were established to explore the environmental implications of different forestry managements. The lands used for pine restoration in the southern United States are formerly forested land and challenging cropland and pastureland that were identified by earlier studies [1,2]. The original GIS data (layers of the three types of lands in 30 m resolution) were extracted from [3]. Then the original layers were downscaled from 30 m to 1 km pixels by ArcMap 10.8.1.

The loblolly pine restoration in three prominent physiographic regions in the southern United States including piedmont, upper coastal plain, and lower coastal plain was simulated at stand level by a growth and yield simulator (PMRC) [4] with varied inputs including site index, planting density, physiographic region, and other silvicultural managements for different scenarios (Table A2-2). A 25-year rotation was assumed for the commercial plantations. Due to the limited simulating time horizon (maximum 35 years) of the PMRC model, we simulated the first 35-year growth with PMRC and estimated the rest of 65 years using a 100-year tree growth curve that was previously generated by study (1) using the US Department of Agriculture Forest Service EVALIDator 2.0.3 online database [5]. Then the plantation was partitioned to living stems (above-stump stem outside-bark), living branches, living foliage, litterfall (needles and debris biomass that fall on the soil), and roots using equations from [6,7]. The carbon mass was converted from dry mass biomass by an average carbon content of 50% [8]. The GIS data for the site index of loblolly pine (base age 25) was extracted from the Gridded Soil Survey Geographic (gSSURGO) Database [9]. Detailed calculations of carbon uptakes by each part of pine plantations can be found in the previous study [1].

Table A2-2. Input variables and silvicultural managements for the forest growth and yield model (PMRC).

	Values and assumptions
Stand variables	
Physiographic regions	Piedmont/Lower Coastal Plain/Upper Coastal Plain
Site index (ft)	50–105
Stand density (trees/acre)	450 for low-density plantations/900 for high-density plantations
Planning horizon (years)	0–25 for commercial plantations/0–35 for pine restoration
Is the basal area of the stand known?	No
Thinning	
Should a thinning be included in this scenario?	Yes for commercial plantations/No for pine restoration
Thinning age (year)	10
Density removed by selective thinning (trees/acre)	50% of the total trees is for the high-density plantations
Silviculture	
Should a fertilization be included?	*Yes* for commercial plantations/*No* for pine restoration

Pounds of elemental nitrogen (lb N/acre)	193
Is phosphorus (P) included?	Yes
Year to be fertilized	10
Uncertainty range	
Forest growth uncertainty range	±15%

The forest soil organic carbon (SOC) change was modeled by RothC model [version 26.3; 10], which was run on a monthly basis for 100 years. The main inputs to the model are monthly climatic data, soil clay content, initial SOC content, and monthly carbon inputs to the soil including litterfall, uncollected harvesting residues (branches and foliage), snags, thinning residues, and roots after harvesting. The climate data is from the CRU TS 4.05 dataset [11] and the soil data are from the ISRIC-World Soil Information [12]. The modeled outputs are the annual SOC content (Mg C/ha) and annual CO_2 emissions (Mg CO_2/ha) from soil.

Forest operations for commercial plantations include site preparation, herbicide application, planting, fertilizer application, pre-commercial thinning, and clear-cut logging. Fifty percent of the snags and thinning residues were assumed to be collected for biochar production with the left 50% remaining in the soil after pre-commercial thinning. After logging, logs are transported to produce cross-laminated timber (CLT) and 50% of the harvesting residues and snags are chipped and transported to produce biochar. We assumed that after 60 years of CLT lifetime, 50% of CLT will be recycled while the remaining 50% will be landfilled. Biochar will be applied to agricultural lands as soil amendment and will be decayed very slowly. The cradle-to-grave life-cycle greenhouse gas (GHG) emissions of forest operations, CLT production and end of life (EOL), and biochar production and EOL were estimated using process- and product-based LCA models, which are documented in the previous study [1]. CLT substitution for carbon-intensive materials (e.g., concrete and steel) was also considered in the LCA model.

Supporting Information for Section 3.3: Silvicultural Forest Management of Southern New England Forests

1 Introductory Material

1.1 Forest Type Description

Oak-mixed hardwood forest is an important forest type, representing 51% of all forestlands in the United States [13,14]. Oak-mixed hardwood forests are primarily distributed east of the Connecticut river valley, including the central Massachusetts and eastern Connecticut regions, not including the montane regions (**Table A2-3**). Heavy glaciation in this subregion left a variable topography, with a network of drumlins (elongated hills formed by glacial ice), ablation till (deposits carried on or near the surface of the glacier), outwash (deposits carried by running water from melting ice), and kettle holes (depression or hole formed by retreating glacier on outwash plains). The highest elevation in this subregion is about 400 m and the lowest is about 160 m. Soils of this subregion are primarily characterized by mesic inceptisols that are fertile and acidic [15]. The species composition comprises mostly oak (*Quercus* spp.) in the canopy, red maple (*Acer rubrum*), black birch (*Betula lenta*), and sugar maple (*Acer saccharum*) in the subcanopy, and eastern white pine (*Pinus strobus*) and eastern hemlock (*Tsuga canadensis*) represented as emergent in both canopy and subcanopy; components of hickory species (*Carya* spp.); and appearances of white ash (*Fraxinus americana*) and tulip poplar (*Liriodendron tulipifera*) on mesic fertile soils.

The northern hardwood forest is largely represented west of the Connecticut river valley in the Berkshire Mountains of western Massachusetts and northwestern Connecticut and the Hudson Valley / Catskill Mountain region of New York. This subregion is an extension of the Appalachian range, with an elevation between 300 m and 600 m. The climate has cooler summers and colder winters compared to the oak-mixed hardwood forest subregion, with less common occurrences of severe tornadoes or hurricanes, but frequent microbursts in the summer. Soils of this subregion are similar to that of the oak-mixed hardwood forests, classified as inceptisols with glacial till origin, but have more wide-spread limestone elements leading to higher alkalinity. This forest type is dominated by American beech (*Fagus grandifolia*), sugar maple, white ash, eastern hemlock, yellow birch (*Betula alleghaniensis*) and red maple with presence of red spruce (*Picea rubens*), red oak, and eastern white pine.

Table A2-3 Estimated areas (thousand acres) of oak-mixed hardwood and northern hardwood forests in southern New England and New York as proportions of the total forestland in the study region (Source: USDA Forest Service EVALIDator v2.0.6 [16].

Forest Type	State	Area	Forest Type
Oak-Mixed Hardwood	Connecticut	480 ± 30	14%
	Massachusetts	526 ± 34	16%
	Southern New York	480 ± 35	14%
	Sub-Total	**1486 ± 57**	**45%**
Northern Hardwood	Connecticut	73 ± 13	2%
	Massachusetts	305 ± 25	9%
	Southern New York	757 ± 43	23%
	Sub-Total	**1135 ± 51**	**34%**
Total Forested Area		**3319 ± 61**	**100%**

1.2 Land Use and Forest Management History

Most of central and southern New England forests are second-growth forests growing on former agricultural farm and pastureland. For at least 10,000 years, indigenous people including the Algonquin peoples and the more recent Nipmuc, Pequot, and Mohegan people stewarded the forests. Land management followed an intermittent swidden agriculture style with controlled fire during this period [17]. European colonists cleared forests after their arrival in the 1700s on the richer, more fertile soils of the coastal plain and lower Connecticut river valley for agricultural and pasture grazing. European Americans abandoned their agriculture lands in the mid-nineteenth century [18]. Much of the former agricultural lands developed as old-field pine forests, which were subsequently cut in the late 1800s and early 1900s for timber. Anthropogenic disturbance, in combination with stand-replacing natural hazards such as the hurricane of 1938, led to the second-growth oak-mixed hardwoods present today. Meanwhile, northern hardwood forests on most of the remaining poorer upland soils were never converted during this process. Instead, the hemlock in these forests was extensively cut for the tanning industry and the hardwoods cut for charcoal production between 1800–1890. Some of the land was repeatedly cutover with much of the regrowth occurring between 1890–1930. Traditional timber cutting practices dominated forest management of the region until the 'industrial/service' economy transition from early 20th century. Wood product market of the region mainly involves sawtimber from sugar maple, eastern hemlock, yellow birch, red/black oak, and some softwood species such as spruce and white pine

(USFS Cut and Sold Reports [19]). Current forest management in the case region has an overall low intensity, with most of the forest lands under passive management.

1.3 Forest Ownership and Management

The forests in the region are primarily privately owned (~70%) by small holder family ownership [20, 21]. Public forestlands (~30%) are owned and managed by state and local municipalities with less than 1% federal ownership. Primary goals of private forest owners are recreation (hunting, scenery) and protection of natural resources (biodiversity, water). Timber production is lower priority for private and public owners. The New York City water authority manages forests to promote water quality, wildlife habitat, recreation, carbon, and economic benefits [22]. Massachusetts DCR manages forests for conservation, increasing resistance and resilience of trees, managing forest health and biodiversity, and maintaining and enhancing soil, water, and air resources [23].

1.4 Impact of Forest Cutting Practices

One of the most common exploitative cutting methods is selective logging, which removes all the large, valuable trees for sawtimber. In southern New England, mainly red oak, sugar maple, and black cherry are removed, while the low-value, slow-growing, less-vigorous trees such as red maple, beech, and hemlock remains. This irregular cutting produces poor growing conditions in the crowded areas of the woods, and also often promotes tree seedlings of lower economic value [24]. Silvicultural management practices, on the other hand, are often regeneration-focused, such as the shelterwood cut which is known to be successful in regenerating oak-mixed hardwoods with presence of other heavy-seeded, shade-tolerant or mid-tolerant tree species including hickory [25-28]. For northern hardwood forests, traditional silvicultural management practices for northern hardwood can vary depending upon the composition and structure desired, with options from group and patch selection systems to intense one-cut shelterwood harvest that resemble a true clearcut [29].

2 Methodology

2.1 Forest Inventory Data Description

We obtained forest inventory data from various sources. The USDA Forest Service Forest Inventory and Analysis (FIA) database [30] provides the most complete spatial coverage of forest inventory plots in Connecticut and Massachusetts. The FIA plots consist of four 24' radius subplots, on which trees larger than 5.0" diameter at breast height (DBH) are measured. A 6.8' radius microplot is nested within each subplot to measure understory seedling and sapling trees less than 5.0" DBH. The latest iteration of inventory in both Connecticut and Massachusetts happened between 2013 and 2019, with in total of 481 and 781 plots, respectively.

We obtained additional forest inventory data from the Massachusetts Department of Conservation and Recreation [31]. This data comprises state lands including state forests, parks, and reservations, covering in total 245,000 acres of forestlands. MA DCR samples forest plots at approximately one plot per 160-acre on a 10-year cycle. The CFI plots are circular fixed 0.2-acre plots with 52.7' radius, collecting overstory tree records larger than 5.6" DBH. Within each plot, four 6' radius subplots centered 26' from plot center in each cardinal directions are set up for records of sapling trees 1" – 5,5" DBH. In addition, ten 1/1000th acre plots, 10' apart, are measured for seedlings up to 1" DBH. The latest completed inventory cycle between 2010 and 2019 resulted in total of 1957 plots.

We also obtained additional forest inventory data from the New York City Department of Environmental Protection [32] that covers more than 192,000 acres of city-owned forested lands at a density of approximately one plot per 8 acres. Plots are located west of the Hudson River within the Catskill and Delaware River watersheds and east of Hudson River within the Croton watershed. We included plots within the Catskill Mountain region to characterize the northern hardwood forest type, which consists of

1989 forest stands measured during the most recent inventory period from 2010 to 2018. Areas of the forest stands ranged from 0.2–223.5 acre. Two types of plots were measured over the same location. A 1/100th acre plot measures the numbers of understory trees, including seedlings between 1.0' – 4.49' tall, small saplings with a DBH of 0.1" – 0.9", and large saplings with a DBH of 1.0" – 4.49". DBH measurements of understory trees are absent. Therefore, we manually assigned the median DBHs to the three understory categories (0.1" for seedlings, 0.5" for small saplings, and 2" for large saplings). A variable radius overstory plot measures trees larger than 5.0" DBH using 10 basal area factor (BAF) prism that records DBH of all tree records, but without height measurements.

We subset all 5,208 inventory plots by the location, forest type classification, stocking level (total basal area per acre) and species composition (number of trees per species, proportion of basal area per species). Subsetting ensured that the forest inventory plots accurately represented the two forest types of interest (oak-mixed and northern hardwood) and were therefore compatible with management scenarios that a forester would realistically prescribe for a given forest type. To subset the data, we demarcated the study region by dividing the whole area into two by the Connecticut River valley ecoregion. We defined regions west of Connecticut River valley represented northern hardwood and east regions excluding Cape Cod costal lowland and islands area represented the oak-mixed forests [33]. Second, we selected inventory plots from within each of the two forest type regions whose compositions matched the appropriate forest type group using the national forest typing algorithm [34].

We selected inventory plots that met Oak/Pine and Oak/Hickory type groups for oak-mixed hardwood, and Maple-Beech-Birch type group for northern hardwood. Next, we examined stocking level of the inventory plots by looking at the total basal area per acre. We excluded plots with total basal area less than 60 ft^2/acre or larger than 250 ft^2/acre, which could be results of inventory errors, inventory of under-stocked forest stands not ready for silvicultural treatments, or representations of rare forest stand structures (e.g., sites with the presence of large old trees with DBH>40"). Finally, we stratified the remaining inventory plots according to species composition to account for differences in stand dynamics under different soil and water conditions. We developed thresholds of number of trees in the inventory tree records and the proportion basal area per acre for the indicator species and divided the plots into 'mesic' (moist glacial till) and 'xeric' (dry skeletal soil) sites. For northern hardwood forests, we classified plots as 'mesic' if over 1/3 of the total basal area comprised sugar maple (*Acer saccharum*), white ash (*Fraxinus americana*), tulip poplar (*Liriodendron tulipifera*) and basswood (*Tilia americana*) and less than 15% of the total basal area comprised American beech (*Fagus grandifolia*). We classified all other northern hardwood plots that did not meet these criteria as 'xeric. For oak-mixed forests, we classified plots as 'mesic' plots if the inventory contained large (diameter at breast height, DBH>10") white ash and/or tulip poplar or more than two sugar maple individuals of any size. We classified all other oak-mixed plots that did not meet this criterion as 'xeric'. The stratification process resulted in 2202 remaining plots. Table A2-4 represents the detailed breakdown of number of plots per forest and site types.

Table A2-4. Number of plots per forest and site types from different data sources.

Forest Type	Site Type	Data Source	N
Northern Hardwood (N=1692)	'Mesic' (N=548)	FIA-CT	5
		FIA-MA	16
		MA-DCR	68
		NYC-DEP	459
	'Xeric'	FIA-CT	14

	(N=1145)	FIA-MA	55
		MA-DCR	306
		NYC-DEP	769
Oak-Mixed Hardwood (N=510)	'Mesic' (N=79)	FIA-CT	32
		FIA-MA	26
		MA-DCR	21
	'Xeric' (N=431)	FIA-CT	56
		FIA-MA	89
		MA-DCR	286

2.2 Forest Vegetation Simulator Model Description

We selected the Northeast variant of the US Forest Service Forest Vegetation Simulator (FVS-NE) model [35, 36] for the simulation of forest management treatments. The model has been regionally calibrated [37, 38] and extensively used by researchers and managers to summarize forest stand conditions, produce forest inventory statistics, and project future stand conditions under various management practices [39-41].

FVS is a distance-independent individual tree growth and yield model used for predicting forest stand dynamics [42]. It simulates forest growth over a user-defined time period using a standard stepwise modeling process. Users determine specific simulation parameters using two input files: (1) a forest inventory data tree record data file, which includes individual trees, the species, DBH, and tree height. The model can fill missing data on tree heights during the initial model stage using a species-specific height-diameter function; and (2) a keyword record text file that instructs modeling activities, such as describing management treatments—including the timing of harvest, the volume of trees harvested, the specific species harvested, and/or the total basal area removed or retained—including changes in tree mortality rates from disturbances, planting or natural regeneration conditions—including the number of regenerating individuals of each species, and defining output variables. Tree growth is simulated by a diameter increment model for large trees and a height increment model for small trees (threshold at DBH=5"). Stand conditions computed include the species composition, size distribution, volume, biomass and carbon of the forest stands. Volume estimation is based on the methods of the National Volume Estimator Library (NVEL) by the U.S. Forest Service [43].

We estimate biomass and carbon content using the Fire and Fuel Extension (FFE) [44]. Biomass is estimated using a combination of the NVEL (National Volume Estimator Library) biomass equations by state and species and the species group-specific allometric equations at national level by [45]. Carbon contents of 0.5 and 0.37 are applied to woody biomass (living and dead) and litter/duff biomass, respectively [46]. The model calculates standing forest carbon stocks for the following categories: total aboveground live, belowground live, belowground dead, standing dead, forest down dead wood, litter and duff, herbs and shrubs, and total removed carbon. The total removed carbon only includes the tree boles, and the model assumes 100% of the slash and leaves are left on the forest floor. The model categorizes the total removed carbon into the following four end-use categories: (1) 'products in use', which include all harvested wood products used for pulp and paper, packing materials, and furniture and building materials that are in current use and storing carbon within the product; (2) 'products in landfills', which are the same wood products that enter the waste stream and end up stored in the landfill, decompose, and emit carbon to the atmosphere at a predefined rate, depending on the product and time

in the landfill; (3) 'products burned for fuel or energy', which are harvested woody materials directly used as bioenergy, or retired wood products used for energy capture instead of going into landfill. Both lead to emissions that transfer carbon from the total removed carbon to the atmosphere; (4) 'emissions without energy capture', which are total removed carbon that emitted to the atmosphere through decay, or combustions that are not for the purpose of fuel or energy use, for example only as a way of waste disposal. The proportions of total removed carbon that goes into the four categories are based on regional estimates of transfer and decay rates that vary by region and roundwood category [46]. In the northeast, we assume 57% and 61% of the total removed carbon goes into softwood and hardwood sawlogs, respectively, and stored in products while 24% and 25% are used for fuel or energy, initially after cutting (at year zero). 26% and 18% remain in product and 16% and 24% transfer into landfill after 25 years (by 2050 in our case). Note that this is a conservative estimate, as more recent estimates showed that up to 75% of the total removed carbon becomes products in use after the cutting [47].

2.3 Model Process

We used the stratified forest inventory data as input for the FVS model simulations. We made 2025 as Year 0 and scheduled the initial management treatment to start the post-cutting simulation with five-year cycles for a total of 20 cycles. First, we simulated tree growth on each inventory plot from the year of the inventory measurement to 2025 without any human or natural disturbances to generate a unified starting point at Year 0 with all the plots that were measured at different times. Then, we started the 5-year-cycle simulations with the initial cutting practices in Year 0. In each cycle, we calculated the following metrics to track stand development: basal area per acre of the total forest stand, per tree species, and per diameter class to illustrate the changes of species composition and diameter distribution over time. We classified trees into four categories based on their DBH: small trees (DBH <5"), medium-size trees (5" ~12"), merchantable trees (12" ~ 18") and large trees (DBH >18"). We also calculated harvested merchantable trees in board feet per acre after every cutting for the accounting of economic costs and benefits. We also collected the carbon stock in all carbon pools exported by the FFE extension in every cycle. For each forest type, we modeled nine total scenarios that varied based on three stand management options and three natural disturbance scenarios, which we describe in detail below.

2.3.1 Management Treatments

In the main report, we used the terms *passive*, *exploitation-focused*, and *regeneration-focused* management. We implemented the same Diameter-Limit Timber Cut (exploitation-focused) for oak-mixed and northern hardwood forests. We used a 25-year rotation cycle and removed all merchantable trees (DBH>12") in each cutting operation. We implemented different Shelterwood Cut (regeneration-focused) for the oak-mixed and northern hardwood forest types. For the oak-mixed forest, we modeled an Irregular Shelterwood, which leaves residual trees un-uniformly in the stand to provide seedling shelters, maintain structure, and moderate microclimate. To model this practice, we used a non-uniform removal of trees with DBH between 2" and 18", and part of the large trees (DBH>18") with a residual basal area of 35 ft^2 /acre. We scheduled two Crown Thinning treatments at 55 and 80 years after the initial harvest, cutting one-third of the large trees (DBH>18"), for the purposes of reducing competition and further releasing the growth of large trees. For the northern hardwood forests, we modeled a One-cut Shelterwood harvest. To model this practice, we removed all trees with DBH >2" and did not apply any additional thinning treatments after the initial harvest.

2.3.2 Disturbances

We modeled the following three forest disturbances scenarios: (1) "No Disturbance," where tree mortality arises from aging or competition; (2) "Extreme Weather," where tree mortality arises from regularly occurring drought (every 10 years) and windstorm (every 50 years) events in the region [48]. We assumed drought increased birch (*Betula* spp.), sugar maple (*A. saccharum*), ash (*Fraxinus* spp.), and

hemlock (*Tsuga* spp.) mortality rates by 25%, and other species mortality rates by 10%. We assumed windstorms increased maple (*Acer* spp.) and hemlock (*Tsuga* spp.) mortality rates by 25% and ash, eastern white pine (*Pinus strobus*), and black birch (*Betula lenta*) by 50%. We assumed disturbances were more likely to affect large trees versus small trees and selected the 'uneven distribution of mortality rates' in FVS; (3) 'Extreme Weather, Pests, and Diseases' scenario that simulates tree mortality from three common pests and disease of northeastern United States [49] in addition to the 'Extreme Weather' assumptions. Spongy moth (*Lymantria dispar*) is a generalist pest that attacks many hardwood tree species in the region, especially oaks [50]. We also assumed higher impact on large trees which are more susceptible to defoliation. Beech leaf disease (BLD, *Litylenchus crenatae mccannii*) and emerald ash borer (EAB, *Agrilus planipennis*) are specialist pests that infect American beech and ash trees, respectively. We assumed 100% tree mortality of beech (*Fagus* spp.) and ash (*Fraxinus* spp.) trees (from BLD and EAB, respectively [51, 52]). We assumed 50% and 25% mortality rates to oak (*Quercus* spp.) and maple larger than 18" DBH, respectively. For oak and maple smaller than 18" DBH, we assumed 15% mortality.

2.3.4 Regeneration

The default regeneration structure in the FVS-NE variant is a partial-establishment stump resprout model. For this variant, the user must define seedling regeneration parameters that include the seedling species and number of individuals that recruit into the forest. We made a series of informed assumptions about the impact of management treatments on seedling and sapling development (Table A2-5) based on empirical seedling recruitment data within the study region [41, 53-56].

Table A2-5. The numbers of individual seedlings by species that we assumed recruited into mesic or xeric oak-mixed and northern hardwood forest stands after cutting in the Forest Vegetation Simulator Northeast variant model.

		Mesic		Xeric	
		Background	Shelterwood	Background	Shelterwood
Oak-mixed hardwood forest	*Northern red oak*	0	150	25	400
	Red maple	5	150	100	500
	Eastern white pine	0	10	250	500
	Black oak	0	0	25	400
	White oak	0	0	10	150
	Sweet birch	400	2500	25	150
	Scarlet oak	0	0	5	50
	American beech	50	250	0	50
	Eastern hemlock	50	300	0	0
	Paper birch	0	300	0	100
	Sugar maple	100	500	0	0
	Pignut hickory	0	0	50	250
	Shagbark hickory	15	200	5	10
	Chestnut oak	0	0	100	150
	White ash	25	300	0	0
	Black cherry	0	50	25	250
	Yellow birch	100	200	0	0
	Total	**745**	**4910**	**620**	**2960**
Northern	*American beech*	20	55	250	400
	Red maple	5	250	55	500

Sugar maple	250	750	0	10
White pine	0	20	150	400
Balsam fir	5	75	30	100
Eastern hemlock	100	200	10	50
Red spruce	50	150	10	60
Yellow birch	300	2500	10	150
Paper birch	0	500	0	350
Northern red oak	5	75	0	15
White ash	10	150	0	5
Total	745	4725	515	2040

We considered every rotation of the Diameter-Limit Timber Cut and the initial cut of the Shelterwood Regeneration Cut (excluding the two crown-thinning) as major cutting events that will introduce seedling recruitment. We also assumed that only windstorm disturbances would create gaps in the forest stand large enough for seedling recruitment (excluding drought, pests, and diseases). We assumed different numbers of seedlings per forest and site types and following different types of cutting and disturbances. We assumed a 'background regeneration' for seedling recruitment after Diameter-Limit Timber Cut and windstorm disturbances, with relatively low total number of seedlings and larger proportions of shade-tolerant species. For number of seedlings following a Shelterwood Regeneration Cut, we assumed significantly larger numbers of total seedlings, and larger proportions of shade mid-tolerant and intolerant species. In this way, we could reflect the different impact of cutting practices on forest composition and structure discussed above (Section 1.4 in this appendix).

3 Results

3.1 Forest Composition through Time: No Disturbance

Under Passive management, the forest grows with the same initial species composition until the total basal area plateaus in ca. 50 years between 180–200 $ft^2\ ac^{-1}$ (top row, **Figure A2-1a**). Exploitation-Focused Management is systematically removing the large trees and choice species [57, 58] reflected by the gradual decrease of oak from the basal area (middle row, Figure A2-1a). Regeneration-Focused Management leads to reproduction similar in species composition and basal area to Passive Management after 100 years (bottom row, Figure A2-1a). Total basal area on 'Xeric' sites reached over 200 $ft^2\ ac^{-1}$, primarily because sites with dry, well-drained, deep and sandy outwash soils have high carrying capacity [58] or the presence of evergreen pine species. The effect of oak regeneration from shelterwood cut on oak-mixed hardwood forests [59] is not prominent, perhaps because the effects of gap-creation [46] is not fully captured by the density-dependent growth and mortality functions in FVS. (Figure A2-1a).

The trajectory of forest stand composition changes under natural disturbances (**Figure A2-1b–c**). The 'Extreme Weather' scenario includes drought once in every 10 years and windstorm once in every 50 years, which represents an episodic disturbance regime with multi-decadal intervals (Figure A2-1b). Episodic drought and windstorm suppress opportunist species such as sugar maple and black birch. On 'Xeric sites, this facilitates the development of beech [60] and red maple as a slightly less drought-sensitive species [61]. On 'Mesic' sites, however, regeneration of birch trees is introduced in much higher volume, which suppresses the establishment of the more resilience species, leading to birch-dominated stands but with lower total basal area over time (Figure A2-1b).

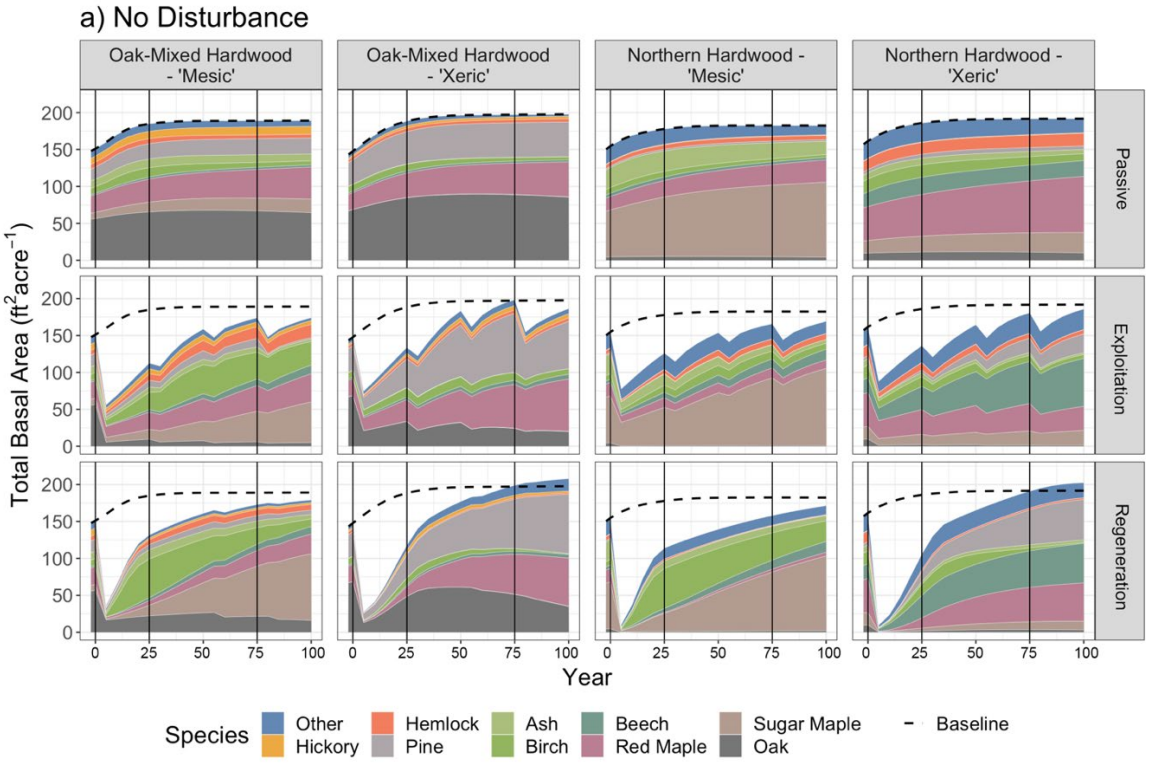

Figure A2-1a. Effect of forest cutting practices (rows) on forest species composition with different forest and site types under no simulated natural disturbances. Total live basal area reported in square feet per acre.

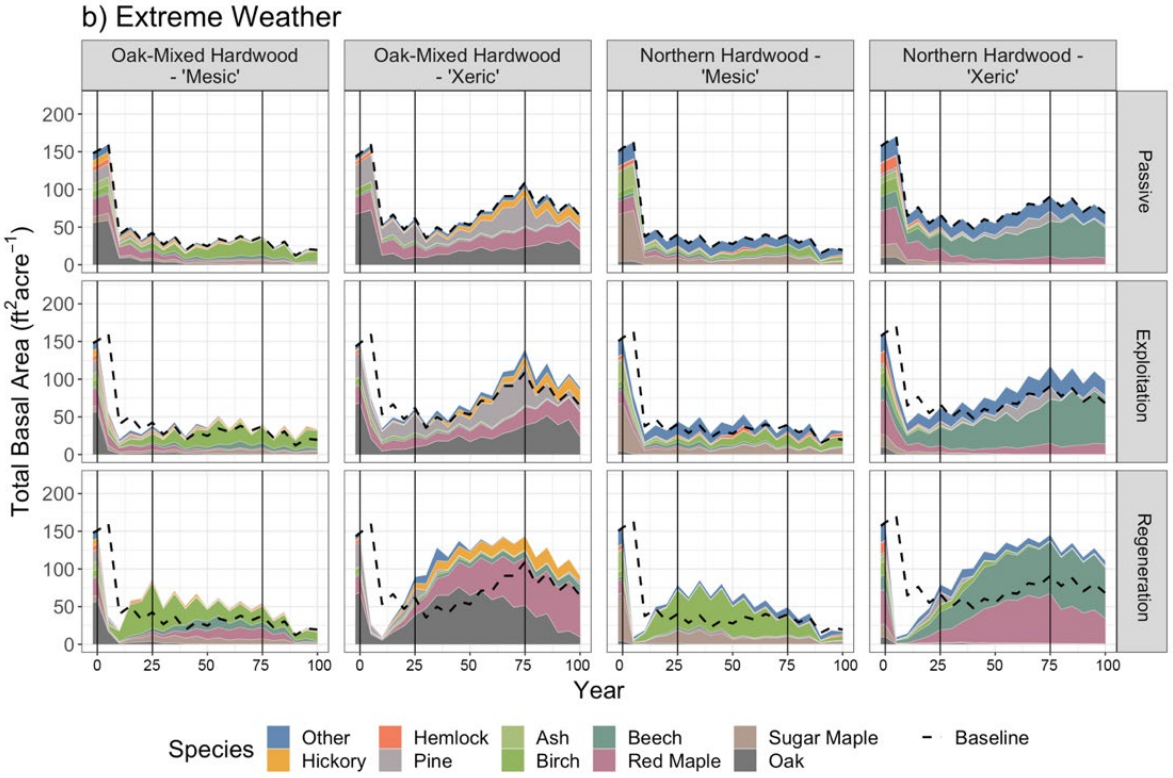

Figure A2-1b. Effect of forest cutting practices (rows) on forest species composition with different forest and site types under simulated Extreme Weather natural disturbances. Total live basal area reported in square feet per acre.

The dominance of beech and red maple is prevented by beech leaf disease and spongy moth on 'Xeric' sites in the 'Extreme Weather, Pests, and Diseases' scenario (Figure A2-1c). Hickory occupies a large share of basal area on the 'Xeric' oak-mixed hardwood forests, which could be explained by its reproductive strategy as an intermediate shade tolerant but hardy and resilient species [62]. In northern hardwood forests, absence of beech and red maple leads to the development of evergreen tree species such as spruce and fir, categorized as 'Other' in the figures. On 'Mesic' sites, birch trees become dominant because birch is competitive during early ages and is frequently present on harvested oak stands [63, 64]. This could explain the sole-dominance of birch on 'Mesic' sites under impacts from extreme weather, pests, and diseases, especially because oak and other competitors are suppressed by these disturbances.

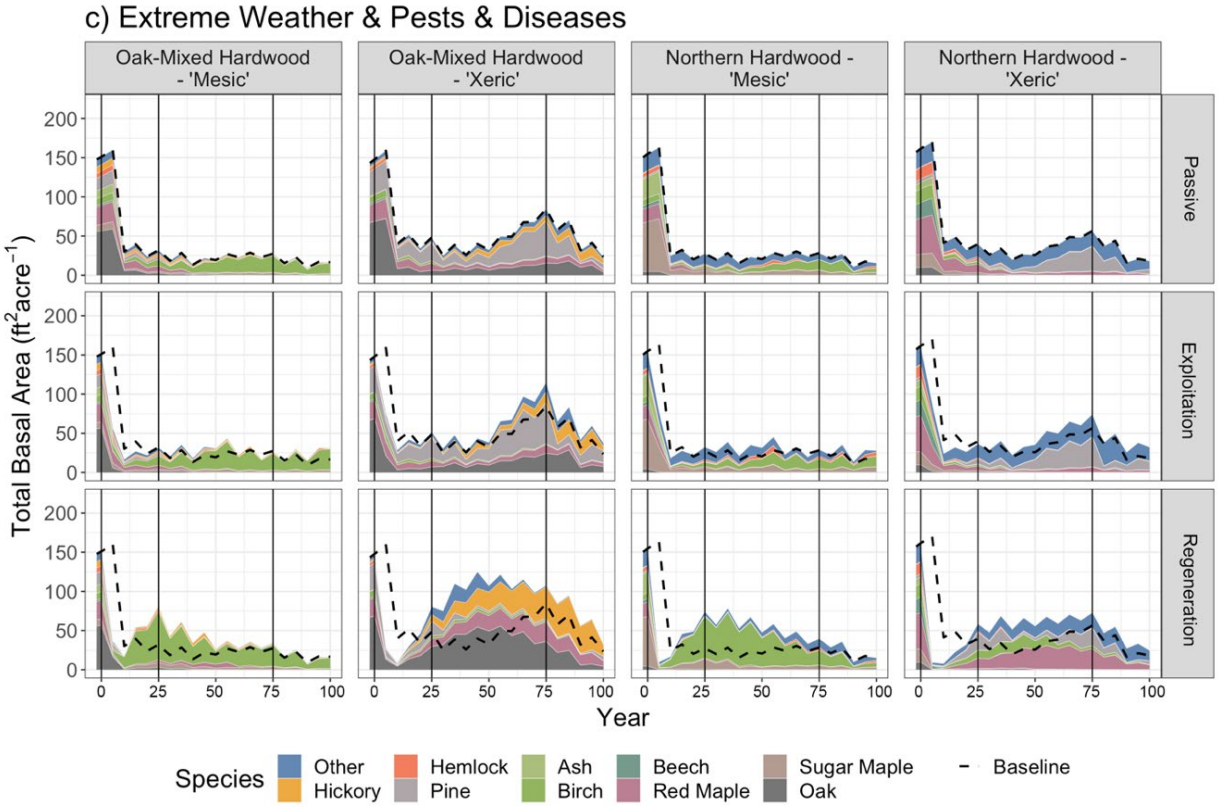

Figure A2-1c. Effect of forest cutting practices (rows) on forest species composition with different forest and site types under simulated Extreme Weather natural disturbances. Total live basal area reported in square feet per acre.

3.2 Carbon Dynamics per Forest and Site Types

Total carbon storage values differ slightly between the four forest and site types (**Figure A2-2a–c**). Differences in carbon storage under Passive Management are minimal (top rows). Under natural disturbance scenarios (**Figure A2-2b, c**), 'Xeric' sites have higher total carbon storage than 'Mesic' sites over time owing to higher total basal area of tree species such as red maple, hickory, spruce, and fir that are less susceptible to disturbances.

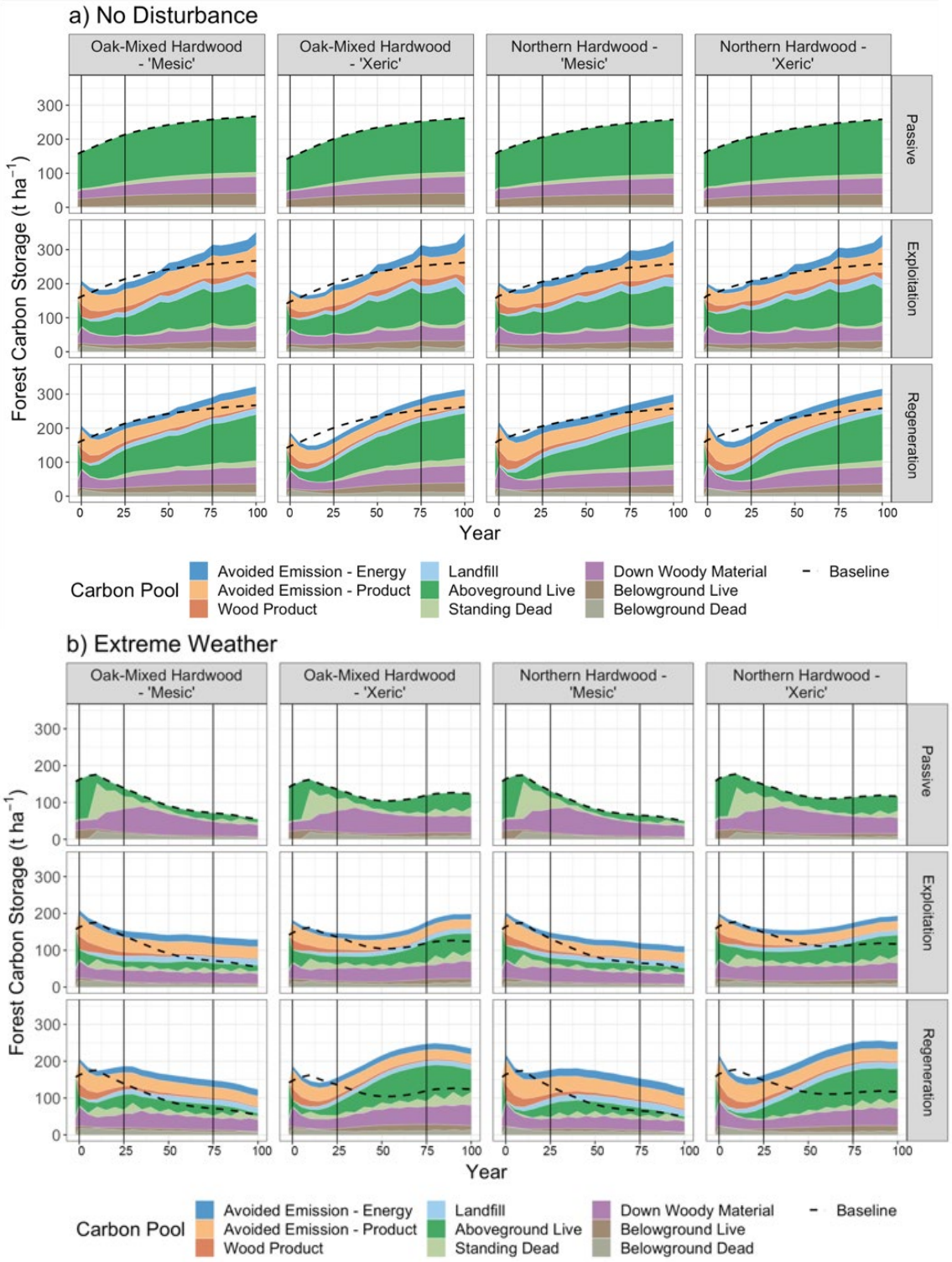
a) No Disturbance
Oak-Mixed Hardwood - 'Mesic'
Oak-Mixed Hardwood - 'Xeric'
Northern Hardwood - 'Mesic'
Northern Hardwood - 'Xeric'
Passive
Exploitation
Regeneration
Forest Carbon Storage (t ha^{-1})
Year
Carbon Pool
Avoided Emission - Energy
Avoided Emission - Product
Wood Product
Landfill
Aboveground Live
Standing Dead
Down Woody Material
Belowground Live
Belowground Dead
Baseline
b) Extreme Weather
Oak-Mixed Hardwood - 'Mesic'
Oak-Mixed Hardwood - 'Xeric'
Northern Hardwood - 'Mesic'
Northern Hardwood - 'Xeric'
Passive
Exploitation
Regeneration
Forest Carbon Storage (t ha^{-1})
Year
Carbon Pool
Avoided Emission - Energy
Avoided Emission - Product
Wood Product
Landfill
Aboveground Live
Standing Dead
Down Woody Material
Belowground Live
Belowground Dead
Baseline

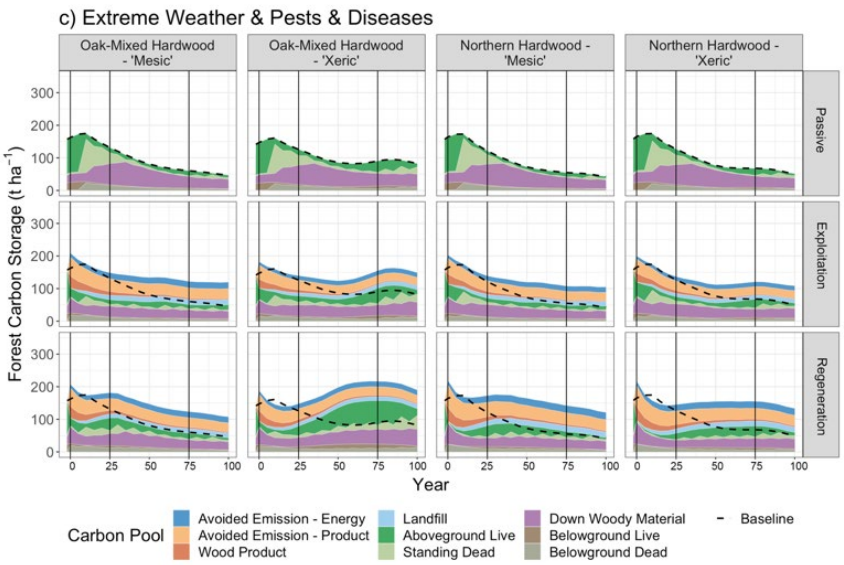

Figure A2-2. *Effect of forest cutting practices on forest carbon storage on the four forest and site types under different natural disturbance scenarios: (a) No Disturbance, (b) Extreme Weather, and (c) Extreme Weather, Pests, and Diseases.*

Figure A2-3 shows CO_2 potentials (tonnes CO_2e ha-1) of two harvest approaches, exploitation-focused and regeneration-focused, relative to a passive management approach with no harvests.

Per hectare CO_2 potential without avoided emissions					**Per hectare CO_2 potential with avoided emissions**				
	Year 25	none	EW	EWPD	Year 25		none	EW	EWPD
Exploitation-Focused	OMH	-268	-141	-130	Exploitation-Focused	OMH	-26	45	56
	NH	-218	-117	-116		NH	12	50	51
Regeneration-Focused	OMH	-241	-63	-57	Regeneration-Focused	OMH	-54	124	131
	NH	-285	-122	-104		NH	-53	110	128
	Year 75	none	EW	EWPD	Year 75		none	EW	EWPD
Exploitation-Focused	OMH	-144	60	65	Exploitation-Focused	OMH	218	226	231
	NH	-134	62	44		NH	202	211	194
Regeneration-Focused	OMH	-69	208	180	Regeneration-Focused	OMH	123	375	347
	NH	-95	204	113		NH	112	411	320
	Year 100	none	EW	EWPD	Year 100		none	EW	EWPD
Exploitation-Focused	OMH	-131	111	93	Exploitation-Focused	OMH	315	273	255
	NH	-97	104	69		NH	285	252	218
Regeneration-Focused	OMH	-5	167	145	Regeneration-Focused	OMH	197	330	308
	NH	-20	189	92		NH	181	391	293

Figure A2-3. The CO_2 potential changes by forest types (oak-mixed hardwood [OMH], northern hardwood [NH]) and disturbance regimes (no disturbance [none], extreme weather [EW], or extreme weather plus pests and disease [EWPD], and time horizons after harvest (25, 75, and 100 years). The CO2 potential is color-coded where red and orange colors indicate carbon losses and yellow and green colors indicate carbon gains with harvesting relative to no harvest.

References

1. *Zhang B, Lan K, Harris TB, Ashton MS, Yao Y. Climate-smart forestry through innovative wood products and commercial afforestation and reforestation on marginal land. Proc Natl Acad Sci. 2023 Jun 6;120(23):e2221840120*
2. *Cook-Patton SC, Gopalakrishna T, Daigneault A, Leavitt SM, Platt J, Scull SM, et al. Lower cost and more feasible options to restore forest cover in the contiguous United States for climate mitigation. One Earth [Internet]. 2020;3(6):739–52. Available from: https://doi.org/10.1016/j.oneear.2020.11.013*
3. *The Nature Conservancy. Reforestation Hub [Internet]. https://www.reforestationhub.org/.*
4. *Plantation Management Research Cooperative. PMRC Growth & Yield Simulator [Internet]. https://pmrc.uga.edu/simulator.*
5. *USDA Forest Service. U.S. Department of Agriculture Forest Service EVALIDator 2.0.3 online database, https://apps.fs.usda.gov/fiadb-api/evalidator [Internet]. 2022.*
6. *Gonzalez-Benecke CA, Gezan SA, Albaugh TJ, Allen HL, Burkhart HE, Fox TR, et al. Local and general above-stump biomass functions for loblolly pine and slash pine trees. For Ecol Manage [Internet]. 2014;334:254–76. Available from: http://dx.doi.org/10.1016/j.foreco.2014.09.002*
7. *Gonzalez-Benecke CA, Jokela EJ, Martin T a. Modeling the Effects of Stand Development, Site Quality, and Silviculture on Leaf Area Index, Litterfall, and Forest Floor Accumulations in Loblolly and Slash Pine Plantations. For Sci [Internet]. 2012 Oct 16;58(5):457–71. Available from: https://academic.oup.com/forestscience/article/58/5/457-471/4604220*
8. *James E. Smith Linda S Heath Kenneth E Skog Richard A Birdsey JE. Methods for Calculating Forest Ecosystem and Harvested Carbon with Standard Estimates for Forest Types of the United States. United States Dep Agric For Serv [Internet]. 2006; Available from: http://www.fs.fed.us/ne*
9. *Soil Survey Staff. Gridded Soil Survey Geographic (gSSURGO) Database for the Conterminous United States. United States Department of Agriculture, Natural Resources Conservation Service. Available online at: https://gdg.sc.egov.usda.gov/.*
10. *Coleman K, Jenkinson DS. RothC-26.3 - A Model for the turnover of carbon in soil [Internet]. Harpenden, UK; 2014. chrome-extension://efaidnbmnnnibpcajpcglclefindmkaj/https://www.rothamsted.ac.uk/sites/default/files/RothC_guide_WIN.pdf*
11. *Ian H, Osborn TJ, Phil J, Lis D. Version 4 of the CRU TS monthly high-resolution gridded multivariate climate dataset. 2020;1–18.*
12. *ISRIC. SoilGrids—global gridded soil information [Internet]. ISRIC-World Soil Information. [cited 2021 Oct 20]. Available from: https://www.isric.org/explore/soilgrids*
13. *W. B. Smith, P. D. Miles, C. H. Perry, and S. A. Pugh, 'Forest Resources of the United States, 2007', Washington, 2017. doi: 10.2737/WO-GTR-78.*
14. *D. C. Dey, 'Sustaining oak forests in eastern North America: Regeneration and recruitment, the pillars of sustainability', Forest Science, vol. 60, no. 5. Society of American Foresters, pp. 926–942, Oct. 02, 2014. doi: 10.5849/forsci.13-114.*
15. *USDA, 'Soil taxonomy:a basic system of soil classification for making and interpreting soil surveys', Washington, D.C., 1975. Accessed: Apr. 26, 2023. [Online]. Available: https://handle.nal.usda.gov/10113/CAT87211181*
16. *USDA Forest Service, 'EVALIDator 2.0.6'. Accessed: Sep. 26, 2023. [Online]. Available: https://apps.fs.usda.gov/fiadb-api/evalidator*
17. *M. D. Abrams, G. J. Nowacki, and B. B. Hanberry, 'Oak forests and woodlands as Indigenous landscapes in the Eastern United States', J Torrey Bot Soc, vol. 149, no. 2, May 2022, doi: 10.3159/torrey-d-21-00024.1.*
18. *D. R. Foster et al., 'New England's Forest Landscape: Ecological Legacies and Conservation Patterns Shaped by Agrarian History', in Agrarian Landscapes in Transition: Comparisons of Long-Term Ecological & Cultural Change, C. Redman and D. R. Foster, Eds., Oxford: Oxford University Press, 2008, pp. 44–88. [Online]. Available: https://scholarworks.umass.edu/anthro_faculty_pubs/344*
19. *USFS, 'Forest Products Cut and Sold from the National Forests and Grasslands'. Accessed: Jun. 12, 2023. [Online]. Available: https://www.fs.usda.gov/forestmanagement/products/cut-sold/index.shtml*

20. *M. D. Nelson, G. C. Liknes, and B. J. Butler, 'Map of forest ownership in the conterminous United States. [Scale 1:7,500,000.] Res. Map NRS-2.', Newtown Square, PA, Jul. 2010. Accessed: Mar. 19, 2023. [Online]. Available: http://nrs.fs.fed.us/data/rds/0001*
21. *M. Tyrrell, 'Understanding Connecticut Woodland Owners: A Report on the Attitudes, Values and Challenges of Connecticut's Family Woodland Owners', New Haven, 2015. Accessed: Jun. 13, 2023. [Online]. Available: https://portal.ct.gov/-/media/DEEP/forestry/CTWoodlandOwnersReportpdf.pdf*
22. *DEP, 'New York City Watershed Forest Management Plan', New York City, 2017.*
23. *DCR, 'Massachusetts state forest action plan', 2020. Accessed: Mar. 20, 2023. [Online]. Available: https://www.mass.gov/doc/massachusetts-forest-action-plan/download*
24. *P. Catanzaro and A. D'Amato, 'High Grade Harvesting: Understand the impacts, know your options', 2006. Accessed: Jul. 16, 2023. [Online]. Available: https://masswoods.org/sites/default/files/pdf-doc-ppt/High_Grade_Harvesting_1.pdf*
25. *M. S. Ashton and M. J. Kelty, The Practice of Silviculture: Applied Forest Ecology, 10th ed. New York: Wiley & Sons, 2018.*
26. *P. H. Brose, 'A comparison of the effects of different shelterwood harvest methods on the survival and growth of acorn-origin oak seedlings', Canadian Journal of Forest Research, vol. 41, no. 12, pp. 2359–2374, Dec. 2011, doi: 10.1139/X11-143.*
27. *D. L. Loftis, 'A Shelterwood Method for Regenerating Red Oak in the Southern Appalachians', 1990.*
28. *P. Raymond and S. Bédard, 'The irregular shelterwood system as an alternative to clearcutting to achieve compositional and structural objectives in temperate mixedwood stands', For Ecol Manage, vol. 398, pp. 91–100, Aug. 2017, doi: 10.1016/j.foreco.2017.04.042.*
29. *W. B. Leak, M. Yamasaki, and R. Holleran, 'United States Department of Agriculture Forest Service General Technical Report NRS-132 Northern Research Station Silvicultural Guide for Northern Hardwoods in the Northeast', 2014. [Online]. Available: http://www.nrs.fs.fed.us/*
30. *Elizabeth A. Burrill et al., 'The Forest Inventory and Analysis Database: Database Description and User Guide for Phase 2 (version 9.0.1)', 2021. Accessed: Mar. 21, 2023. [Online]. Available: http://www.fia.fs.fed.us/library/database-documentation/*
31. *MA DCR, 'Manual for Continuous Forest Inventory Field Procedures', 2022.*
32. *D. Cleland, J. Freeouf, J. Keys, G. Nowacki, C. Carpenter, and W. McNab, 'Ecological Subregions: Sections and Subsections for the conterminous United States. Gen. Tech. Report WO-76D.', Washington, DC, 2007. doi: 10.2737/WO-GTR-76D.*
33. *Gary Scoffield, 'US Forest Type Groups', 2012. [Online]. Available: https://databasin.org/datasets/b907b1f86fbd4b18b71541ce19d78496/*
34. *S. L. Arner et al., 'National Algorithms for Determining Stocking Class, Stand Size Class, and Forest Type for Forest Inventory and Analysis Plots', 2001.*
35. *FVS Staff, 'Northeast (NE) Variant Overview of the Forest Vegetation Simulator', Fort Collins, CO, 2008.*
36. *G. E. Dixon, 'Essential FVS: A User's Guide to the Forest Vegetation Simulator', Fort Collins, CO, 2002.*
37. *D. G. Ray, M. R. Saunders, and R. S. Seymour, 'Recent Changes to the Northeast Variant of the Forest Vegetation Simulator and Some Basic Strategies for Improving Model Outputs', Northern Journal of Applied Forestry, vol. 26, no. 1, pp. 31–34, Mar. 2009, doi: 10.1093/njaf/26.1.31.*
38. *M. B. Russell, A. R. Weiskittel, and J. A. Kershaw, 'Benchmarking and calibration of Forest Vegetation Simulator individual tree attribute predictions across the northeastern United States', Northern Journal of Applied Forestry, vol. 30, no. 2, pp. 75–84, Jun. 2013, doi: 10.5849/njaf.12-034.*
39. *A. J. Dugan, J. W. Lichstein, A. Steele, J. M. Metsaranta, S. Bick, and D. Y. Hollinger, 'Opportunities for forest sector emissions reductions: a state-level analysis', Ecological Applications, vol. 31, no. 5, Jul. 2021, doi: 10.1002/eap.2327.*
40. *R. A. Giffen, C. M. Ryan, E. P. Belair, M. A. Pounch, and S. Brown, 'Storing More Carbon by Improving Forest Management in the Acadian Forest of New England, USA', Forests, vol. 13, no. 12, Dec. 2022, doi: 10.3390/f13122031.*
41. *J. S. Nunery and W. S. Keeton, 'Forest carbon storage in the northeastern United States: Net effects of harvesting frequency, post-harvest retention, and wood products', For Ecol Manage, vol. 259, no. 8, pp. 1363–1375, Mar. 2010, doi: 10.1016/j.foreco.2009.12.029.*

42. *N. L. Crookston and G. E. Dixon, 'The forest vegetation simulator: A review of its structure, content, and applications', in Computers and Electronics in Agriculture, Oct. 2005, pp. 60–80. doi: 10.1016/j.compag.2005.02.003.*
43. *USFS, 'National Volume Estimator Library (NVEL)'. Accessed: Jun. 12, 2023. [Online]. Available: https://www.fs.usda.gov/forestmanagement/products/measurement/volume/nvel/index.php*
44. *S. A. Rebain et al., 'The Fire and Fuels Extension to the Forest Vegetation Simulator: Updated Model Documentation', Fort Collins, CO, 2010.*
45. *J. C. Jenkins, D. C. Chojnacky, L. S. Heath, and R. A. Birdsey, 'National-Scale Biomass Estimators for United States Tree Species', Forest Science, vol. 49, pp. 12–35, 2003, Accessed: May 08, 2023. [Online]. Available: https://www.fs.usda.gov/research/treesearch/6996*
46. *J. E. Smith, L. S. Heath, K. E. Skog, and R. A. Birdsey, 'Methods for calculating forest ecosystem and harvested carbon with standard estimates for forest types of the United States', Newtown Square, PA, 2006. doi: 10.2737/NE-GTR-343.*
47. *W. C. Stewart and G. M. Nakamura, 'Documenting the Full Climate Benefits of Harvested Wood Products in Northern California: Linking Harvests to the Us Greenhouse Gas Inventory', For Prod J, vol. 62, no. 5, pp. 340–353, Sep. 2012, doi: 10.13073/0015-7473-62.5.340.*
48. *M. K. Janowiak et al., 'New England and northern New York forest ecosystem vulnerability assessment and synthesis: a report from the New England Climate Change Response Framework project', 2018. doi: 10.2737/NRS-GTR-173.*
49. *USDA, 'Major Forest Insect and Diseases Conditions in the United States 2021', 2023. [Online]. Available: http://www.ascr.usda.gov/complaint_filing_cust.html*
50. *M. C. Boukouvala et al., 'Lymantria dispar (L.) (Lepidoptera: Erebidae): Current Status of Biology, Ecology, and Management in Europe with Notes from North America', Insects, vol. 13, no. 9. MDPI, Sep. 01, 2022. doi: 10.3390/insects13090854.*
51. *C. J. Ewing, C. E. Hausman, J. Pogacnik, J. Slot, and P. Bonello, 'Beech leaf disease: An emerging forest epidemic', For Pathol, vol. 49, no. 2, Apr. 2019, doi: 10.1111/efp.12488.*
52. *D. A. Herms and D. G. McCullough, 'Emerald ash borer invasion of north america: History, biology, ecology, impacts, and management', Annu Rev Entomol, vol. 59, pp. 13–30, Jan. 2014, doi: 10.1146/annurev-ento-011613-162051.*
53. *A. M. Mika and W. S. Keeton, 'Net carbon fluxes at stand and landscape scales from wood bioenergy harvests in the US Northeast', GCB Bioenergy, vol. 7, no. 3, pp. 438–454, May 2015, doi: 10.1111/gcbb.12143.*
54. *D. B. Kittredge and P. M. S. Ashton, 'Natural Regeneration Patterns in Even-Aged Mixed Stands in Southern New England', Northern Journal of Applied Forestry, vol. 7, no. 4, pp. 163–168, Dec. 1990, doi: 10.1093/njaf/7.4.163.*
55. *D. B. Kittredge and P. M. S. Ashton, 'Impact of Deer Browsing on Regeneration in Mixed Stands in Southern New England', Northern Journal of Applied Forestry, vol. 12, no. 3, pp. 115–120, Sep. 1995, doi: 10.1093/njaf/12.3.115.*
56. *M. Martin, D. Woodbury, Y. Glogower, M. Duguid, B. Frey, and M. Ashton, 'Within-gap position shapes fifty years of forest dynamics in a temperate hardwood forest in Connecticut, USA', For Ecol Manage, vol. 494, Aug. 2021, doi: 10.1016/j.foreco.2021.119311.*
57. *R. D. Nyland, 'Exploitation and Greed in Eastern Hardwood Forests', J For, vol. 90, no. 1, pp. 33–37, 1992.*
58. *R. A. Hallett and J. W. Hornbeck, 'Managing Oak and Pine Stands on Outwash Sands: Protecting Plant Nutrients', Northern Journal of Applied Forestry, vol. 17, no. 2, pp. 57–61, Jun. 2000, doi: 10.1093/njaf/17.2.57.*
59. *J. Wikle, M. Duguid, and M. S. Ashton, 'Legacy forest structures in irregular shelterwoods differentially affect regeneration in a temperate hardwood forest', For Ecol Manage, vol. 454, Dec. 2019, doi: 10.1016/j.foreco.2019.117650.*
60. *L. K. Forcier, 'Reproductive Strategies and the Co-occurrence of Climax Tree Species', Science (1979), vol. 189, no. 4205, pp. 808–810, Sep. 1975, doi: 10.1126/science.189.4205.808.*
61. *J. S. He, Q. Bin Zhang, and F. A. Bazzaz, 'Differential drought responses between saplings and adult trees in four co-occurring species of New England', Trees - Structure and Function, vol. 19, no. 4, pp. 442–450, Jun. 2005, doi: 10.1007/s00468-004-0403-2.*
62. *T. F. Au and J. T. Maxwell, 'Drought Sensitivity and Resilience of Oak–Hickory Stands in the Eastern United States', Forests, vol. 13, no. 3, Mar. 2022, doi: 10.3390/f13030389*

APPENDIX–CHAPTER 3

Baseline cropland soil characteristics and management practices are critical to understanding how a shift in management contributes to soil organic carbon (SOC) accrual and CO_2 removal. Baseline conditions for tillage practices are particularly important to capture accurately when identifying cropland soil-based CO_2 removal practices. Cropland management practices as of 2017 are shown in **Figure A3-1,** and the response in crop yield of these different baseline management cases to a cover cropping soil-based CO_2 removal practice is shown in **Figure A3-2.**

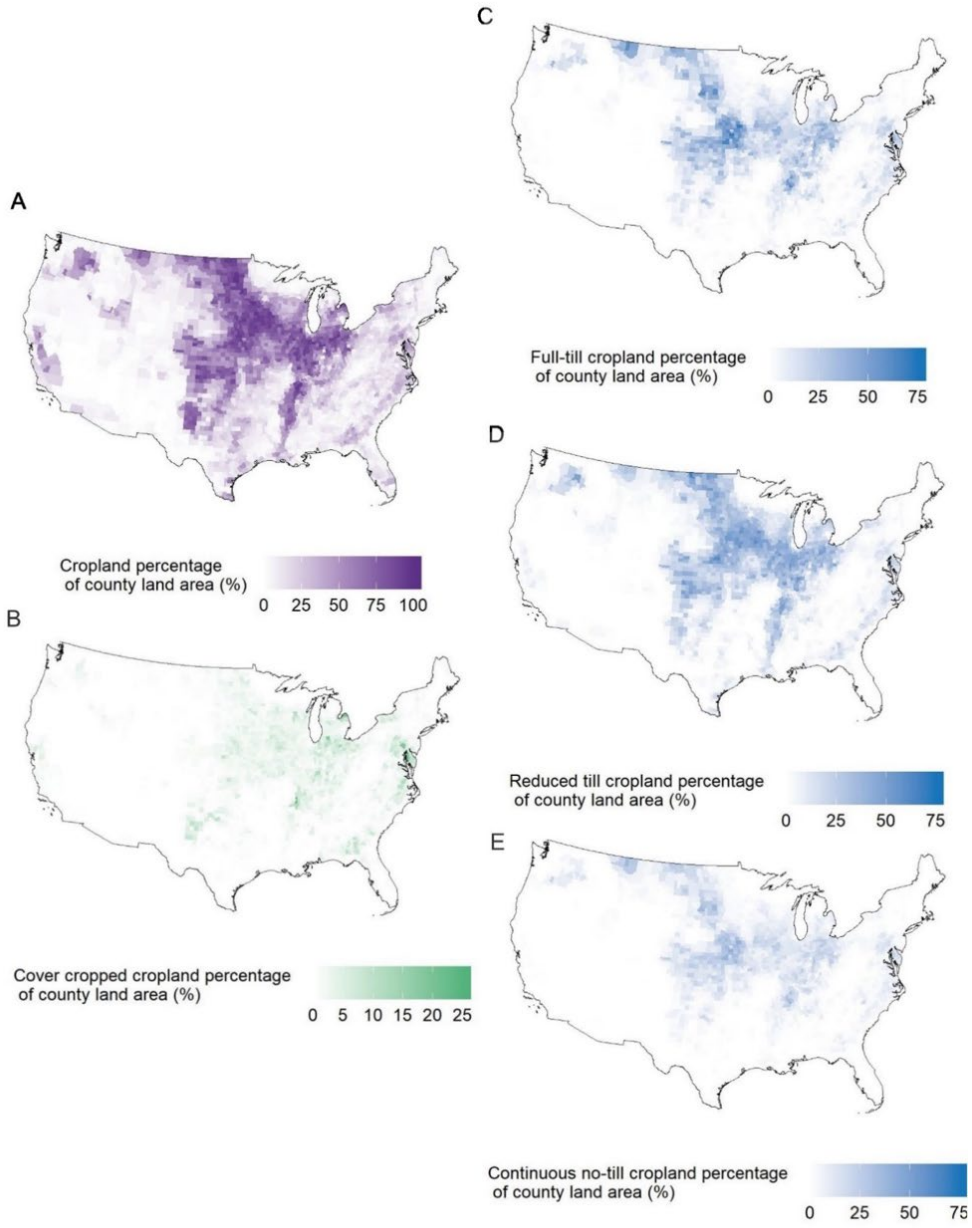

Figure A3-1. Baseline cropland management: Baseline conditions for agricultural management in the United States [1]. Note difference in scales for color bars. Reduced till and continuous no-till land area data is modified from the agricultural land census based on Claassen et al. 2018 [2].

The transition from a full conventional tillage baseline to continuous no-till practice, as represented by the DayCent biogeochemical model, is given in **Figure A3-3.** Whether or not these practices will be implemented depends on the balance of income received relative to the cost of implementation (**Table A3-1**) and the opportunity cost of not continuing the previous practice (e.g., the U.S. dollar value per tonne of change in Figure A3-2).

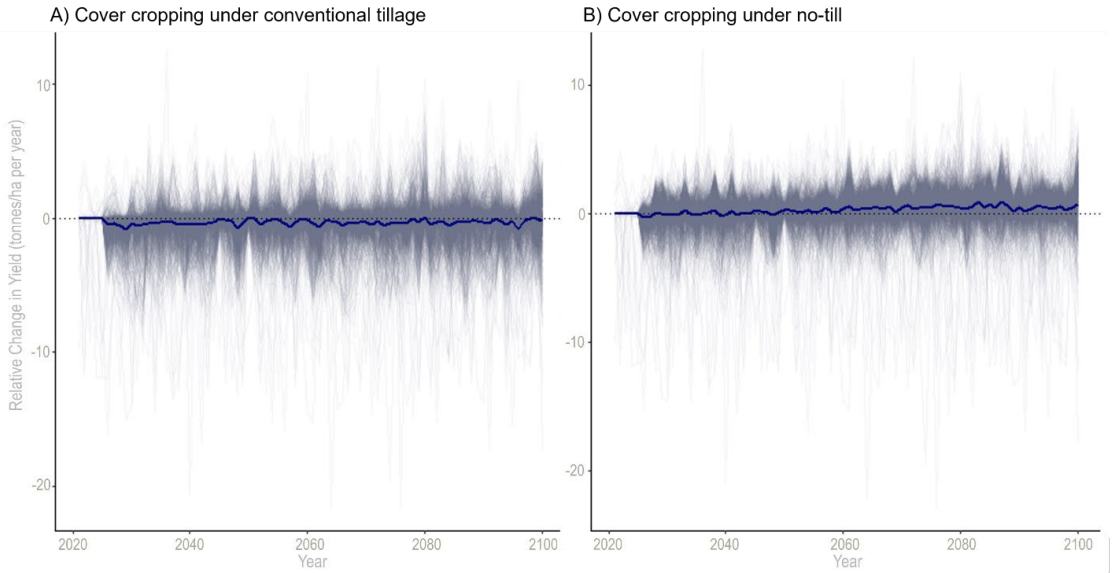

Figure A3-2. Cover crop grain yield: The response of annual grain yield (tonnes/ha) from commodity crops to the implementation of cover crops for every cropland-containing county in the United States. Each line is the response for each cropland-containing county in the United States.The dark, bold line represents the national mean annual grain yield response across all counties. Cover cropping slightly decreased mean annual yield under conventional tillage (A) and had no impact on yield under no-till (B) through 2050.

Table A3-1. Table implementation costs.

Management practice	Mean implementation cost*	Payment schedule ID
	$ per hectare	(USDA EQIP)
Cover Crop	234.94	340 + E340B
Field Border - native species	461.91	386
Perennial Carbon Crop	**	**
Reduced till	79.26	345+ E345D
No-till	57.18	329

** USDA EQIP 2022*

*** see biomass methods for economic cost assumptions*

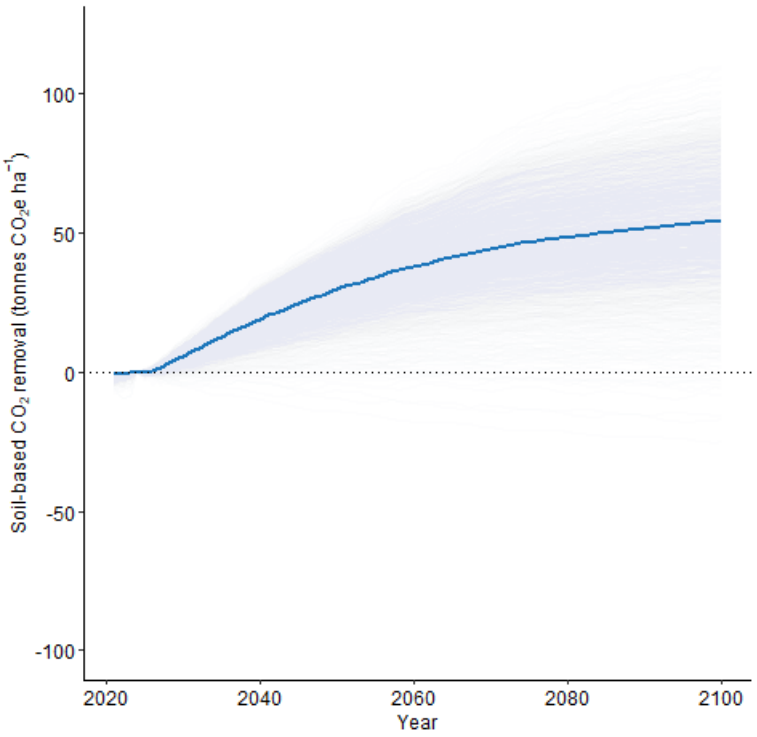

Figure A3-3: Biogeochemical trajectories of soil-based CO_2 removal in continous no-till management since 2025 over time relative to a full-till commodity crop baseline. CO_2 removal accounts for changes in soil carbon baseline as well as a penalty for any increased nitrous oxide. Continuous no-till management was simulated across county-representative commodity cropland using the DayCent biogeochemical model [3, 4] with future climate inputs from the MIROC-ES2L earth system model. Trajectories for each county containing cropland in the United States are represented with individual lines. The overall mean trajectory across all counties is represented with a bold blue line.

Methods

Modelling Biogeochemical Response to Cropland Management

We used the latest version of the DayCent ecosystem biogeochemical model [35] that is implemented in the current US national greenhouse gas (GHG) inventory and is being incorporated into the COMET-Farm system. The new model version includes a number of improvements that impact modeling soil C and N gas fluxes and now simulates SOC dynamics to 30-cm soil depth (earlier versions were parameterized for 20 cm).

Sample Design

The modeling sample of point locations on agricultural land was created using a random sampling approach. The approach sampled approximately 300 points per Major Land Resource Area, subregions identified as sharing similar parent material, water resources, climate, soil type, and crop type [5], [6]. A total of 37,283 sites were sampled from across 2057 cropland containing counties, averaging 18 sites per county, and ranging from 1 to 219 sample sites per county. Samples were restricted to croplands that could be modeled in DayCent, using a mask generated from United States Department of Agriculture's (USDA's) Cropland Data Layer (CDL) datasets (https://croplandcros.scinet.usda.gov/). Since our effort

focused on annual croplands only, the sample was further refined to exclude any points with orchards or vineyards and had to have at least one annual crop in the time series. Modelling efforts were limited to annual croplands due to the requirement of rotation in order to plant cover crops and their large percentage of cropland extent; however, there is also potential for soil-based CO_2 removal in perennial croplands that were not included in this study.

Baseline Management

For all conventional agriculture points, crop rotation was determined from actual crops observed in CDL for 2009–2018, and repeated to fill out the time series, whether for the current period (2008–2020) or future scenarios (2021–2100). Baseline agricultural management such as plant/harvest dates and fertilizer rates were pulled from the same database developed for modeling the Healthy Soils version of COMET-Planner (http://comet-planner-cdfahsp.com/). Typical planting and harvest dates for common grain/row crops were derived from USDA (USDA-NASS, 2010). For tillage, all points were run as conventional, reduced, and continuous no tillage (Table A3-2).

Table A3-2. Management scenarios.

Starting year	Baseline management	Simulated practice changes
2025, 2045	Conventional till	Cover crop
	Reduced till, No till	Commodity crops to perennial grasses (e.g., CRP or perennial field border)
		Reduced till No till

Future/Conservation Management

Business as usual (baseline) and scenarios of changes for conservation management in the future were listed in Table A3-2. The adoption of practice changes to baseline scenarios was from 2025 or 2045, and the practice changes reported here include only the 2025 scenario from the MIROC_ES2L earth system model climate projections. For scenarios of adding a cover crop, non-legume cereal rye [6] was planted after any annual crop when there was a fallow period >90 days after August. Transition to perennial grass was simulated as a native grass.

DayCent Model Runs and Analyses

All of the above cropping and management data were converted to DayCent schedule files. Site-specific soil characteristics required for DayCent was derived from SSURGO [7], including soil texture, soil water holding capacity, and initial SOC contents. Daily weather for current and future climate under climate change scenarios were downloaded from the NASA Earth Exchange Global Daily Downscaled Projections (NEX-GDDP-CMIP6) [8]. Historic management (pre-cultivation through 2007) schedules were the same as those used in COMET-Farm, which were determined through internal USDA staff surveys during development of COMET-Farm. It was assumed that current croplands had been under long-term cropping, as spatially explicit land use histories were very limited. As such, all sites were simulated for conventional, reduced, and continuous no tillage, respectively, in the current period. For irrigated sites, automatic irrigations occur during the growing season if the available water stored in the plant root zone falls below 55% of the available water holding capacity. Parameter values used in the USDA COMET-Farm platform were used in this project. Simulations ran by management scenarios, and earth system models

under one moderate GHG emission scenario (Shared Socioeconomic Pathways or SSP 2 - 4.5 [Table A3-3]).

Table A3-3. Climate and emission projections.

Shared Socioeconomic Pathway	Earth System Model
2-4.5	MIROC_ES2L FGOALS_g3 MRI_ESM2_0 NorESM2_LM MPI_ESM1_2_LR GFDL_ESM4

Biogeochemical Responses to Perennial Carbon Crops for Biomass

The System Approach for Land Use Sustainability model (SALUS) was used to simulate low-productivity stable cropland [9] in the Midwest region. Required soil inputs were derived from SSURGO and daily historical weather was provided by gridMET [10]. For these locations, conventional farming was assumed as previous land history and as typical management before converting to a perennial carbon crop. Conventional farming management is assumed as corn–soybean rotation with historical planting dates derived from NASS planting progress reports [1], and nitrogen fertilizer was applied to the corn crop. Conventional tillage was implemented as chisel plow to 20 cm depth in the fall and field cultivator to 10 cm depth in the spring. After 10 years of conventional farming, the land is converted to the perennial carbon crop, switchgrass. Switchgrass simulations included an annual addition of 50 kg of nitrogen per hectare, which is agnostic to the source of nitrogen and could be from legume planting or synthetic nitrogen amendment. Soil organic carbon and nitrous oxide emissions were both simulated annually for each sub-county, and aggregated to the county scale. SALUS has been validated to simulate switchgrass in the Midwest [11]. Further details on assumptions for biogeochemical process modeling through the SALUS model can be found in Chapter 6.

Perennial Carbon Crop Economic Decision Model: AgModel

The county-level agricultural outlook model covers the contiguous United States and includes six cash crops, i.e., barley, corn, rice, sorghum, soybeans, and wheat. Previous versions of the model have been published in Dumortier (2016) [12] and Dumortier et al. (2017) [13]. Besides cash crops, the possibility to harvest two types of agricultural residues (i.e., corn stover and wheat straw) and switchgrass are included as well. The model consists of supply and demand modules that take commodity, biomass, and CO_2e climate benefit (expressed in $USD per metric tonne of CO_2e) prices as inputs. The latter two are only used in the supply module of the model. That is, based on the biomass and carbon prices, farmers harvest agricultural residues and switchgrass. Climate benefit and soil-based CO_2 removal for each county were calculated using historical, county-specific SALUS biogeochemical model outputs for the transition of low-productivity stable corn and soy cropland rotation to perennial switchgrass carbon crop between 1979 and 2021, projected into the future. Planting perennial carbon crops, i.e., switchgrass, instead of annual cash crops increases soil-based CO_2 removal, allowing farmers to receive CO_2 removal incentives in addition to income from selling carbon crop biomass.

The supply module uses historic county-level data from the National Agricultural Statistics Service (NASS) of the USDA to project crop yields linearly into the future. The same data source is also used to calibrate crop area by county given commodity prices. Cash crops cost of production are obtained from the USDA Cost and Return Database by Farm Resource Region and are linked to energy prices and producer price indices from the 2022 Annual Energy Outlook (AEO) published by the United States Energy Information Administration (EIA). The AEO projects energy prices and producer price indices until 2050, which corresponds to the time horizon used in this analysis. Land allocation among the various cash crops is based on per hectare net returns (i.e., crop price times yield minus operating cost) of all crops. Area allocated to a particular crop not only depends on the returns of the crop in question but also on the returns of the other crops. For corn and wheat, the revenue from harvesting and selling crop residues are included as well.

On the demand side, crops are consumed by the non-feed, feed, and export sectors. The demand functions are modelled as constant elasticity functions. For corn, we also have exogenous biofuel demand from the vehicle sector in the United States. The calculation of the biofuel demand from the transportation sector is described in Chapter 6.

Synthesis of Biogeochemical and Economic Constraints for Cover Crop, Perennial Field Borders, and No-till Management

Climate Benefit and Soil-based CO_2 Removal Rates

DayCent biogeochemical model outputs between 2025 and 2050 were used to calculate annual and cumulative relative changes in SOC, nitrous oxide fluxes, and commodity crop yield between new management practices and their counterfactual management in each county.

For the practices of cover cropping and perennial field borders, tillage was assumed to remain consistent according to the baseline tillage regime, which was either conventional full-till, reduced till, or no-till. Baseline tillage regime was allocated within each county-based percentage of total applicable land (the sum of full-till, reduced-till area, and no-till area) from the 2017 USDA NASS agricultural census, but modified to estimate continuous no-till. Four-year continuous till minimum is approximately 21% of all land area [2], so to adjust agricultural census annual no-till areas to continuous no-till, we multiplied the classified no-till by 59%, and added the remaining 41% of classified no-till to the reduced till land area in each county, such that total land area under at least four years of continuous no-till was 21% of cropland in the United States. DayCent simulated cover cropping and perennial field borders within each of the tillage scenarios in each county, accounting for county- and tillage-specific biogeochemical responses. Transitions to reduced till were assumed to be only amenable from a full-till baseline counterfactual, and transition to no-till was assumed to be amenable only to full- and reduced-till baseline counterfactuals. We also explored the climate-change impacts of imposing a new management in 2045 instead of 2025, but report only transition in 2025 in this report. Where baseline counterfactuals were missing from DayCent simulations, we could not analyze changes in converted practices, and thus omitted counties (FIPS codes 37003 and 22053) from the analysis.

Biogeochemical responses to new management were calculated relative to initial value and baseline counterfactual trajectories. We tracked both annual and cumulative differences in SOC stocks, nitrous oxide emissions, grain yield, and associated grain yield income for each county. Annual rate of total climate benefit was calculated using SOC and nitrous oxide emissions relative to the counterfactual baseline in 2050 and linearized over the 25 years between 2025 and 2050 such that the cumulative relative difference reflects the accurate non-linear accumulation of soil carbon and climate benefit.

$$Annualized\ total\ climate\ benefit\ (tonne\ CO_2e\ ha^{-1}\ y^{-1})$$
$$= \left(Soil\ organic\ C_{practice,2050} - Soil\ organic\ C_{baseline,2050}\right)$$
$$- \frac{(Cumulative\ N_2O_{practice,2050} - Cumulative\ N_2O_{baseline,2050})}{(2050 - 2025\ y)}$$

SOC accumulation was converted to CO_2 by mass (44 g CO_2 per 12 g C), and nitrous oxide emissions were converted to CO_2e through mass and 100 year global warming potential of 273 CO_2e per mol of N_2O [14]. Total climate benefit includes avoided losses of SOC and avoided nitrous oxide emissions, which do not count toward CO_2 removal but are important components of agricultural climate change mitigation. Incentivizing climate benefit avoids any potential perverse incentive to remove atmospheric CO_2 at the cost of emitting additional nitrous oxide. We calculate mean annual soil-based CO_2 removal through triangulation from the time of practice implementation and baseline trajectories for soil carbon and nitrous oxide emissions.

$$Annualized\ soil\ carbon\ dioxide\ removal\ (tonne\ CO_2\ ha^{-1}\ y^{-1})$$
$$= \left(Soil\ organic\ C_{practice,2050} - Soil\ organic\ C_{practice,2025}\right.$$
$$- positive\ values\ only\ of: (Soil\ organic\ C_{baseline,2050}$$
$$\left. - Soil\ organic\ C_{baseline,2025})\right) - Positive\ values\ only\ of: (Cumulative\ N_2O_{practice,2050}$$
$$- Cumulative\ N_2O_{baseline,2050}) / (2050 - 2025\ y)$$

Constraining Land Area for Management Implementation with Economics

Land area economically amenable to implementing each new practice was determined as cropland where income to the farmer is greater than the cost to the farmer for each tillage regime for each county. Because the DayCent biogeochemical model used a 10-year rotation of representative crops from the CDL that implement cover cropping during different years throughout that rotation, we chose a time horizon of 10 years over which to compare the difference in cumulative income to determine whether a practice will be implemented or not.

$$Cost\ (\$USD\ per\ ha) = Foregone\ income + Implementation\ cost * Area\ modifier$$

Area modifier accounts for the fraction of cropland area over which the practice could be implemented and is equal to one for cover cropping and no-till but is modified to 0.01 for perennial field borders, where only 1% of cropland would be modified to create a field border, due to the primary goal of keeping 99% of the land planted in cash crops. The per-area cost of implementing each practice was determined by existing state-specific public payment schedules for the USDA Environmental Quality Incentive Program. National average implementation costs are found in Table A3-4.

We used DayCent yield projections combined with the most recent land area data under each crop [1] to calculate farmer crop income in $USD (valued in year 2022) for each of the following commodity crops: corn, wheat, cotton, soybean, oats, barley, sorghum grain, hay, and peanuts. Grain yield data from DayCent was reported in units of g C per m^{-2} and converted to metric tonne of dry grain biomass per hectare using the assumption that grain is ~40% carbon [15] averaged across commodity crops. We acknowledge that this is a coarse assumption, where carbon percentage of grain is crop-dependent and ranges between 33 and 45% carbon [16]. Crop prices were consistent with the prices used for the sophisticated POLYSYS and AgModel economic models used for the carbon crop biomass in this chapter and in Chapter 6, and are detailed in Table A3-4. We tracked cumulative income from commodity crop yield in both baseline counterfactual and for new management in each county and tillage case and calculated foregone income as the total yield-based income in the counterfactual baseline minus yield-based income under the new practice. In any case for which the new practice increases yield relative to counterfactual, the negative cost counts offsets rather than adds to costs of implementation.

$$Foregone\ Income\ (\$USD\ per\ ha) = \frac{(Cumulative\ yield\ income_{baseline,2025-2035} - Cumulative\ yield\ income_{practice,2025-2035})}{Area\ of\ cropland\ under\ baseline\ tillage\ regime * 10\ years}$$

To determine potential income to the farmer in each county, we calculated county-specific USD per hectare incentives using the payment-per-tonne method:

$$Incentive\ (\$USD\ ha^{-1}\ y^{-1}) = CO_2\ price\ (\$\ per\ tonne\ CO_2e) * Total\ climate\ benefit\ (tonne\ CO_2e\ ha^{-1}\ y^{-1})$$

Table A3-4. Crop price inputs for economic land-use decisions for farmers in a county, multiplied by loss (or gain) in yield to determine foregone income (or increased income) due to a practice. Prices are given per dry metric tonne of grain earned by farmers in terms of 2022 USD.

Crop	POLYSYS crop price
	$USD per dry tonne
Corn	184.64
Grain sorghum	134.64
Oats	124.8
Barley	118.5
Wheat	235.16
Soybeans	385.44
Cotton	1748.26
Hay	187.89
Peanut	386.46

Supply Curves: Sensitivity of National CO_2 Removal and Climate Benefit to Carbon Prices

We analyzed the sensitivity of regional and national soil-based CO_2 removal to a range of incentive rates, which closely paralleled the sensitivity of land area to convert to a new practice given each incentive rate. Separately, we summed CO_2 removal and climate benefit across all tillage regime baselines for each county, weighted by the land area in each tillage regime where cropland converts to the new practice. That is, for each county:

$$CO_2\ removal_{full\ till}\ (tonne\ CO_2\ ha^{-1}\ y^{-1}) * Land\ area\ converted\ to\ practice_{full\ till}\ (ha) +$$
$$CO_2\ removal_{reduced\ till}\ (tonne\ CO_2\ ha^{-1}\ y^{-1}) * Land\ area\ converted\ to\ practice_{reduced\ till}\ (ha) +$$
$$CO_2\ removal_{no\ till}\ (tonne\ CO_2\ ha^{-1}\ y^{-1}) * Land\ area\ converted\ to\ practice_{no\ till}\ (ha)$$
$$= Annual\ CO_2\ removal\ per\ county\ (tonnes\ y^{-1})$$

While field borders and cover crops could be planted in the same fields, neither cover crops nor field borders would co-occur with perennial carbon crops. To deconflict land such that no land could be double-counted for multiple practices, we subtracted the area of land converted to perennial carbon crops in each county from the land area converted to any of the other practices. Perennial carbon crops

were prioritized in this report because the biomass produced for carbon removal and sequestration was used as inputs to Chapter 6 section 1 (Biomass and BiCRS conversion technologies) of this report. With land area deconflicted, we are able to sum the combined value for area for each practice in each county to get county-wide CO_2 removal in each year for combined use of cover crops, perennial field borders, and perennial carbon crops. National potential at each CO_2 price point was calculated by taking the sum of each response variable across all counties in the year 2050.

We calculated "Cost" of CO_2 removal for Figure 3-14 (see main document) by summing the total dollars given as incentives for additional removal ($40 per tonne CO_2e incentive * (total climate benefit for practice with $40 incentive—total climate benefit for practice with $0 incentive in tonnes CO_2e) and dividing by true atmospheric CO_2 removal (tonnes CO_2) instead of total climate benefit. Because climate benefits of the practices examined also include avoiding GHG emissions, the climate benefit is greater than the true CO_2 removal, resulting in a higher per tonne cost of CO_2 removal relative to the prescribed price of the CO_2e incentive.

REFERENCES

1. *U. S. Department of Agriculture. Census of Agriculture. 2017 Published by National Agricultral Statistics Service; Available from www.nass.usda.gov/AgCensus.*
2. *Roger Claassen, et al. Tillage Intensity and Conservation Cropping in the United States. 2018. EIB 197; http://dx.doi.org/10.22004/ag.econ.277566.*
3. *Tingting Liu, Randall J. F. Bruins, and Matthew T. Heberling, Factors Influencing Farmers' Adoption of Best Management Practices: A Review and Synthesis. Sustainability, 2018. **10**(2): p. 432, https://doi.org/10.3390/su10020432.*
4. *Ram B. Gurung, et al., Bayesian calibration of the DayCent ecosystem model to simulate soil organic carbon dynamics and reduce model uncertainty. Geoderma, 2020. **376**: p. 114529, https://doi.org/10.1016/j.geoderma.2020.114529.*
5. *United States Department of Agriculture, Natural Resources Conservation Service, "Land resource regions and major land resource areas of the United States, the Caribbean, and the Pacific Basin," U.S. Department of Agriculture. Available: https://www.nrcs.usda.gov/sites/default/files/2022-10/AgHandbook296_text_low-res.pdf.*
6. *Conservation Technology Information Center, "National Cover Crop Survey Report 2022-2023," Conservation Technology Information Center, Sustainable Agriculture Research and Education, American Seed Trade Association, 2023. Available: https://www.sare.org/wp-content/uploads/2022-2023-National-Cover-Crop-Survey-Report.pdf.*
7. *Soil Survey Staff. Gridded Soil Survey Geographic (gSSURGO) Database for the Conterminous United States. United States Department of Agriculture, Natural Resources Conservation Service. . 2020 Published by Available from https://gdg.sc.egov.usda.gov/.*
8. *Bridget Thrasher, et al., NASA Global Daily Downscaled Projections, CMIP6. Scientific Data, 2022. **9**(1): p. 262, https://doi.org/10.1038/s41597-022-01393-4.*
9. *Bruno Basso, et al., Yield stability analysis reveals sources of large-scale nitrogen loss from the US Midwest. Scientific Reports, 2019. **9**(1): p. 5774, https://doi.org/10.1038/s41598-019-42271-1.*
10. *John T. Abatzoglou, Development of gridded surface meteorological data for ecological applications and modelling. International Journal of Climatology, 2013. **33**(1): p. 121-131, https://doi.org/10.1002/joc.3413.*

11. *Rafael Martinez-Feria and Bruno Basso, Predicting soil carbon changes in switchgrass grown on marginal lands under climate change and adaptation strategies. GCB Bioenergy, 2020.* ***12****(9): p. 742-755, https://doi.org/10.1111/gcbb.12726.*

12. *Jerome Dumortier, Impact of agronomic uncertainty in biomass production and endogenous commodity prices on cellulosic biofuel feedstock composition. GCB Bioenergy, 2016.* ***8****(1): p. 35-50, https://doi.org/10.1111/gcbb.12238.*

13. *Jerome Dumortier, Nathan Kauffman, and Dermot J. Hayes, Production and spatial distribution of switchgrass and miscanthus in the United States under uncertainty and sunk cost. Energy Economics, 2017.* ***67****: p. 300-314, https://doi.org/10.1016/j.eneco.2017.08.023.*

14. *Chris Smith et al., "2021: The Earth's Energy Budget, Climate Feedbacks, and Climate Sensitivity Supplementary Material," in 2021: The Earth's Energy Budget, Climate Feedbacks and Climate Sensitivity Supplementary Material, Masson-Delmotte, V., P. Zhai, A. Pirani, S.L. Connors, C. Péan, S. Berger, N. Caud, Y. Chen, L. Goldfarb, M.I. Gomis, M. Huang, K. Leitzell, E. Lonnoy, J.B.R. Matthews, T.K. Maycock, T. Waterfield, O. Yelekçi, R. Yu, and and B. Zhou, Eds. [Online]. Available: https://www.ipcc.ch/*

15. *Jonathan L Grennell, Yield and carbon exchange of sorghum grown as advanced biofuel feedstock on abandoned agricultural land in southeastern Ohio. 2014, Ohio University (http://rave.ohiolink.edu/etdc/view?acc_num=ohiou1399458748).*

16. *Holou Roland Ahouélété Yaovi and Kindomihou Valentin Missiakô, The Biofuel Crops in Global Warming Challenge: Carbon Capture by Corn, Sweet Sorghum and Switchgrass Biomass Grown for Biofuel Production in the USA, in Frontiers in Bioenergy and Biofuels, J.-L. Eduardo and Z. Leila Queiroz, Editors. 2017, IntechOpen: Rijeka. p. Ch. 7 (https://doi.org/10.5772/65690).*

APPENDIX – CHAPTER 4

Storage of supercritical phase fluid CO_2 may need to be deployed in areas where capture and geologic storage from existing point sources has not been previously considered and, as such, the suitability of the subsurface for storage is not well understood. We are re-evaluating storage feasibility and costs in conventional deep saline formations using a series of recently updated national databases (**Table A4-1**). This appendix comprises three sections: previous studies of storage cost; storage project mapping methods; and mean storage cost estimation methods.

Previous Studies of Storage Cost

Table A4-1. Map inputs to project-based storage cost

Citation	Storage type	Low cost per tonne $C0_2$	High cost per tonne $C0_2$
Allinson et al. (2003) [1]	20 sites onshore Australia	$0.2	$5.1/
Bock et al. (2003) [2]	Onshore storage US depleted gas fields	$0.5	$12.2
Bock et al. (2003) [2]	Onshore US oil fields	$0.5	$4.0
Budinis et al. (2018) [3]	Onshore saline formations	$3.1	$18.8
Dahowski et al. (2005) [4]	Available CO_2 storage capacity	$12	$15
Eccles et al. (2012) [5]	75% storage capacity for 15 US saline formations	Less than $2	n.a.
Middleton et al. [6]	n.a.	$7	n.a.
Grant [7, 8]	n.a.	n.a.	n.a.

Mapping the Sedimentary CO_2 Storage Window

Large-volume, deep saline formation storage requires that the following criteria be met in order to be permittable and feasible:

- Layered sedimentary rocks (both injection and confining zones)
- A depth of at least 750 m below the top of the saturated zone so that the CO_2 will be stored as efficient, dense phases (supercritical or, in a few cases, liquid)
- A depth below regulatorily protected (defined as >10,000 ppm total dissolved solids or "TDS") underground sources of drinking water (USDW)
- Depth in the normally pressured section above the top of overpressure
- Above low permeability rocks at depth (defined as crystalline basement, low- to high-grade metamorphic rocks, or deeply buried (>4 km) sediments in which porosity has been lost by compaction)

In our analysis, we screened out those parts of the subsurface where these five criteria are not met and produced a map (**Chapter 4, Figure 4-3**) that shows the distribution of rock volumes that are prospective

for further evaluation. We then combined, rectified, and documented previously compiled data from the DOE-National Energy Technology Laboratory (NETL)-funded University of Texas Bureau of Economic Geology brine database [9], the US Geological Survey CO_2 storage assessment units inventory [10], and the National Carbon Sequestration (NATCARB) database [11] to add detail to our feasibility database. We used these data to annotate where storage potential is high (prospective deep saline formations are both thick and permeable) and moderate (prospective deep saline formations are thinner or less permeable).

The top and bottom CO_2 storage window boundaries delineate physical boundaries in sedimentary formations within which CO_2 can be stored conventionally (Figure A4-1). The sedimentary CO_2 storage window (SSW) is calculated by taking the difference between the depth to the bottom storage window boundary and the depth to the top storage window boundary (eq. 2.1).

$$SSW = depth\ to\ bottom\ boundary - depth\ to\ top\ boundary \quad (2.1)$$

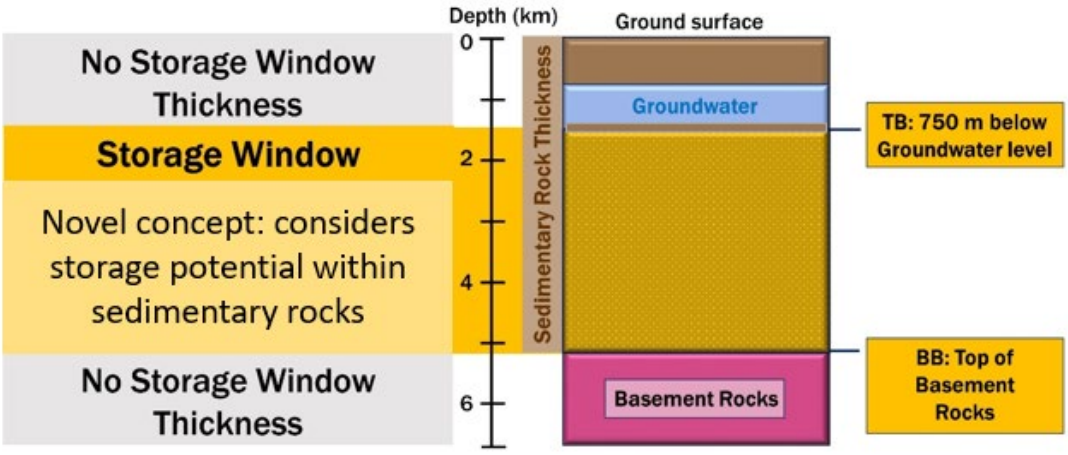

Figure A4-1. Sedimentary CO_2 storage window (SSW) schematic. TB = top SSW boundary, BB = bottom SSW boundary.

The shallowest depth at which CO_2 remains is as a warm dense fluid (supercritical) and is estimated with a simplification to be 750 meters below the top of groundwater. The bottom window delineates the base of the sedimentary rock below which Precambrian-aged basement rocks begin. The Gulf of Mexico Basin formations are an exception in that the bottom window represents depth to top of overpressure rather than base of the sedimentary rock section.

Sedimentary CO_2 Storage Window Input Data

Calculation of the storage window is the result of the compilation, editing, and grid algebra applied to pre-existing spatial data. To process and edit the data, ArcGIS software and tools (i.e., Raster Calculator) were utilized for spatial data calculations. Table A4-2 summarizes the input data and data sources utilized to calculate both the top and bottom SSW boundaries.

Table A4-2. Storage window analysis input data summary table.

Storage window analysis	Input data	Data sources
Top SSW boundary	Depth to groundwater table	De Graaf et al. 2017 [12]
	Continental digital elevation models	Porter et al. 2018 [13]
		USGS 2022 [14]
		Laske and Masters 1997 [15]
Bottom SSW boundary	US wide sedimentary rock thickness	Marshak et al. 2017 [16]
	Depth to overpressure (Gulf of Mexico)	Shah et al. 2018 [17] Burke et al. 2012 [18]

US-Wide Sedimentary Rock Thickness

Three sources delineating different regions in the United States: western US [17], central US [16], and eastern US [15] were utilized and modified to create a cohesive, national-scale sedimentary rock thickness dataset. To merge all three sources, contour lines were created from each data source, and later rasterized utilizing ArcGIS's topo to raster interpolation tool. The western US sediment thickness map covers the western states and continues east until reaching the Precambrian basement craton edge [17]. Unlike the central and eastern US sources, where sedimentary thickness extends to the Precambrian basement, the western US thickness map includes sediment thickness up to the top of the Mesozoic basement. Additionally, the contour lines in the eastern US data source were edited such that they do not overlap with data from the middle US data source to avoid overlapping sources of data when compiling all three data sources together.

Depth to Groundwater

The groundwater depth data utilized for this project is a two-layer global groundwater model utilizing a combination of the hydrological model PCR-GLOBWV and a groundwater model using MODFLOW [12]. The model is presented in monthly time-steps with December 2015 as the last iteration of the model. Thus, December 2015 was chosen to represent the depth to top of groundwater. The global groundwater model is split into two layers, Layer 1 and Layer 2. Layer 2 is described as the top of the confining geological layer, while Layer 1 is the top of the confined aquifer underneath it. De Graaf et al. (2017) [12] delineated the layers based on grain sizes of unconsolidated sediments (GLiM). Since De Graaf et al. defines Layer 1 to include top of "partially" confined aquifers as well (meaning there is still transmissivity through Layer 1 to Layer 2), this study utilizes Layer 2 to represent depth to top of groundwater.

Continental Digital Elevation Models

Continental digital elevation models (DEMs) from the lower 48 states [14] and Alaska [13] were utilized to edit spatial datasets. For example, the central US original database [16] provided depth to top of Precambrian basement relative to mean sea level; therefore, 3DEP DEM data were needed to create an accurate sediment thickness map of this data source. DEM data were also utilized to exclude areas of steep elevation change, as mentioned in Chapter 4.

Depth to Overpressure

Burke et al., 2012 [18] comprises a geopressure-gradient model consisting of 200,000 mud-weight measurements from 70,000 wells and depth-created contour maps of these geopressure-gradient surfaces ranging from 0.6 psi/ft to 1.0 psi/ft. This study utilizes the geopressure-gradient surface of 0.7 psi/ft to delineate depth to top of overpressure in the Gulf of Mexico Basin, as this surface is considered to represent the top of the overpressure transition zone.

No Storage Window Criteria

This section discusses the three different 'no storage window' criteria considered for the SSW data. All three compose the no storage window spatial data that complements the SSW data.

Basement rocks, metamorphic and igneous rocks

We screened out areas where metamorphic or igneous rocks are present at the surface. As a broad category, igneous and metamorphic rocks commonly lack the geologic characteristics necessary for subsurface fluid storage, such as alternating layers of high porosity and permeability rocks with low porosity and permeability rocks. We added basalts and other igneous rocks that may be prospective for storage back in as an alternate resource where mineral trapping may be effective.

Insufficient Sedimentary Thickness

In some areas of the United States, there is a lack of sufficient sedimentary thickness to successfully store CO_2 in the subsurface. CO_2 needs to be stored deeper than 750 meters below the top of groundwater to maintain its dense fluid state. In locations where the sedimentary rock column is shallower than 750 meters, no conventional supercritical storage potential is available.

Topographic Constraints

We excluded areas of steep slopes and areas where the elevation is greater than 1000 meters, because these conditions will make storage infrastructure construction and logistics more complicated and increase costs.

Pressure-based CO_2 Storage Capacity Methodology

As CO_2 is injected into the subsurface, the resulting pressure increase extends outward from the injection well, typically surpassing the plume itself (**Figure A4-2**). The pressure space needed to support a project directly impacts total storage costs.

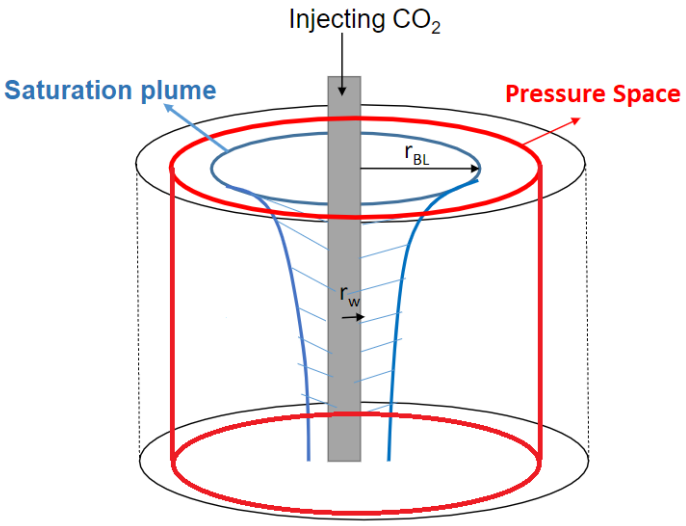

Figure A4-2. Diagram of the 'pressure space' concept. CO_2 plume and pressure build-up (pressure space) propagation in the subsurface (modified from S. Bakhshian, unpublished figure).

Pressure space considers the induced pressure increase and propagation from injected CO_2 within a porous volume in a given geologic formation (eq. 3.1):

$$\text{Pressure Space} = \text{(Allowable Pressure Increase)} * \text{(Pore Volume)} \tag{3.1}$$

Pressure-based CO_2 storage capacity takes the concepts of pressure space as given in equation 3.1, and can be rewritten with the following parameters:

$$Cap_P = \frac{(P_I * C_T * \rho_{CO2}) * (\Phi * A * SWFT * N{:}G)}{1000} \tag{3.2}$$

Where the parameters are:

Cap_P is pressure-based capacity (in million tons (Mt) of CO_2)

P_I is pressure increase (MPa)

C_T is total compressibility (1/MPa)

ρ_{CO2} is CO_2 density (kg/m^3)

Φ is porosity (decimal)

A is area (m^2)

SWFT is storage window formation thickness (m)

$N{:}G$ is net to gross injectable interval (decimal)

Pressure-based CO_2 Storage Capacity Parameters

The parameters considered to calculate pressure-based CO_2 storage capacity (**Table A4-3**) are a combination of (1) input data from sources such as the Gulf Coast Carbon Center's (GCCC) CO_2 Brine database [9] and US Geological Survey's Carbon Dioxide Storage Assessment, [10] 2) calculated parameters from input data (i.e., midpoint formation depth, MDF), and (3) calculated parameters derived from other calculated parameters (i.e., CO_2 density).

Table A4-3. Inputs for pressure space calculations used in this report.

Input	Description	Units
Pressure increase	Amount of pressure increase that can occur as a result of CO_2 injection without fracturing the storage reservoir (see **Figure 4-4**)	MPa
Total compressibility	Volume change of the reservoir rock and fluid in response to pressure changes caused by injection of CO_2	MPa^{-1}
CO_2 density	Ratio of mass to volume of injected CO_2 at reservoir temperature and pressure	kg/m^3
Porosity	Fraction of fluid-filled space in a given volume of rock	unitless
Area	Constant 25 km^2	km^2
Storage window formation thickness (SWFT)	Total thickness of reservoir rocks within the storage window	m
Net-to-gross injectable interval	Fraction of reservoir rocks with adequate permeability for storage	unitless
Midpoint formation depth (MPD)	The depth to the midpoint of the SWFT	m
Reservoir temperature	Temperature at the MPD	°F
Salinity	Dissolved salt content of formation brine	kg/m^3

Storage Window Formation Thickness

The SWFT, meters is the total thickness of all reservoir formations within the sedimentary CO_2 SSW. The goal is to omit any part of the geologic section that would not be feasible to store CO_2 long-term.

The USGS database provides storage window formation thickness data, but two steps are required to calculate SWFT for the GCCC database:

1. Delineate the storage window area (SWA, meters squared): The SWA is the 2D spatial extent calculated from subtracting the depth to top window boundary from depth to formation (DF, meters) input data, as shown in equation 3.3. The SWA boundary delineates the start of the calculated positive results (>0), which means that anything within this SWA boundary is considered for storage. Consideration of the bottom storage window boundary is not necessary, as the formation depth extent cannot exceed the depth to the bottom boundary.

$$SWA = DF - Depth\ to\ top\ boundary \tag{3.3}$$

2. Clip the Formation Thickness (FT) input data utilizing the SWA. The FT input data is then cropped to match the SWT's 2D spatial extent utilizing the ArcGIS's Clip tool.

Area

The area under consideration for this spatial database is an arbitrary, standardized area describing the size and extent of the data. Thus, the area utilized to calculate pressure-based capacity stems from the minimum gridded spatial data resolution found from the input data. In this scope of work, that translates to an area of 25,000,000 m^2 or 25 km^2. This remains constant for all data calculations, regardless of the input data.

Net to Gross Injectable Interval

Net to Gross (N:G) injectable interval is a geological term used to describe the thickness of permeable, prospective reservoir versus the overall interval thickness. This includes both carbonates and siliciclastic sedimentary rock reservoirs. The N:G injectable interval is usually expressed as a percentage or decimal fraction, with higher values indicating a greater proportion of permeable reservoir to non-permeable reservoir. It is an important parameter used in petroleum geology and reservoir engineering for evaluating the quality and potential productivity of a sedimentary rock or reservoir. This parameter is one of the most likely to give unrealistic results. This data is extracted from databases, and outliers of thick sections of high net to gross are screened out as likely the results of inconsistent data mergers (high net to gross from a thin interval applied to a thick interval).

Midpoint Formation Depth

Midpoint formation depth (MPD, meters) is calculated by adding half of the storage window formation thickness (SWFT, meters) parameter to depth to top of formation (DF, meters) input data.

$$MPD = DF + \frac{1}{2}SWFT \tag{3.4}$$

Porosity

Porosity is defined as the percentage of fluid-filled space within a given volume of rock. Over time, the rock is buried and subjected to increasing pressure, thus undergoing compaction. This process generally leads to a reduction of the volume of the rock and as a result decreases its primary porosity. The amount of compaction and porosity reduction depends on the type of rock, maximum depth of burial, diagenesis, and the temperature and pressure conditions. Porosity is extracted from databases and may have errors resulting from extrapolation of data from thin or local intervals (e.g., producing hydrocarbon fields) to a more extensive rock body.

Reservoir Temperature

Reservoir temperature is an input to calculate pressure-based CO_2 storage capacity. Other parameters needed for storage capacity calculations, such as CO_2 density and brine compressibility incorporate reservoir temperature data.

To calculate the reservoir temperature, it is necessary to consider the natural variations in both Earth's crust and its surface. For example, variations in lithology (i.e., sandstone versus granite) and crustal thickness create a range of geothermal gradients throughout Earth's crust. Surface temperatures throughout the United States also experience variations due to seasonal changes and climate. Thus, a

regional geothermal gradient data map [19] and an average surface temperature data map [20] were utilized in this reservoir temperature assessment as input data.

The geothermal gradient (G, °C/km), combined with the average surface temperature (T_S, °C) and midpoint formation depth (MPD, meters) make up the reservoir temperature (T_R, °C) (eq. 3.5).

$$T_R = T_s + \frac{MPD}{1000} * G \tag{3.5}$$

Salinity

Salinity is an input data parameter because it partly determines the allowable pressure increase within a reservoir. The salinity of a brine determines the brine density, which in turn affects the compressibility of a brine. A higher brine compressibility would lower the total allowable pressure increase within a reservoir.

Pressure Increase

In constructing the pressure curves (see Chapter 4 main document, **Figure 4-4**), we accounted for sedimentary compaction and changing brine salinity, which change with depth. The maximum allowable injection pressure, ΔP_{max}, is given by the difference between initial reservoir pressure (assumed here to be hydrostatic) and fracture pressure (here using the lower value given by Eaton's method) [21]. We then include a 10% safety factor to arrive at the pressure increase input to the pressure space calculation.

Pressure in the subsurface increases with depth due to the stress exerted by an increasing overburden of rock and fluid (i.e., brine water) with depth. A hydrostatic pressure gradient, or the pressure exerted by a column of fluid, increases at around 10.52 MPa/km (0.465 psi/ft) for subsurface brines [22]. A lithostatic pressure gradient, or the stress exerted by layers of rock stacked on top of each other, increases at 22.6 MPa/km (1.0 psi/ft) [22]. To find the hydrostatic (P_H, MPa) or lithostatic pressure (P_L, MPa) at a given depth in a reservoir formation, the midpoint formation depth (MPD, meters) parameter is multiplied by the hydrostatic or lithostatic pressure gradient (Eq. 3.6 and 3.7).

$$P_H = 10.52 * \frac{\text{MPD}}{1000} \tag{3.6}$$

$$P_L = 22.62 * \frac{\text{MPD}}{1000} \tag{3.7}$$

However, pore volume in the subsurface is already saturated with fluid; consequently, the injection of CO_2 for storage purposes within this saturated porous volume can lead to the destabilization and fracturing of the rock if the pore volume becomes overpressured. One method to estimate the pressure at which the rock will fracture due to overpressure is by using Eaton's Method [23], summarized in eq. 3.8 below. Eaton's fracture pressure (P_E) is in units of MPa.

$$P_E = \frac{v}{(1-v)} * (P_L - P_H) + P_H \tag{3.8}$$

To calculate the fracture pressure point, Eaton's Method considers three variables: the lithostatic and hydrostatic pressures as discussed above, and Poisson's ratio (v). Poisson's ratio describes the 2D

horizontal to vertical directional stress transmissivity behavior ratio of a rock, with a higher *v* value indicating that the rock transmits more stress vertically than horizontally. Poisson's ratio typically ranges from -1 to 0.5 [24] for different types of solid materials (i.e., metals and minerals), with sandstones, shales, and carbonate rocks averaging around 0.2, 0.3, and 0.3, respectively [25]. Analyses on Mt. Simon formation sandstone cores from the CO_2 sequestration demonstration project at Decatur, IL resulted in a Poisson's ratio between 0.14 to 0.27 [26]. For simplicity, this scope of work will assume a constant Poisson's ratio of 0.25 for all the given reservoir formations.

The difference between Eaton's fracture pressure and hydrostatic pressure is known as effective stress (P_{Ef}, MPa), which translates into the amount of pressure increase within the porous volume required to fracture the rock, as well as the point at which the rock becomes overpressured. Effective stress is summarized in eq 3.9 below:

$$P_{Ef} = P_E - P_H \tag{3.9}$$

As a precaution to avoid overpressure, the pressure increase (P_I) considered for pressure-based CO_2 storage capacity calculations is only 90% of the calculated Eaton's fracture pressure minus the hydrostatic pressure, as described by eq. 3.10 below.

$$P_I = 0.9 * P_E - P_H \tag{3.10}$$

Total Compressibility

Compressibility is the measure of a fluid's or a solid's volume change as a response to pressure changes exerted upon said volume. The porous volume in which the CO_2 is injected and stored will experience increasing pressure, and thus will also be subjected to compressibility. To account for the compressibility of both the fluid ($C_B, \frac{1}{MPa}$) and solid rock unit ($C_R, \frac{1}{MPa}$) in the porous volume as a response to the pressure changes for CO_2 storage capacity calculations, the following relationship is established, where C_T is the total compressibility of the porous volume:

$$C_T = C_R + C_B \tag{3.11}$$

The compressibility of rock and brine calculations is derived from Mathias et al., 2009 [27], who also provide a methodology for estimating pressure buildup due to CO_2 injection for CCS purposes. The equations are as follows:

$$C_R = \frac{0.01411}{(1 + 55.87 * \Phi)^{1.42859}} \tag{3.12}$$

$$C_B = \frac{145}{(7.033 * P_H + 541500 * S - 537 * T_R + 403300)} \tag{3.13}$$

where hydrostatic pressure (P_H) is in psi units, porosity (Φ) is in decimals, and reservoir temperature (T_R) is in degrees Fahrenheit.

CO_2 Density

Calculating the density of a gas or fluid within a reservoir requires consideration of the relationship between pressure, volume, molar mass, and temperature as described by the ideal gas law. The ideal gas law (PV = nRT) assumes that the gas occupies a large volume, and that the intermolecular forces between the particles are negligible. However, at burial temperatures and pressures where CO_2 is stored, the CO_2 is supercritical, and the ideal gas law no longer applies.

To account for the behavior of a non-ideal gas under high temperature and pressure conditions, the compressibility factor (Z) is used as a modifier to the ideal gas law. It is a dimensionless number that represents the deviation of the actual volume occupied by a gas from the ideal volume predicted by the ideal gas law since it reflects the effects of intermolecular forces of a gas at a given pressure and temperature. Z values less than 1 indicate that the gas is more compressible than an ideal gas. The ideal gas law with the compressibility factor Z can be rewritten as:

$$Z = \frac{P * V}{R * T} \tag{3.14}$$

$$P = P_A + P_H \tag{3.15}$$

where P is the final pressure in MPa, V is molar volume cm^3, R is the gas constant 8.314 J/mol-K, and T is temperature in Kelvin (K). Allowable pressure increase (P_A) and hydrostatic pressure (P_H) are discussed in the "Pressure Increase" section.

Several equations of state to solve for density of a gas given pressure and temperature have been proposed in the past couple centuries, (e.g., van der Waals and Peng-Robinson). For this analysis, the Peng-Robinson equation of state [28] was used to calculate CO_2 density. Solving for Z, the Peng-Robinson equation of state is as follows [29]:

$$Z = \frac{1}{(1 - B/Z)} - \frac{A}{B} * \frac{B/Z}{1 + \frac{2B}{Z} - (\frac{B}{Z})^2} \tag{3.16}$$

where A and B are dimensionless forms of empirically determined parameters that depend on the properties of the gas. Rearranging eq. 3.16 to solve for Z results in the following cubic Peng-Robinson equation of state:

$$Z^3 - (1 - B) * Z^2 + (A - 3B^2 - 2B) * Z - (AB - B^2 - B^3) = 0 \tag{3.17}$$

With the real solution of Z from eq 3.17, the molar weight of CO_2 (44 g/mol), and a re-arranged version of eq. 3.17 to solve for V, CO_2 density ($\rho_{CO2}, \frac{kg}{m^3}$) can be calculated:

$$\rho_{CO2} = \frac{44000 * P}{Z * R * T} \tag{3.18}$$

CO_2 Injectivity Methods

Injectivity describes the ability of a fluid or a gas to be injected into and through a porous volume in the subsurface. The easier it is for the fluid or gas to be able to flow within the porous volume, the higher the rate of injection, which means higher injectivity of said fluid or gas. Injectivity is influenced by several factors, including the physical properties of the geologic reservoir (i.e., permeability and the net to gross injectable interval within the reservoir thickness), the pressure and temperature of the fluid or gas, and the presence of impurities in the fluid or gas.

Quantifying CO_2 injectivity is important for the development of new CCS projects. Quantification of CO_2 injectivity can help determine how many wells are needed per project to reach defined storage goals over time (i.e., 1 million tons of CO_2 for 20 years).

Calculating CO_2 Injectivity

Injectivity is usually calculated from field injection and pressure data from a well. Previous injectivity studies [30, 31] focused on the injectivity index (J) to characterize the capability of a well to inject fluid into a reservoir. Reservoir properties such as permeability, size, thickness, well properties (diameter and design), skin factor, two phase relative permeability, friction, and pressure drop from the wells are considered. The injectivity index (J) as a radial steady state flow around a vertical well [30] is summarized below in eq. 4.1, where *k* is permeability, *h* is thickness, and the denominator variables are related to the formation and bottom hole pressure:

$$J = \frac{q}{(p_e - p_{wf})} = \frac{k * h}{141.2 * B_o * \mu_o * \left(ln\frac{r_e}{r_w} + S\right)} \tag{4.1}$$

However, well pressure data is not readily available at a regional level, and so the injectivity calculations for this scope of work have been simplified to depend solely on the permeability and thickness of the reservoir. Previous work has demonstrated that injectivity calculations based on permeability and thickness are a good simplified proxy to the injectivity index, since the relationship between injectivity and permeability and thickness is linear [31, 32]. By eliminating the denominator in eq. 4.1 into this simplified version, the uncertainties associated with each variable in the final product are reduced.

Thus, in this study, CO_2 injectivity (I) is estimated by multiplying the permeability (*k*, millidarcy) of the porous volume by the storage window formation thickness (SWFT, meters) and the net to gross injectable interval (N:G) as shown in eq. 4.2 below. CO_2 injectivity is in units of millidarcy-meters, which is abbreviated as mD-m.

$$\mathrm{I} = k * SWFT * N{:}G \tag{4.2}$$

CO_2 Injectivity Parameters

SWFT and N:G are also CO_2 storage cost estimation input parameters, which have been discussed above. The remaining parameter is permeability.

Permeability

Permeability of a rock refers to the ability of a rock to allow fluids, such as water or gases, to pass through it. It is a measure of the pressure drop required to drive fluid flow through a material. For this analysis permeability is derived from databases and has the same problems as porosity in that the available data may not be representative of the entire the region.

Plume Shape

The nature of the geometry of the subsurface flow units and the way that CO_2 is emplaced has an impact on the "footprint" occupied by the CO_2 plume (shown in green in **Figure A4-3**). In case A of the figure, the thick injection zone has no sedimentary layering, so the plume rises to the top and "pancakes" out into a large footprint. In contrast, case B has many discontinuous layers, and CO_2 injected at the base of the stack develops a plume that spreads beneath each layer. In case C, the operator has deliberately injected into many zones to make the footprint small. In case D, the operator has chosen a domed "trap" to make the footprint small. In A, B, and C, the spread of the CO_2 plume over time results in it becoming trapped in the pores and unable to move. In D, the CO_2 is concentrated and remains mobile.

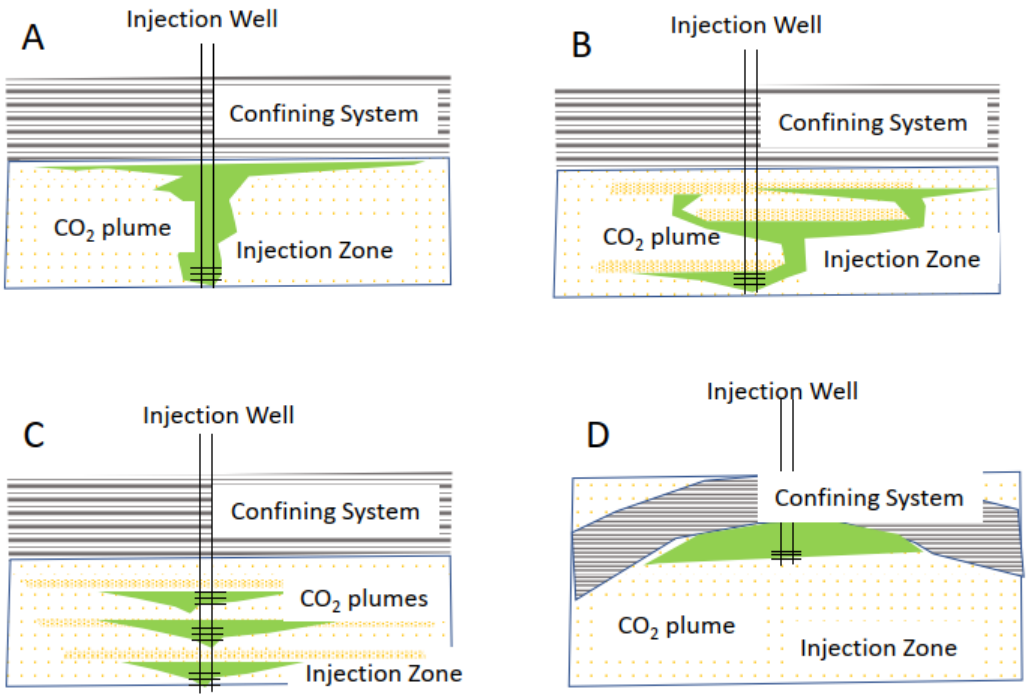

Figure A4-3. CO_2 plume shape.

Estimating Project Costs Over the Project Lifetime

To estimate the costs of a geologic storage project over the project lifetime, we accounted for costs accrued during each project phase: exploration, development, operation, closure, and post closure. Experience with this process is sparse, and almost all projects are first-of-a kind and cannot inform costs for mature projects.

Mean Storage Cost Estimation Methods.

Development of a CO_2 capture and storage project is a complex process that involves multiple phases: exploration for a storage site location; site development and permitting; operation; and post injection. We approach cost as the sum of the costs in each phase. Data tables were built based on calculated injectivity, and the corresponding number of wells required to achieve injection of 1 million tons CO_2/year for 20 years and project area-based plume and pressure space parameters. Injection volume-based parameters are set for our 1 million tonne unit project and are independent of the number of wells and area.

Exploration for a Storage Site Location

Exploration cost has rarely been included as a cost in past assessments. Most assessments assume that a site has been identified. Inventories by Hovorka and Barnhard [33] show that for many sites, initial characterization to show that a site is viable can be very low cost because analysis of existing data is effective in de-risking sites. However, in areas with minimal subsurface data, for example where exploration for hydrocarbons has not been conducted, data are limited. This is the case for large areas of our study where mapping identifies sedimentary rocks in the storage window. We assume that twice as many seismic lines need to be collected to characterize these places with sparse data, compared to areas where existing data can be purchased, and that this would be used to guide injection well location selection.

For poorly understood areas, we assume that exploration costs include acquisition of two seismic lines across the project pressure space and drilling a stratigraphic test well, which we assume is re-used as a project well. We assume three such exploration projects will be needed to find one viable storage site.

A small number of test wells have been drilled in underexplored areas, for example in Arizona, New Jersey, and Georgia. Not all test wells will lead to the discovery of a storage resource, and the number of unsuccessful wells required to locate successful storage is poorly constrained. We assume the success rate for exploration for geologic storage is somewhat higher than the success rate for oil and gas because water-filed pores are more common than hydrocarbon accumulations and because a significant amount of existing data is available. We therefore set the success rate at 1 in 4, adding the cost of drilling and characterizing three unsuccessful wells to the cost of drilling, characterizing, and operating the successful well.

For the development phase, we assume costs include collecting the data required to submit a Class VI injection permit, including data needed to constrain a fluid flow model, and drilling the number of injection wells required to emplace the volume at the spacing needed to sustain injection for 20 years. We assume that all the data needed is collected in one operation, so cost is not per well but per storage project. Similarly, we assume that a total of two monitoring wells will be required per storage project regardless of the number of injection wells, rather than each injection well needing a corresponding monitoring well. This cost reduction is viable because the information and data gathered from multiple injectors will build knowledge about the subsurface.

Operation Phase

For the operation phase, we assume costs include monitoring, pore space leasing, insurance, and community benefits. We reviewed most of the publicly available monitoring plans in permits and

conclude that deployments are diverse. We therefore do not attempt to prescribe and cost a selected monitoring array because it is clear this will be negotiated with the regulator and be unique to each project. We assume that the bulk of monitoring costs will be related to geophysical surveys to track the CO_2 and pressure plumes, but that repeat 3D seismic surveys (which are among the most expensive monitoring techniques) will not be required.

We include three major operational costs indicated by evolving projects but not considered in previous studies: (1) fees paid to the surface landowner to lease or gain an easement on use of the subsurface, (2) insurance or bonding, and (3) benefits paid to host communities. Data on leasing costs are sparse, and most transactions are private. Few jurisdictions have requirements specifying the terms for such leases, with only a handful of states having a specified per ton fee to be paid or put in various bonds, trust funds, or escrow accounts. For this analysis, we assume a pore space lease cost of \$7,500/km^2, a bonus of \$2,000/km^2 for 20 years, and a landowner fee of \$3.00/ton of CO_2. Storage project operators will need insurance for field operations similar to that for oil and gas operations. Project financiers may require insurance or bonding to offset the risk that the project does not receive the full payment from incentive programs, for example the International Revenue Service 45Q tax credit or the California Low Carbon Fuel Standard. Non-payment would occur if the project failed to document retention of the injected CO_2 and insurance to de-risk this is now available [34]; however, we did not obtain a quote for this study. For this analysis, we assume insurance and closure fees of \$0.10/ton CO_2. Community benefits costs are the most poorly constrained in this phase. Some support to the community is a normal part of doing business, for example, sponsoring local activities. United States Department of Energy CarbonSAFE awards [35] now require documentation of community benefits provided as part of the project, but the range of available information is too small to yet compile statistics on the cost range. For this analysis, we assumed a community benefits fee of \$0.10/ton of CO_2.

Closure Phase

For the closure phase of geologic storage projects, we assume costs include well plugging and abandonment, removal of surface equipment, and restoration of the surface. Class VI permits and the California Low Carbon Fuel standard include requirements for a Post Injection Site Care (PISC) period (default 50 years and required 100 years, respectively) during which monitoring must be done. The range of costs for this monitoring could be broad, depending on the specific requirements. Our assessment assumes that commercial projects will control this cost with advanced monitoring techniques and that effort will be minimal once it has been demonstrated that the CO_2 and pressure plumes have stabilized. We therefore do not place high costs in closure and post-closure project phases; however, disagreement and uncertainty about this assumption are noted.

Well Drilling Costs

Well drilling and completion costs are a composite of many individual costs that vary over time. Costs are non-linear with depth, with the shallow portion of the well costing more than the deeper zones due to the need to use large diameter steel casing to protect shallow freshwater [36]. Factors such as site accessibility, weather, fluctuating materials and labor cost, and economic conditions all impact overall cost. Components of total cost include equipment mobilization, site preparation, well engineering, casing and cement, drilling, and contingency (trouble mitigation) costs. We estimate drilling rig-related costs of \$0.9- \$1.3 million [37] with the range influenced by drilling efficiency, well depth, fuel costs, and rig and crew rates driven by market conditions. We estimate casing costs of \$0.6–1.2 million with the range

influenced by steel price, well dimensions, and number of casing strings. Finally, we estimate 25% "other" costs such as insurance, consulting, surface equipment, completion tools, drilling, facilities, and artificial lift.

Given the complexity of well cost, we did not attempt to provide project-specific drilling costs but instead use reported average well costs. However, available recent onshore US well drilling costs are dominated by wells that are designed to extract hydrocarbons from unconventional reservoirs, which include costs for hydraulic fracturing, including proppant, pumps to fracture the reservoir, completion fluids, and flow back fluids. These costs represent 38–50% of the total cost but are not relevant to geologic CO_2 storage wells. Based on recent well drilling and completion costs, we estimate storage well costs of $3,725,000 per well plus or minus 50%. This uncertainty is greater than the plus or minus 23% uncertainty from published data, but we believe the greater uncertainty is justified by our inclusion of geologic basins with sparse existing data.

Additional costs for well testing, evaluation, and analysis are small compared to the other drilling and completion costs, so they are rolled into the well drilling costs rather than being calculated separately.

Project Area-based Costs

Seismic Surveys

Collection of seismic surveys are a current best practice in oil and gas exploration. CCS project developers may choose to acquire seismic; however, it is not explicitly required for permitting. We assume that two new 2D seismic lines will be collected over the project area to the edge of the pressure space and that one 3-D seismic survey will be collected over the area of the CO_2 plume but not into the area of elevated pressure. This is in addition to leasing any available exiting good quality data.

Cost of collection and leasing of both 2D and 3D data is not well constrained in the public literature. Many variables go into the cost of collecting seismic data, such as line spacing, resolution, bin size, source type, quality control, acquisition equipment, labor costs, processing, and interpretation. These parameters are designed for specific projects and then bid competitively. We assume that the size of the 3D survey will be 2 km greater than the CO_2 plume area to ensure data is acquired over the entire area of interest. We amalgamated data by informal personal inquiries and used a cost of $15,625/km plus or minus 100% for 2D surveys and a cost of $100,000/km plus or minus 150% for 3D surveys.

We assume that the 3D survey will be repeated two times, once early in the project and once at project end. The best practice and permit requirements are highly uncertain and intensely debated; technological advances such as the use of fiber to replace seismic receivers and fixed sources to collect less aerially dense data that can be used to meet regulatory expectations may be a "game changer."

Monitoring Wells

Best practice regarding the number of monitoring wells is likewise difficult to constrain or predict. Class VI rules require operators to drill and use monitoring wells for various functions, but the exact number is determined on a project by project basis. We assume that two monitoring wells are drilled in each 100km^2 project area, one deep well and one shallower "above zone" well. We assume that within the uncertainty range, monitoring wells cost the same as injection wells, although some differences in engineering are certainly expected. Fresh water monitoring well costs are small and rolled into the uncertainty as are sampling and analytical costs.

Pore Space Leasing

Payment to the surface owner to lease the pore space is a cost that has not widely been previously assessed and data are extremely limited. Legal requirements to obtain such leases are uncertain. In water and waste disposal, no lease other than the immediate wellsite is required. However, states are beginning to set rules for leasing the pore space occupied by CO_2. For some projects such as QUEST in Canada, the leased acreage is greater than the pressure space of the project. The per acre fee is also being negotiated privately and only sparse data is available. The amalgamation of opinions in the Gulf Coast produced a type fee structure of option (pre development) of $20–50 per acre, bonus at development of $300–1000 per acre over the plume area, and royalties $1.50 $2.00 per ton of CO_2.

Per Ton Fees

Also new to costing are fees that are paid per ton. We include the royalty fee mentioned above, permitting fees, insurance, bonding, trust funds, and community benefits.

Royalty Paid to Landowner

We assumed royalties of $1.50 $2.00 per ton. A survey in California produced higher numbers [38]. For this project, we used $3 per ton for the plume area plus or minus 100%.

Permitting Fees, Insurance, Bonding, Trust Funds

States are setting up various mechanisms to pay for the cost of administering and permitting geologic storage projects as well as assuring that projects reach closure without requiring public investment. Project financiers are beginning to purchase insurance to offset the risk that they will not get the full financial benefit of the project because of either failure to retain the CO_2 or failure to complete the requirements to get this payment [34]. In addition, projects need insurance for operational risks, such as injury to workers or damages. We did not attempt to collect data in detail but assumed a cost of $0.10 per ton as a placeholder.

Community Benefits

The Department of Energy has been requiring projects to develop community benefits plans as part of the process of competing for funding to offset costs. [35] Data on what has been planned for successful applicants has not been made public yet, nor has any standard been set; this practice will continue for non-federally funded projects. We set a placeholder of $0.10 per ton.

Cost Calculation

Table A4-4. Map inputs to project-based storage cost.

Category	Abbr.	Item	Cost ($USD)
Development	D	Injection well per 1 well	$ 3,725,000.00/well
Exploration	E_{2D}	2-D seismic survey, per km, per line	$15,625.00/km
	E_{3D}	3-D seismic survey per km2	$100,000.00/ km^2
Monitoring	M	Monitoring per km2 of project area for 20 years	$8,580,00.00/ km^2
Pore space lease	PS	Pore-space lease per km^2	$7500.00/ km^2

	PS_b	Bonus per km2 for 20 years	$2000.00/km^2
	PS_L	Landowner fee per ton of CO_2	$3.00/ton
Closure	C	Insurance and closure fee per ton of CO_2	$0.10/ton
Community benefits	Com	Community benefits fee per ton of CO_2	$0.10/ton

Cost Table

Using **Table A4-4** input values, costs were applied to the injectivity and project area data in ARC GIS using Python script. Exploration costs were applied to the prospective areas only, although it is likely that exploration costs should be applied to areas of known basins where data were extrapolated between clustered data points. In some areas, costs are calculated for individual sample points on a grid, in other areas, costs are applied to polygons.

The storage costs per project, in units of $MM USD (millions of U.S. dollars), are then calculated by adding all cost categories together, as indicated in eq. 5.4 below.

$$Storage\ Costs\ per\ Project = Dev + Exp + Mon + Lease + Closure + Community \quad (5.4)$$

$$Dev = Wells * D \quad (5.4a)$$

$$Exp = \left(\sqrt{A_{Proj}} + 2\right) * E_{2D} + 2 * ((A_{Proj} * 0.05) + 6) * E_{3D} \quad (5.4b)$$

$$Mon = \left(\frac{A_{Proj}}{100}\right) * M + M \quad (5.4c)$$

$$Lease = ((A_{Proj} * 0.05) + 4) * (PS + PS_B) + 20{,}000{,}000 * PS_L \quad (5.4d)$$

$$Closure = 20{,}000{,}000 * C \quad (5.4e)$$

$$Community = 20{,}000{,}000 * C_B \quad (5.4f)$$

CO_2 Storage Costs per Ton

To calculate storage costs per ton, the total storage costs per project are divided by the assumed CO_2 injection rate per year and the expected longevity of the project, which are 1 million tons per year for 20 years. Units of storage costs are in $USD per ton of CO_2.

REFERENCES

1. *WG Allinson, DN Nguyen, and J Bradshaw, The economics of geological storage of CO2 in Australia. The APPEA Journal, 2003.* ***43****(1): p. 623-636, https://doi.org/10.1071/AJ02035.*

2. *Bert Bock, et al. Economic Evaluation of CO2 Storage and Sink Enhancement Options. 2003. United States; 10.2172/826435. https://www.osti.gov/biblio/826435.*

3. *Sara Budinis, et al., An assessment of CCS costs, barriers and potential. Energy Strategy Reviews, 2018. **22**: p. 61-81, https://doi.org/10.1016/j.esr.2018.08.003.*

4. *R. T. Dahowski, et al. Building the Cost Curves for CO 2 Storage: North America (Report Number 2005/3). 2005. IEA Greenhouse Gas R&D Programme, https://www.researchgate.net/publication/233920536_Building_the_Cost_Curves_for_CO_2_Storage_North_America.*

5. *Jordan K. Eccles, et al., The impact of geologic variability on capacity and cost estimates for storing CO2 in deep-saline aquifers. Energy Economics, 2012. **34**(5): p. 1569-1579, https://doi.org/10.1016/j.eneco.2011.11.015.*

6. *Richard S. Middleton and Jeffrey M. Bielicki, A scalable infrastructure model for carbon capture and storage: SimCCS. Energy Policy, 2009. **37**(3): p. 1052-1060, https://doi.org/10.1016/j.enpol.2008.09.049.*

7. *Tim Grant and David Morgan. FE/NETL CO2 Saline Storage Cost Model (2017): User's Manual (DOE/NETL 2017/1582). 2017. Pittsburgh, PA; Morgantown, WV, USA; National Energy Technology Laboratory (NETL); https://www.osti.gov/biblio/1557137.*

8. *Tim Grant. Quality Guidelines for Energy System Studies: Carbon Dioxide Transport and Storage Costs in NETL Studies (DOE/NETL-2019/2044). 2019. Pittsburgh, PA; Morgantown, WV, USA; National Energy Technology Laboratory (NETL); 10.2172/1567735. https://www.osti.gov/biblio/1567735.*

9. *Susan D. Hovorka, et al. Sequestration of Greenhouse Gases in Brine Formations: CO2 Brine Database. Accessed July 2023 Published by Gult Coast Carbon Center (GCCC) (The University of Texas at Austin - Jackson School of Geosciences); Available from https://gccc.beg.utexas.edu/research/brine-main.*

10. *Sean T. Brennan, et al. A Probabilistic Assessment Methodology for the Evaluation of Geologic Carbon Dioxide Storage: U.S. Geological Survey Open-File Report 2010–1127. 2010. U.S. Geological Survey, Reston, Virginia: 2010, http://pubs.usgs.gov/of/2010/1127.*

11. *NETL, NATCARB/Atlas carbon storage atlas. 2015: https://www.netl.doe.gov/coal/carbon-storage/strategic-program-support/natcarb-atlas.*

12. *Inge E. M. de Graaf, et al., A global-scale two-layer transient groundwater model: Development and application to groundwater depletion. Advances in Water Resources, 2017. **102**: p. 53-67, https://doi.org/10.1016/j.advwatres.2017.01.011.*

13. *Claire Porter, et al., ArcticDEM, Version 3. 2018, Harvard Dataverse (https://doi.org/10.7910/DVN/OHHUKH).*

14. *USGS. 3DEPElevation (ImageServer). Accessed July 2023 Published by ArcGIS REST Services Directory; Available from https://elevation.nationalmap.gov/arcgis/rest/services/3DEPElevation/ImageServer.*

15. *G. Laske and G. Masters, A global digital map of sediment thickness. Eos Trans. AGU, 1997. **78**: p. F483, http://igppweb.ucsd.edu/~gabi/sediment.html#sed.*

16. *Stephen Marshak, et al., The basement revealed: Tectonic insight from a digital elevation model of the Great Unconformity, USA cratonic platform. Geology, 2017. **45**(5): p. 391-394, https://doi.org/10.1130/G38875.1.*

17. *Anjana K. Shah and Oliver S. Boyd. Depth to basement and thickness of unconsolidated sediments for the western United States—Initial estimates for layers of the U.S. Geological Survey National Crustal Model. 2018. Open-File Report; U.S.G. Survey, Reston, VA; 10.3133/ofr20181115. http://pubs.er.usgs.gov/publication/ofr20181115.*

18. *Lauri A Burke, et al., Regional map of the 0.70 psi/ft pressure gradient and development of the regional geopressure-gradient model for the onshore and offshore Gulf of Mexico Basin, USA. GCAGS Journal, 2012. **1**: p. 97-106, https://archives.datapages.com/data/gcags-journal/data/001/001001/pdfs/97.htm.*

13. *Richard S. Middleton, et al., Effects of geologic reservoir uncertainty on CO2 transport and storage infrastructure. International Journal of Greenhouse Gas Control, 2012. **8**: p. 132-142, https://doi.org/10.1016/j.ijggc.2012.02.005.*

14. *Richard S. Middleton and Sean Yaw, The cost of getting CCS wrong: Uncertainty, infrastructure design, and stranded CO2. International Journal of Greenhouse Gas Control, 2018. **70**: p. 1-11, https://doi.org/10.1016/j.ijggc.2017.12.011.*

15. *Richard S. Middleton, et al., SimCCS: An open-source tool for optimizing CO2 capture, transport, and storage infrastructure. Environmental Modelling & Software, 2020. **124**: p. 104560, https://doi.org/10.1016/j.envsoft.2019.104560.*

16. *Richard S. Middleton, et al., Great SCO2T! Rapid tool for carbon sequestration science, engineering, and economics. Applied Computing and Geosciences, 2020. **7**: p. 100035, https://doi.org/10.1016/j.acags.2020.100035.*

17. *Carbon Solutions. SCO_2T^{PRO}. Accessed July 2023 Published by Carbon Solutions; Available from https://www.carbonsolutionsllc.com/software/sCO2t/.*

18. *Nehring Associates. The Significant Oil and Gas Fields of the United States Database. Accessed July 2023 Published by Nehring Associates; Available from https://www.nehringdatabase.com/.*

19. *DD Blackwell and M Richards, Geothermal Map of North America, AAPG Map, scale 1:6,500,000, Product Code 423. 2004 (https://www.smu.edu/-/media/Site/Dedman/Academics/Programs/Geothermal-Lab/Graphics/Geothermal_MapNA_7x10in.gif).*

20. *Stephen E. Fick and Robert J. Hijmans, WorldClim 2: new 1-km spatial resolution climate surfaces for global land areas. International Journal of Climatology, 2017. **37**(12): p. 4302-4315, https://doi.org/10.1002/joc.5086.*

21. *Jincai Zhang and Shang-Xian Yin, Fracture gradient prediction: an overview and an improved method. Petroleum Science, 2017. **14**(4): p. 720-730, https://doi.org/10.1007/s12182-017-0182-1.*

22. *Djebbar Tiab and Erle C. Donaldson, Chapter 2 - Introduction to Petroleum Geology, in Petrophysics (Fourth Edition), D. Tiab and E.C. Donaldson, Editors. 2016, Gulf Professional Publishing: Boston. p. 23-66 (https://doi.org/10.1016/B978-0-12-803188-9.00002-4).*

23. *Ben A Eaton and Travis L Eaton, Fracture gradient prediction for the new generation. World Oil, 1997. **218**(10): p. 93-97, ISSN: 0043-8790.*

24. *I.S. Sokolnikoff, Mathematical Theory of Elasticity (2nd ed. reprint). 1983: R.E. Krieger Publishing Company (ISBN-13: 978-0070596290). 476.*

25. *Schlumberger Energy Glossary. https://glossary.slb.com/*

26. *Carolyn A. Morrow, et al. Physical properties of sidewall cores from Decatur, Illinois. 2017. Open-File Report; U.S.G. Survey, Reston, VA; 10.3133/ofr20171094 (https://pubs.er.usgs.gov/publication/ofr20171094).*

27. *S. A. Mathias, et al. Screening and selection of sites for CO2 sequestration based on pressure buildup. International Journal of Greenhouse gas control, 2009, 3(5), 577-585. https://doi.org/10.1016/j.ijggc.2009.05.002*

28. *Ding-Yu Peng and Donald B. Robinson, A New Two-Constant Equation of State. Industrial & Engineering Chemistry Fundamentals, 1976. **15**(1): p. 59-64, https://doi.org/10.1021/i160057a011.*

29. *J Richard Elliott and Carl T Lira, Chapter 7 - Engineering Equations of State for PVT Properties, in Introductory Chemical Engineering Thermodynamics (2nd edition). 2012, Pearson Prentice Hall: Upper Saddle River, NJ; ISBN-13: 978-0-13-606854-9 (Available at https://chethermo.net/screencasts/chapter7).*

30. *Boyun Guo, Kai Sun, and Ali Ghalambor, Well productivity handbook: vertical, fractured, horizontal, multilateral, multi-fractured, and radial-fractured wells (1st edition). 2008, Houston, Texas, USA: Gulf Publishing Company. ISBN-13: 978-1933762326 (https://industri.fatek.unpatti.ac.id/wp-content/uploads/2019/03/228-Well-Productivity-Handbook-Boyun-Guo-Kai-Sun-Ali-Ghalambor-Edisi-1-2014.pdf); 368*

31. *Manoj Valluri, Srikanta Mishra, and Priya Ravi Ganesh, Injectivity index: a powerful tool for characterizing CO2 storage reservoirs—a technical note. Greenhouse Gases: Science and Technology, 2021. **11**(2): p. 251-265, https://doi.org/10.1002/ghg.2046.*

32. *Nick Hoffman, et al., Site Characterisation for Carbon Sequestration in the Nearshore Gippsland Basin, in International Conference and Exhibition, Melbourne, Australia 13-16 September 2015. p. 265-265 (https://doi.org/10.1190/ice2015-2209980).*

33. *S.D. Hovorka, T. Barhart, and SECARB USA Team. Early-stage cost of storage project characterization. (2022). pgs. 13. Proceedings of the16th Greenhouse Gas Control Technologies Conference (GHGT-16). Lyon, France https://dx.doi.org/10.2139/ssrn.4284960.*

34. *Marsh. Solutions: Carbon Capture and Storage Insurance. Accessed July 2023 Published by Marsh; Available from https://www.marsh.com/us/industries/energy-and-power/products/carbon-capture-storage-insurance.html.*

35. *US DOE Office of Fossil Energy and Carbon Management (FECM). Funding Notice: Bipartisan Infrastructure Law: Carbon Storage Validation and Testing. Accessed July 2023 Published by US DOE FECM; Available from https://www.energy.gov/fecm/funding-notice-bipartisan-infrastructure-law-carbon-storage-validation-and-testing.*

36. *M Enamul Hossain and Abdulaziz Abdullah Al-Majed, Fundamentals of sustainable drilling engineering. 2015, Hoboken, NJ and Salem, MA: John Wiley & Sons, Inc. and Scrivener Publishing, LLC. https://onlinelibrary.wiley.com/doi/book/10.1002/9781119100300; 754.*

37. *IHS Markit. Rising Oil Prices and Cost Efficiencies Driving Greater Global Demand for Offshore Drilling Rigs through 2020, IHS Markit Says. 2018 Published by S&P Global; Available from https://news.ihsmarkit.com/prviewer/release_only/slug/energy-rising-oil-prices-and-cost-efficiencies-driving-greater-global-demand-offshore-.*

38. *B. Grove and G. Peridas. Sharing the Benefits: How the Economics of Carbon Capture and Storage Projects in California Can Serve Communities, the Economy, and the Climate. 2023. LLNL-TR-848983, https://gs.llnl.gov/sites/gs/files/2023-05/ca-ccs-economic-study-report.pdf.*

APPENDIX—CHAPTER 5

This paper intentionally left blank.

APPENDIX—CHAPTER 6

Methods for Paper and Paperboard Assessment, CRP and Marginal Land Identification, and Biomass Economic Modeling Approach

The total amounts of paper/paperboard waste that are captured for recycling was estimated based on the United States Environmental Protection Agency Paper and Paperboard: Material-Specific Data [1]. Data from this source was for the year 2018. The source reported total paper and paperboard generated, recycled, composted, and combustion with energy recovery and landfilled. The total non-recycled paper and paperboard for the year 2018 was assumed/calculated to be the total amount that is considered combustion with energy recovery and landfilled (which was approximately 21.4 million US tons). Then based on country population for the year 2018, this total paper/paperboard was broken down by population. The total amount of non-recycled paper/paperboard was divided by the total 2018 population, and this factor was then multiplied by the population of each county. This determined how much non-recycled paper/paperboard was available for each county. Using population growth statistics from the US Census, this amount of paper/paperboard was projected to the appropriate years.

To determine the associated price of the non-recycled paper/paperboard, a similar method to the 2016 Billion Ton approach was utilized for which a negative tipping fee is added to a positive sorting cost; however, a few adjustments were adapted. There was no artificial price floor assumed. It was allowed to have a small or negative price; there is no reason why the costs could not go low, and there is historical precedent for this. Updated state-level tipping fees produced by EREF was utilized [2]. Instead of the original $40 and $60/ton sorting cost from the 2016 Billion Ton approach, a low end of $60 and a high end of $80/ton was utilized as a result of this source [3]. The final adjustment made was that instead of using total population to determine the sorting cost, population density was utilized. Population density by county was determined from the US Census. The cutoff for population density was 1000 people per square mile. For counties where the population was greater than 1000 people per square mile, a sorting fee was calculated by the following formula, Sorting Fee = 0.5*(-tipping fee + 60) + 0.5*(-tipping fee +80). It was assumed that this price for non-recycled paper/paperboard would remain constant over time. This assumption was made for ease of calculation because it is difficult to understand how these prices will change in the future.

Conservation Reserve Program Methods

We assumed only native herbaceous grasses as potential biomass sources on Conservation Reserve Program (CRP) lands. We assume mixed native grass regimes that are already established in CRP lands can be harvested for biomass. We compare land use under a biomass harvesting scenario to a status quo baseline scenario for which land can either re-enroll or convert to other uses (annual crops or pasture).

The 2021 FSA USDA report was used to establish baseline grassland CRP acreage, rental rate, and re-enrollment dates [4]. By 2031, 7.45 million hectares of CRP land will expire. In the status quo baseline case, expiring CRP lands can either convert to conventional crops, pastureland, or re-enroll in CRP. In the biomass scenario, re-enrolled CRP lands can harvest existing grasses annually. We run both the baseline scenario and the biomass scenario and compare the two to calculate net change.

We used the System Approach to Land Use Sustainability (SALUS) model [5] to estimate the potential yield and soil carbon changes in the identified CRP fields. SALUS is a process-based crop and biogeochemical model designed to simulate crop growth and development, and carbon, water, and nutrient fluxes on a daily time step basis. Model inputs are daily values of incoming solar radiation (MJ m-2), maximum and minimum air temperature (°C), and rainfall (mm), as well as information on soil characteristics, genotype, and agronomic management. The SALUS model has been validated for several crops and management practices [5] and was previously used to spatially simulate switchgrass yields across Michigan [6] and to evaluate soil carbon sequestration from switchgrass across the US Midwest [7], [8]. For CRP sites, SALUS assumed mature grass stands effectively modeled as switchgrass. Twenty percent of biomass yields were left unharvested for wildlife. Switchgrass is planted every 15 years, and the planting year and subsequent year are considered establishment years and are lower yielding. The plant is harvested annually, and agronomic yields are reported.

Economic Modeling of Carbon Crops

We use the POLYSYS socio-economic model to simulate the implications of biomass harvesting policies on US cropland acreage and commodity prices. POLYSYS is a simulation model of US agriculture that includes the eight conventional crops that make up 90% of US cropland acreage, arable non-irrigated pastureland, and CRP in grasslands. POLYSYS land use decisions are made at the county level through individual linear programming models. Regional crop budgets, county average yields, and naïve price expectations are used to determine profitability ranking. POLYSYS iterates annually through 2050 with annual productions totaled nationally used in a national econometric module to simultaneously determine equilibrium commodity prices and sector demands, including exports. Through this mechanism, land changes and price impacts of agricultural policies can be determined for unique national biomass prices offered. For this analysis, biomass prices are simulated at prices ranging from $37 per dry ton to $183 per dry tonne biomass (corresponding to biomass prices of $20 to $100 per tonne CO_2) [9].

We estimated yields on CRP lands for both conventional crops and biomass crops considering the soil quality of individual CRP fields. For estimating conventional crop yields on CRP lands, we have correlated the yield of each major crop to National Crop Productivity Index (SURRGO) values [10]. We adjust the county-level crop yield on CRP lands down from the county weighted average yield by the difference in NCCPI value of the soils between cropland and CRP lands.

Marginal Land Identification Methods

The combination of land identified in the USDA Land Capability Classes and abandoned land from the GLBRC Bioenergy Lands Atlas provides a significant opportunity to supply greater biomass production through high-yielding switchgrass on these lands without competing with food production. Existing native mixed species grasses are assumed for areas with a significant amount of land in native species (more specifically, the Sandhills of Nebraska and the Flint Hills of Kansas). We exclude arid lands from consideration due to low productivity and the likelihood that they are currently used for livestock production. Additional constraints to the locations included the removal of publicly owned land, highly sloped landscapes, forests, and wetlands.

Biomass yields on marginal lands are estimated for switchgrass with SALUS, as earlier described for the CRP approach. Economic outcomes are estimated for this approach using POLYSYS as described earlier for the CRP approach.

Maximum Economic Potential Methods

The maximum potential assessment assumes any crop or pastureland can be brought into biomass production if biomass offers the highest economic return in a region. High-yielding switchgrass, poplar, and willow varieties are considered as potential biomass sources on crop and pasture lands. Yields were estimated on prime farmland using the PRISM model (methods can be found in the 2016 Billion-ton Report) and are higher than marginal land yields in the marginal scenario and the mixed grass yields in the CRP scenario. Cropland that converts to perennial grasses will accumulate soil carbon and is paid an incentive for CO_2 reduction. The incentive level corresponds to the equivalent biomass price paid for the carbon; for example a $73 per dry tonne biomass price equates to an CO_2 incentive rate of $40 per metric ton CO_2 (*i.e. $73/tonne biomass * 1 tonne biomass/0.5 tonne C * 12 tonne C/44 tonne CO_2*). Soil carbon accumulation rates were calculated at the sub-county level using the SALUS biogeochemical model as noted for prior scenarios, above.

We assume the regional number of livestock will not be impacted by pastures converting to biomass crops due to intensification of grazing on local pasture. The cost of pasture intensification in the model is paid by biomass crops; we assume that 1.5 acres of pasture need to be intensified for every one acre of land converting to biomass. The cost of intensification is a first-year cost of $100 per acre for pasture (fencing, water, management) and $15 per acre for future years (pasture management).

We show the annual biomass production of switchgrass, willow, and poplar according to the maximum potential assessment in **Figures A6-1, A6-2**, and **A6-3**.

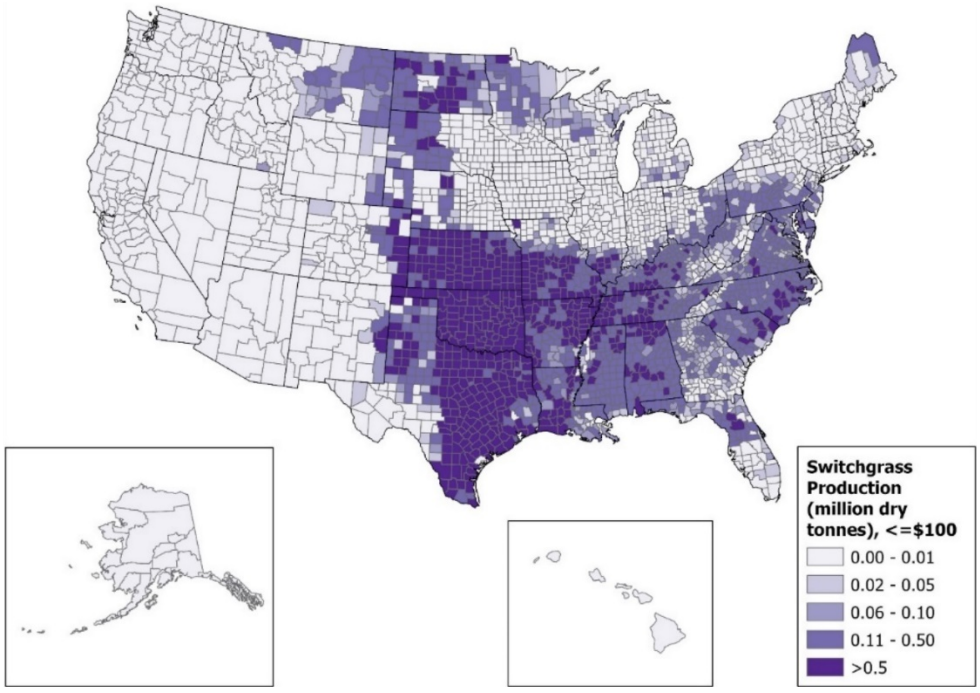

Figure A6-1. Map of maximum potential biomass production from switchgrass at $100 per dry tonne.

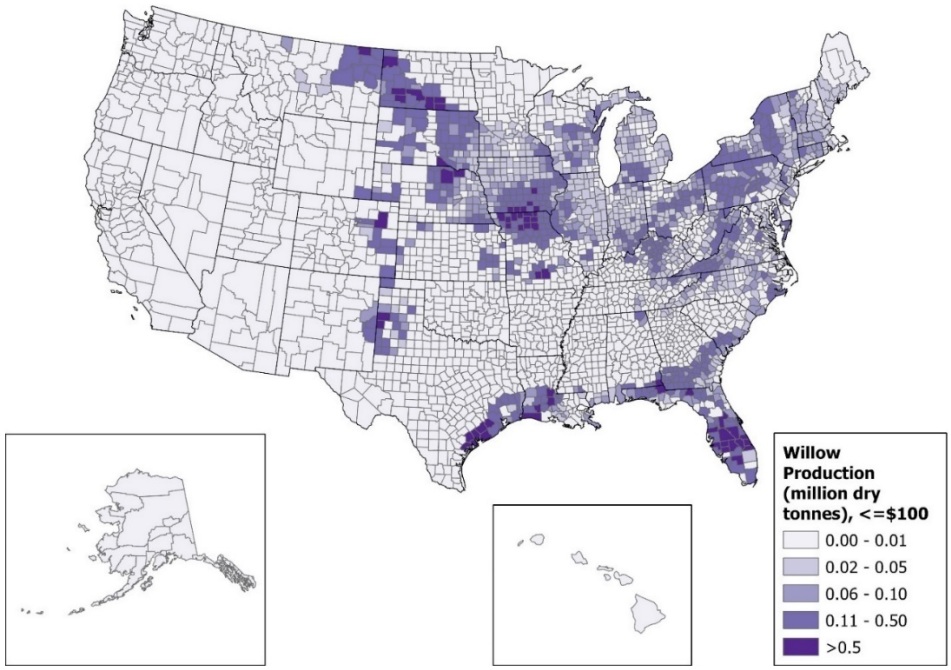

Figure A6-2. Map of maximum potential production from willow trees at $100 per dry tonne.

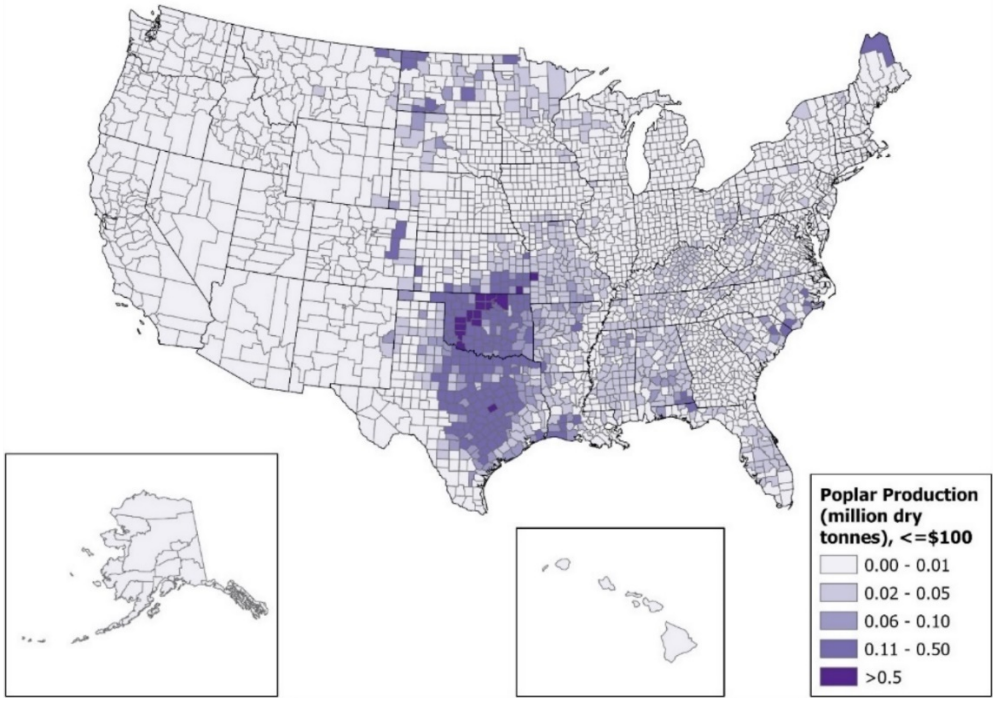

Figure A6-3. Map of maximum potential production from poplar trees at $100 per dry tonne.

Biomass Feedstock Eligibility Criteria

Based on set criteria detailed in the main chapter, each biomass feedstock is assigned to a specific biomass carbon removal and storage (BICRS) processing technology. **Table A6-1** lists the eligibility of all considered feedstock and their BICRS technology.

*__Table A6-1__. Biomass feedstocks that are eligible for each BiCRS technology. Poplar, switchgrass, and willow are the additional feedstocks available in the longterm and are denoted by ***.*

Technology/ Feedstock	Combustion	Fermentation	Gasification	Pyrolysis	Sawmill
Barley straw	✓	✓	✓	✓	–
Citrus residue	–	✓	–	–	–
Corn stover	✓	✓	✓	✓	–
Cotton gin trash	✓	✓	✓	✓	–
Cotton residue	✓	✓	✓	✓	–
Noncitrus residues	✓	✓	✓	✓	–
Oats straw	✓	✓	✓	✓	–
Rice hulls	✓	–	–	–	–
Rice straw	✓	–	–	–	–
Sugarcane bagasse	✓	✓	✓	✓	–
Sugarcane trash	✓	–	–	–	–
Tree nut residues	✓	–	✓	✓	–
Mixedwood logging residues	✓	–	✓	✓	–
Other forest residue	✓	–	✓	✓	–
Western forest restoration	✓	–	✓	✓	✓
Construction and demolition waste	✓	–	✓	✓	–
Municipal solid waste wood	✓	–	–	–	–
Other municipal solid waste	✓	–	–	–	–
Paper and paperboard	✓	–	✓	✓	–
Wheat straw	✓	✓	✓	✓	–
Hardwood, lowland logging residues	✓	✓	✓	✓	–

Hardwood, lowland small diameter trees	✓	✓	✓	✓	✓
Hardwood, upland logging residues	✓	✓	✓	✓	–
Hardwood, upland small diameter trees	✓	✓	✓	✓	✓
Mixedwood small diameter trees	✓	–	✓	✓	✓
Other forest residues	✓	–	✓	✓	–
Other forest thinnings	✓	–	✓	✓	–
Secondary mill residue	✓	–	✓	✓	–
Softwood, natural logging residues	✓	–	✓	✓	–
Softwood, natural small diameter trees	✓	–	✓	✓	✓
Softwood, planted logging residues	✓	–	✓	✓	–
Softwood, planted small diameter trees	✓	–	✓	✓	✓
Primary mill residue	✓	–	✓	✓	–
Sorghum stubble	✓	✓	✓	✓	–
Poplar***	✓	✓	✓	✓	–
Switchgrass***	✓	✓	✓	✓	–
Willow***	✓	✓	✓	✓	–

Technology/ Feedstock	AD	Hydrothermal liquefaction
Beef manure	✓	✓
Dairy manure	✓	✓
Swine manure	✓	✓
Non-residential food waste	✓	✓

Detailed BICRS Technologies Process Description and Modeling Assumptions

BICRS Technologies

Gasification

Gasification of biomass consists of four main steps: Biomass preprocessing, gasification, gas clean-up and reforming, and downstream processing (see main chapter Figure 6-22). Biomass preprocessing includes drying and size reduction of biomass. Biomass is often dried to less than 5% moisture content to reduce the heat load of the gasifier. Biomass is also grinded to around 3 mm diameter to improve the surface area of biomass for higher reaction rates and homogenous heating. Biomass gasification produces mainly syngas which is a gas mixture (50–80%) comprising mostly carbon monoxide, hydrogen, carbon dioxide, and a small amount of methane, char (5–20%), and the remaining which consists of ashes, tar, particulates matter, alkali, nitrogen, and sulfur compounds. The composition of products differs according to biomass types and reaction conditions. Before any downstream processing, syngas is cleaned from tar and other contaminants, which is necessary to avoid damage to equipment and catalyst poisoning. Removing sulfur contaminants is a necessary step in most gasification applications to ensure fuels produced are in compliance with environmental regulations. Acid-gas removal is a typical approach to ensure syngas is sulfur-free. There are also other processes using physical and chemical solvents **[11]**. In this step, CO_2 is also separated from syngas, in addition to sulfur-gases. The separated CO_2 is of high purity and can be captured and sequestered at low cost. Syngas is then reformed for secondary tar removal and to increase hydrogen volume in the syngas **[12]**. Often, syngas produced from biomass is hydrogen-deficit; therefore, a water-gas shift reaction is necessary to readjust the carbon monoxide and hydrogen ratio in the syngas for an optimal downstream process **[13]**. Downstream processes vary according to product type.

Gasification to Liquid Fuels via Fischer-Tropsch Synthesis

Syngas can be converted to liquid alkane fuels such as gasoline, diesel, and jet fuel via Fischer-tropsch synthesis (FTS) after gasification. FTS is a catalytic chemical reaction that converts carbon monoxide and hydrogen in syngas to various ranges of hydrocarbons that later, can be hydrocracked into liquid fuels. Common FTS catalysts are iron-, cobalt-, nickel-, and ruthenium-based. Iron catalyst is a common option due to its lower cost and availability [13]. FTS can also be tuned by adjusting reaction conditions to optimize for the desired product. FTS creates gaseous hydrocarbons, light oxygenates, naphtha, kerosene, and distillates (products are listed from light to heavier carbon molecules) [14]. Kerosene fraction can be upgraded to jet fuels, while distillates can be upgraded to middle-range hydrocarbons such as gasoline and diesel. These products are upgraded to liquid fuels via hydro-processing which includes both hydrocracking and hydrotreating. Hydrocracking is a catalytic process that cracks heavy hydrocarbons into lighter hydrocarbons such as naphtha (gasoline blendstock), kerosene and diesel, while hydrotreating removes sulfur and impurities in fuels to increase the efficiency of fuels and decreases harmful combustion byproducts such as NO_X and SO_X to comply with environmental regulations. Gaseous hydrocarbons and light oxygenates are typically combusted to produce process heat and electricity to be sold to the grid which increases the revenue of the process.

Gasification to Hydrogen via Water–Gas Shift

Syngas can also be converted into hydrogen via a water-gas shift (WGS) reaction. A WGS reaction increases the hydrogen content in the gas streams. The next step is a separation process which separates hydrogen from unreacted syngas (a mixture of carbon monoxide, methane, and other hydrocarbons). The

unreacted syngas is combusted to produce electricity which can be sold to the grid to increase revenue of this pathway. Hydrogen is separated from the other gases via pressure swing adsorption (PSA), a well-developed gas separation technology. PSA maximizes hydrogen recovery, typically a 99.99% purity rate [15]. Finally, hydrogen is compressed to pipeline standards and can be transported using current infrastructure.

Gasification to RNG via Methanation

Syngas can also be converted to renewable natural gas via methanation which occurs after WGS. Methanation is a process that converts carbon monoxide and carbon dioxide to methane using the already existing hydrogen in the syngas. Methanation is a highly exothermic reaction. The heat from the process can be recovered in the form of steam and can be used to generate electricity via a steam turbine. Since methanation is highly exothermic in nature, methanation often occurs in a series of several reactors to have better thermal control in the reaction. Additionally, having methanation occur in series would maximize conversion as well [16]. This process is yet to be commercialized but is being studied by many. GTI investigates that a woody-biomass gasification to a RNG plant has a high capital investment due to the number of reactors required in the process on top of the gasifier [17]. After methanation, a PSA approach is used to separate and purify methane from unreacted gases. Unreacted gas is directed back to the methanation reactor to maximize yields. Separated methane is then compressed to pipeline injection standards. Methane from gasification is of the same chemical structure as natural gas and can be used in current infrastructure without any major modifications.

Fast Pyrolysis

Fast pyrolysis of biomass consists of three main steps: biomass preprocessing, fast pyrolysis, and upgrading of bio-oil (see main chapter Figure 6-23). Similar to gasification, biomass is dried (<10 wt.% moisture content) and grinded (~3 mm diameter) before fast pyrolysis to maximize quality and quantity of product. Fast pyrolysis decomposes biomass into three types of products : bio-oil (60–75%), solid char (10–15%) and non-condensable gases (10–25%) [18]. After fast pyrolysis, these products are separated. Char is often burnt to provide process heat, which also reduces the need for external heat source and subsequently operational costs. However, char can also be sold and used as a form of soil amendment which potentially sequesters 80% of its carbon over 100 years. We assumed that char has a carbon content of 51%. The non-condensable gases are either also combusted for process heat or directed to a steam reformer to produce hydrogen required for upgrading of bio-oil to liquid fuels. Hydrogen is typically produced from reforming natural gas over steam. The latter will reduce the amount of natural gas required which reduces cost and fossil emissions associated with this process. We assume that 90% of the CO_2 produced from combusting char and non-condensable gases can be captured and sequestered. Additionally, we also assumed to capture 90% of the CO_2 from burning natural gas for hydrogen. These assumptions will allow us to investigate the maximum CO_2 removal potential from this technology. Bio-oil is a complex mixture of oxygenated compounds, water, and organic compounds. Bio-oil is highly unstable due to the reactive oxygenates and can continue to chemically react over time which poses a challenge during storage and transportation [19]. To remove all the undesirable characteristics of bio-oil, it is often upgraded which stabilizes and converts it into different fuel products.

Fast Pyrolysis to Liquid Fuels via Hydroprocessing

Bio-oil is upgraded to liquid fuels such as gasoline and diesel via hydroprocessing, which is a process that includes both hydrotreating and hydrocracking. Hydrotreating bio-oil removes oxygen from bio-oil by

reacting it with hydrogen and converts the stream into a gas and liquid fraction. The gas streams contain non-condensable gases, CO_2 and light hydrocarbons, while the liquid streams contain stable hydrocarbon oil and an aqueous stream that is easily separatable. Part of the gaseous stream is combusted onsite for process heat, while the other part is sent to the steam reformer to produce hydrogen for hydrotreating; 90% of the CO_2 from both processes is assumed to be capture and sequestered. The aqueous stream consists of almost little to no carbon and is typically a waste stream. The hydrocarbon oil stream is fractionated into gasoline, diesel blendstocks, and heavy fractions. The heavy fractions are then hydrocracked to form gasoline and diesel blendstocks.

Fast Pyrolysis to Hydrogen via Steam Reforming of Bio-oil

Bio-oil is also an intermediate for the generation of hydrogen. Bio-oil can be converted to hydrogen via catalytic steam reforming of bio-oil. Steam reforming of bio-oil produces a gaseous stream, similar to syngas produced from gasification. The gaseous stream is mainly carbon monoxide and hydrogen (H_2). Following a similar approach to the production of H_2 from syngas produced from gasification, syngas undergoes WGS and then PSA to separate the hydrogen from the unreacted gases. The unreacted gases are directed back to the steam reformer to maximize yields. This process is based on a previous study by Zhang et al. [20]. A major complexity with this conversion pathway is coke deposition during the bio-oil reforming process. This reduces the H_2 yield and can poison the catalyst, which will incur more cost. To overcome this issue, a suitable catalyst optimized for this reaction is necessary. Studies have investigated different catalysts that are applicable to this process. Some of the processes include noble metal-based catalysts such as ruthenium, platinum, palladium and rhodium, which have high catalytic activity and hydrogen selectivity and low coke formation but are more expensive as opposed to transition metal-based catalysts such as nickel **[21]**. Nickel-based catalysts are lower in cost and have been studied to be stable (resist coking) during the steam reforming reaction along with having high hydrogen yields. Therefore, nickel-based catalysts are highly investigated and typically used in this reaction.

Fast Pyrolysis Bio-oil to Bioasphalt

Bio-oil can also be converted into non-fuel, long-lived products such as bioasphalt; a renewable and sustainable version of its fossil-counterpart. Asphalt is often used as a binder for constructing road pavements. Almost 90% of paved roads and highways in the country use asphalt as a main material [22]. Bio-oil produced from fast pyrolysis can replace asphalt completely or blended from a 10–75% blend rate with petroleum asphalt. A 10% blend rate represents a mature technology, while 25–75% blend rates are increasingly being adopted [23], [24]. Bio-oil is investigated as a replacement for asphalt because of its composition. Bio-oil is composed of saturated fraction, aromatic fraction, asphaltene and colloid, all of which are similar in composition to asphalt. Due to the increasing demand for crude oil, the price of asphalt has increased significantly. An advantage of bioasphalt from pyrolysis oil is the ability to lower the overall cost of binders. Another advantage of bioasphalt is the ability to store carbon for a long period of time. In this analysis, bioasphalt is assumed to be able to store 77% of carbon for 100 years. This assumption includes the overall life cycle of bioasphalt, which includes demolishing, a 95% recycling rate, and reconstruction every 20 years **[25]**. The fast pyrolysis to bioasphalt process is modified based on a study by Ganguly et al. **[26]**. In this process, biochar is also produced, along with non-condensable gases (similar to other pyrolysis processes). Biochar is assumed to be sold and utilized as soil amendment, with the ability to store and sequester 80% of the carbon for 100 years. Part of the non-condensable gas stream is used to substitute a portion of natural gas used in the process for heat, while the remaining (about 10%) is investigated to be vented or captured. The CO_2 from the non-condensable gas stream is

minimal and could potentially increase net carbon removal cost, although it maximizes the negative emission potential of this pathway.

Hydrothermal Liquefaction

Hydrothermal liquefaction (HTL) has three main steps: feedstock preparation, hydrothermal liquefaction, and bio-oil upgrading to liquid fuels (see main chapter Figure 6-25). Feedstock is firstly dewatered to the level required for HTL (25% solids). Dewatering of biomass is a form of pretreatment to increase the calorific value of the feedstock and allow for easier transportation to the HTL plant **[27], [28]**. Dewatering of biomass for HTL is essential to minimize capital and operating costs. HTL produces products in various phases – solid, liquid (oil and aqueous), and gas. The solid product consists of char and ash, and 60–70% water is considered as waste stream, as the carbon in the solid product is negligible and can be expensive to capture. The gas stream from HTL is sent to a furnace, to substitute a portion (~20% of heat) of natural gas required to produce heat to drive the HTL reaction. The aqueous phase is sent to an anaerobic digester to produce biogas which is then sent to a steam methane reformer, together with natural gas, to produce hydrogen required to upgrade bio-oil from HTL to liquid fuels. Anaerobic digestion also produces a stream of wastewater with very small amount of carbon; thus, not captured in this analysis as well. The CO_2 from on-site combustion of natural gas is assumed to be captured and sequestered in this analysis to maximize HTL's negative emission potential. All recycled streams used to produce heat and hydrogen also generate gaseous CO_2 after the reaction, which is assumed to be captured and sequestered. The scale of the HTL plant is based on a series of iterations, and a scale of 110 dry tons of biomass per day is chosen as it represents the minimal scale required for the process to be economically feasible **[27]**. Bio-oil is then transferred to a centralized upgrading facility. The upgrading facility is assumed to be able to process 10 times more than the HTL facility. The scale of the upgrading facility is also based on supply chain optimizations. Biocrude is upgraded to liquid fuels such as gasoline and diesel via hydrotreating and hydrocracking. Hydrotreating converts the biocrude to a hydrocarbon product that is in the boiling range of gasoline and diesel. Heavier fractions are hydrocracked producing additional naphtha and diesel products. These products are then fractionated and used as blendstocks.

Combustion

The biomass handling and energy generation operations for combustion are designed and modeled using published reports by the National Renewable Energy Laboratory (NREL) as guidance **[29], [30]**. See main chapter Figure 6-24 for a simplified block diagram of biomass combustion to electricity. Boiler efficiency, defined as the percentage of the lower heating value that is converted to steam heat, is ~80% **[29]**. All other technical parameters can be found in NREL's reports **[29], [30]**. Capital costs are determined from published NREL reports **[30], [31]**. Variable operating costs are estimated from the International Renewable Energy Agency 2020 **[32]**. A CO_2 concentration of 15.5 mol% is used to model CO_2 capture operations. Carbon removal via the combustion pathway is achieved from captured CO_2 and the carbon capture efficiency is 90%. All of the energy demanded by the CO_2 capture operations is provided by the combustion facility.

Fermentation

The fermentation of lignocellulose involves three main steps: pretreatment, fermentation, and downstream processing (See main chapter Figure 6-26). Pretreatment involves the breakdown of the biomass into its main components. Biomass pretreatment technologies include autohydrolysis, acid hydrolysis, alkaline hydrolysis, steam explosion, and others. In the present study, deacetylation +

mechanical refining was selected as the pretreatment technology due to its low cost, high efficiency, and low risk [30]; the technology borrows many operations from the kraft pulping industry. In addition, this form of pretreatment is currently the state-of-the-art pretreatment technology under development at NREL. The deacetylation step uses NaOH to solubilize lignin, which is then sent for downstream upgrading into adipic acid or electricity generation. Lignin is a complex, heterogenous, branched polymer made up of aromatic compounds of high energy density with the potential for value-added chemical synthesis, although poor selectivity has hindered the development of value-added chemicals from lignin. The traditional application of lignin is combustion for heat and power production, as established by the biomass pulping industry [33]. High-value applications of lignin have traditionally been the production of vanillin and lignosulfonates [34].

NREL has recently developed a state-of-the-art method of producing adipic acid from lignin in a cost-effective manner [31], [35], [36]. Adipic acid is a major industrial chemical used as a precursor for many products, including nylon. In this study, we modeled two general fermentation platform technologies with and without adipic acid synthesis. In the fermentation platform without adipic acid synthesis, all lignin is sent for heat and power production using standard technology. In the fermentation platform with adipic acid synthesis, part of the lignin is sent to a series of operations developed by NREL for high efficiency adipic acid production. More specifically, the combined stream from pretreatment and enzymatic hydrolysis is routed to a "base catalyzed deconstruction" (BCD) reactor operating at elevated temperatures to further deconstruct the lignin into solubilized phenolic oligomers. The liquid BCD product is then routed to bioconversion, where genetically engineered microbes convert the soluble lignin and other residual organics to muconic acid through an aerobic pH-controlled bioconversion. Muconic acid is then isolated in high-purity crystals following acid addition and low-pH crystallization. The muconic crystals are redissolved in a carrier solvent then hydrogenated under mild conditions to adipic acid, which is subsequently recovered through another crystallizer [30]. The solid cellulosic (non-lignin) fraction from pretreatment is sent to enzymatic hydrolysis where a cocktail of cellulase enzymes hydrolyze the cellulose and hemicellulose into monomeric 5- and 6-carbon sugars. A continuous enzyme hydrolysis system capable of converting 96% of polysaccharides into monomeric sugars is modeled [30], [37]. The monomeric sugars are converted to various biochemicals and biofuels using genetically engineered microbes; the diesel pathway uses a different microbe than the ethanol, jet fuel, and polyethylene pathways.

Fermentation to Renewable Diesel

The renewable diesel pathway has been developed by NREL and involves fermentation of the 5-carbon and 6-carbon sugars into butryic acid using an engineered microbe capable of producing 0.43 kg butryic acid per kg sugar [30]. Carbon removal via the diesel pathway is achieved from captured CO_2 during fermentation and lignin combustion. The butyric acid is separated from the fermentation broth by dissolution in a solvent and membrane extraction, followed by distillation to separate the butyric acid from the solvent, as shown in Figure A6-4. The butryic acid is converted to hydrocarbon fuel via a series of upgrading catalytic operations including ketonization, condensation, and hydrotreatment [30]. Capital and operating costs are calculated using a mass and energy model derived from NREL's publications [30]. The CO_2 generated during fermentation is of high enough purity to be ready for sale after drying and compression. The gate-to-gate carbon removal efficiency of the fermentation to diesel with adipic acid BiCRS pathway varies from 0.598 to 0.840 tonnes CO_2/tonnes biomass, or 33 – 46% of the theoretical removal efficiency, as shown in Table A6-2. The gate-to-gate carbon removal efficiency of the

fermentation to diesel without adipic acid BiCRS pathway varies from 0.952 to 1.041 tonnes CO_2/tonnes biomass, or 53 – 58% of the theoretical removal efficiency, as shown in Table A6-3. The lower removal efficiency for the pathway with adipic acid production is due to the degradation of adipic acid into CO_2 at end-of-life.

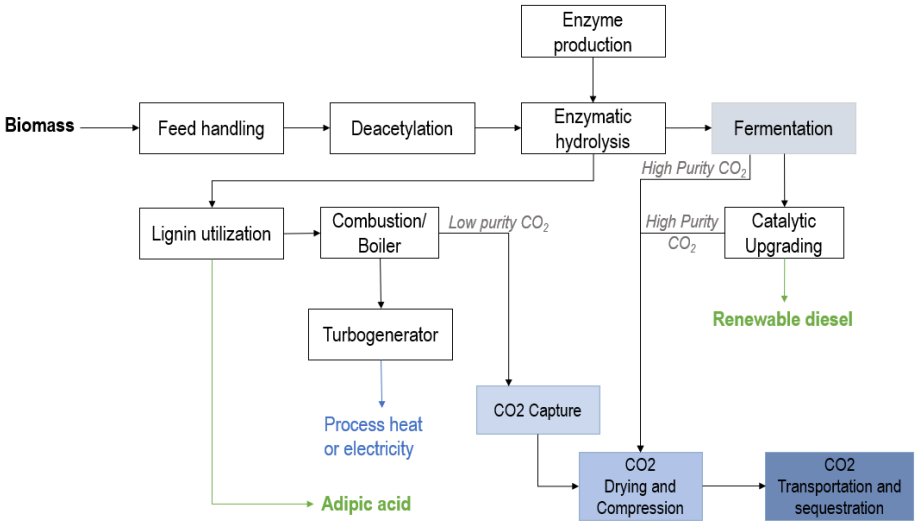

Figure A6-4: Simplified block diagram of fermentation to renewable diesel and adipic acid with carbon capture and storage.

Table A6-2. *Gate-to-gate carbon removal efficiencies for the fermentation to diesel BiCRS pathway with variation in co-products*

Co-products	Near-term (2025)		Long-term (2050)	
	Removal Efficiency (tonnes CO_2/tonnes biomass)	% theoretical	Removal Efficiency (tonnes CO_2/tonnes biomass)	% theoretical
Diesel	0.952	53%	1.041	58%
Diesel + adipic acid	0.598	33%	0.840	46%

Fermentation to Ethanol

The ethanol pathway has been developed by NREL and involves fermentation of 5-and 6-carbon sugars into ethanol using an engineered microbe [38]. Carbon removal via the ethanol pathway is achieved from captured CO_2 during fermentation and lignin combustion. The 5-carbon and 6-carbon conversion yields to ethanol are 91% and 96%, respectively. After fermentation, ethanol is recovered from the fermentation broth by distillation and dehydrated via molecular sieve adsorption to reach a product purity of more than 99.5%, as shown in Figure A6-5 [38]. The energy demand for ethanol recovery is 4MJ/kg ethanol [39]. Capital and operating costs are calculated using a mass and energy model derived from NREL's publications [30], [38]. The CO_2 generated during fermentation is of high enough purity to be ready for sale after drying and compression. The gate-to-gate carbon removal efficiency of the fermentation to ethanol with adipic acid BiCRS pathway varies from 0.462 to 0.814 tonnes CO_2/tonnes biomass, or 26–45% of the theoretical removal efficiency. The gate-to-gate carbon removal efficiency of the fermentation to ethanol without adipic acid BiCRS pathway varies from 0.816 to 1.015 tonnes CO_2/tonnes biomass, or

45–56% of the theoretical removal efficiency (**Table A6-3**). The lower removal efficiency for the pathway with adipic acid production is due to the degradation of adipic acid into CO_2 at end-of-life.

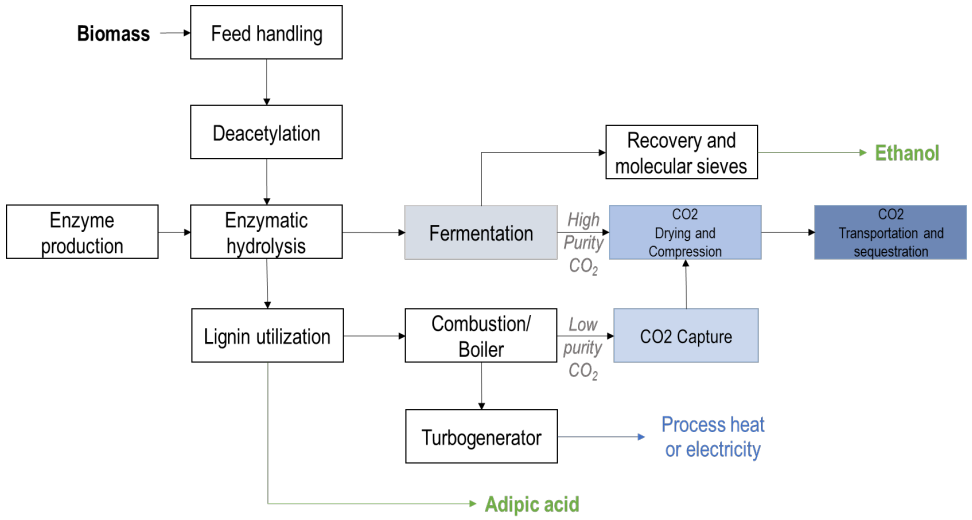

Figure A6-5: Simplified block from diagram of fermentation to ethanol and adipic acid with carbon capture and storage.

Table A6-3. Gate-to-gate carbon removal efficiencies for the fermentation to ethanol BiCRS pathway with variation in co-products.

Co-products	Near-term (2025)		Long-term (2050)	
	Removal Efficiency (tonnes CO_2/tonnes biomass)	% theoretical	Removal Efficiency (tonnes CO_2/tonnes biomass)	% theoretical
Ethanol	0.816	45%	1.015	56%
Ethanol + adipic acid	0.462	26%	0.814	45%

Fermentation to Jet Fuel

The jet fuel pathway builds upon the ethanol pathway with the inclusion of catalytic upgrading to convert the alcohol to jet fuel, as shown in **Figure A6-6**. Carbon removal via the jet fuel pathway is achieved from captured CO_2 during fermentation and lignin combustion. Ethanol is first catalytically dehydrated to ethylene (99% conversion) using an advanced HZM-5 catalyst, which is tolerant of small amounts of moisture and eliminates the need to have a molecular sieve adsorption unit **[40], [41]**. Approximately 0.6 kg of ethylene is produced per kg of ethanol, corresponding to a ~99% stoichiometric conversion efficiency **[38]**. The ethylene is oligomerized into linear α-olefins and then hydrotreated to eliminate double bonds and fully saturate the molecules into diesel, gasoline, and jet fuel range hydrocarbons **[42], [43]**. The mixture of hydrocarbons is readily separated via distillation. The CO_2 generated during fermentation is of high enough purity to be ready for sale after drying and compression. The gate-to-gate carbon removal efficiency of the fermentation to jet fuel with adipic acid BiCRS pathway varies from 0.324 to 0.814 tonnes CO_2/tonnes biomass, or 18–45% of the theoretical removal efficiency, as shown in **Table A6-4**. The gate-to-gate carbon removal efficiency of the fermentation to jet fuel without adipic acid BiCRS pathway varies from 0.678 to 1.015 tonnes CO_2/tonnes biomass, or 38–56% of the theoretical removal

efficiency, also shown in Table A6-5. The lower removal efficiency for the pathway with adipic acid production is due to the degradation of adipic acid into CO_2 at end-of-life.

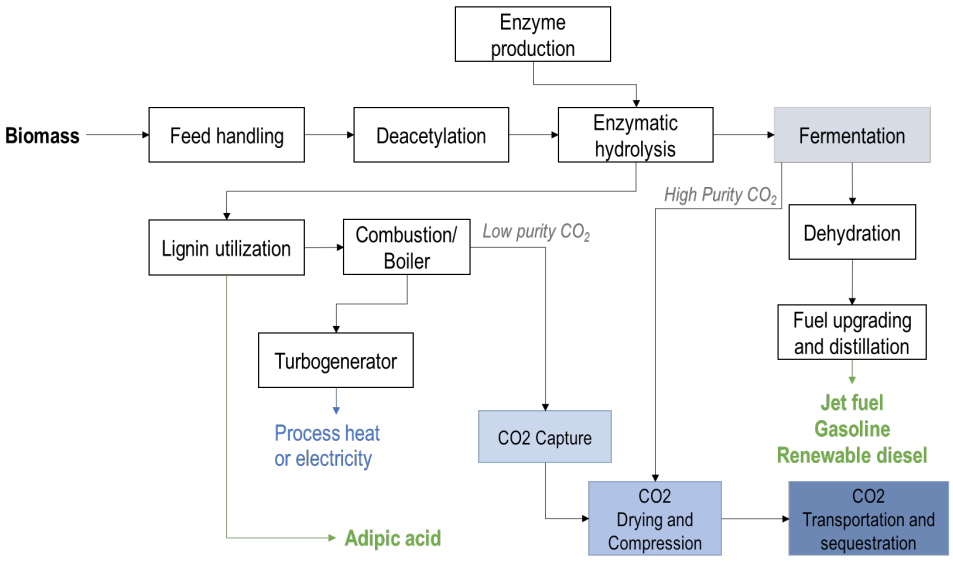

Figure A6-6. Simplified block from diagram of fermentation to jet fuel and adipic acid with carbon capture and storage.

Table A6-4. Gate-to-gate carbon removal efficiencies for the fermentation to jet fuel BiCRS pathway with variation in co-products.

Co-products	Near-term (2025)		Long-term (2050)	
	Removal Efficiency (tonnes CO_2/tonnes biomass)	% theoretical	Removal Efficiency (tonnes CO_2/tonnes biomass)	% theoretical
Jet fuel	0.678	38%	1.015	56%
Jet fuel + adipic acid	0.324	18%	0.814	45%

Fermentation to Polyethylene

The polyethylene pathway builds upon the ethanol and jet fuel pathways with the inclusion of catalytic upgrading to convert the ethylene into polyethylene, as shown in **Figure A6-7**. Carbon removal via the polyethylene pathway is achieved from both captured CO_2 and long-lived carbon in the polyethylene material. Established petrochemical refining technologies can be used to polymerize ethylene with very high efficiency, thereby reducing risk **[38], [44]–[46]**. Technical parameters and economic data for polyethylene synthesis are primarily based on reports by NREL and related materials **[38], [44]–[48]**. Energy consumption to convert ethanol into polyethylene is 9.85 MJ/kg of polyethylene **[44]**. The process model for polyethylene includes end-of-life handling, where it is assumed 16% and 9% of the polyethylene is incinerated and recycled, respectively **[49]**. The emissions associated with polyethylene recycling are assumed to be 1.175 kg of CO_2 per kg of polyethylene recycled **[45]**. The remaining 75% of the polyethylene at end-of-life is assumed to be landfilled where 60% of the carbon is stored for 100 years **[50]**. The CO_2 generated during fermentation is of high enough purity to be ready for sale after drying and compression. The gate-to-gate carbon removal efficiency of the fermentation to polyethylene with adipic acid BiCRS pathway varies from 0.594 to 1.132 tonnes CO_2/tonnes biomass, or 33–63% of the theoretical

removal efficiency, as shown in Table A6-5. The gate-to-gate carbon removal efficiency of the fermentation to polyethylene without adipic acid BiCRS pathway varies from 0.948 to 1.333 tonnes CO_2/tonnes biomass, or 52–74% of the theoretical removal efficiency, as shown in Table A6-6. The lower removal efficiency for the pathway with adipic acid production is due to the degradation of adipic acid into CO_2 at end-of-life.

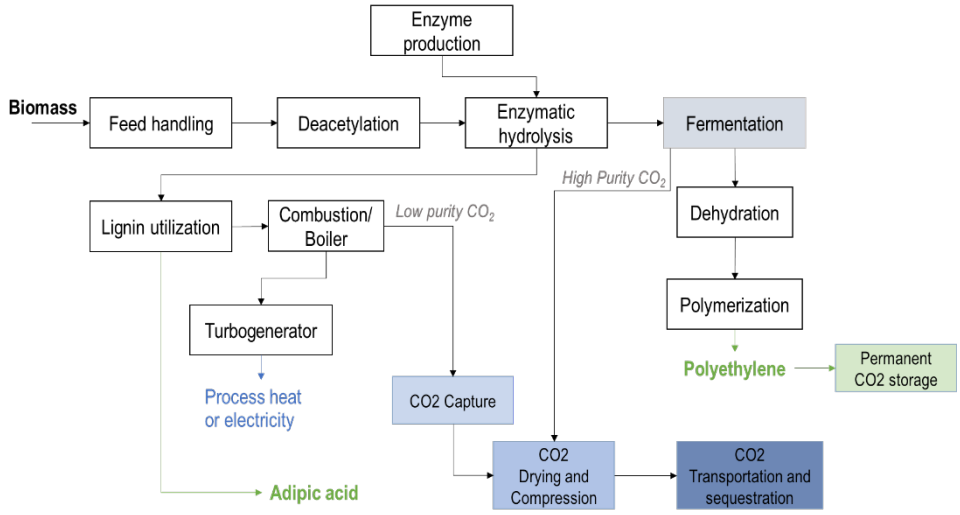

Figure A6-7: *Simplified block from diagram of fermentation to polyethylene and adipic acid with carbon capture and storage.*

Table A6-5. Gate-to-gate carbon removal efficiencies for the fermentation to polyethylene BiCRS pathway with variation in co-products.

	Near-term (2025)		Long-term (2050)	
Co-products	**Removal Efficiency (tonnes CO2/tonnes biomass)**	**% theoretical**	**Removal Efficiency (tonnes CO_2/tonnes biomass)**	**% theoretical**
Polyethylene	0.948	52%	1.333	74%
Polyethylene + adipic acid	0.594	33%	1.132	63%

Anaerobic Digestion

Summaries for carbon removal efficiencies of wet waste conversion to renewable natural gas via anaerobic digestion of manure, food waste, and biogas capture are shown in Table A6-6 and A6-7.

Table A6-6. *Gate-to-gate carbon removal efficiencies for the anaerobic digestion BiCRS pathway with variation in feedstock*

	Near-term (2025)		Long-term (2050)	
Feedstock	**Removal Efficiency (tonnes CO_2/tonnes biomass)**	**% theoretical**	**Removal Efficiency (tonnes CO_2/tonnes biomass)**	**% theoretical**
Swine manure	0.186	8%	0.244	11%
Food waste	0.301	16%	0.395	22%
Dairy/beef manure	0.030	1%	0.039	2%

Table A6-7. Gate-to-gate carbon removal efficiencies for the existing biogas source BiCRS pathway with variation in feedstock

	Near-term (2025)		Long-term (2050)	
Feedstock	**Removal Efficiency (tonnes CO_2/tonnes biomass)**	**% theoretical**	**Removal Efficiency (tonnes CO_2/tonnes biomass)**	**% theoretical**
Landfill biogas	1.089	67%	1.214	74%
Wastewater treatment plant biogas	0.191	10%	0.315	16%

Boundary Conditions, Techno-Economic and Life Cycle Assessment Assumptions, BILT Model Description

Techno-economic Assessment Assumptions and Equations

The cost of CO_2 removal for each BICRS technology is calculated using these specific economic parameters, shown in Table A6-8 using Equations 1–7. We assume that capital cost (CAPEX) has a capital recovery factor (CRF) of 11.75% corresponding to a 10% interest rate and 20-year payback period, which represent realistic terms for greenfield biorefineries. Indirect capital cost is calculated as a percentage of direct capital cost to be consistent across pathways as per NREL's methodology [29]. A 0.7 capital scaling factor is deemed acceptable given that each of the BiCRS technologies investigated in this project is capable of achieving economies of scale. Operating cost (OPEX) is categorized into fixed and variable OPEX. Fixed OPEX is calculated as a percentage (4.5%) of total capital cost to be consistent across pathways, while variable OPEX is technology and feedstock dependent [29]. Bioproduct revenue is calculated based on the amount of fuel, chemical and/or long-lived product produced in each scenario and the 5-year average wholesale price of the product. The cost year is selected to be 2022 for both near-term and long-term to provide realistic cost estimates; inflation is accounted across the entire economic analysis.

Table A6-8. Economic parameters and assumed values to calculate costs of carbon removal ($/tonne CO_2).

Term	Assumptions
Capital recovery factor	11.75%
Interest rate	10%
Project life, *N*	20 years
Indirect capital cost	0.424 x direct capital cost
Capital scaling factor	0.7
Fixed operating cost	4.5% of total capital cost
Plant utilization	90%
Cost year	2022

Equation 1 $$\textbf{Carbon Removal Cost } (\$/\textbf{tonne CO2}) = \frac{\textbf{Levelized Cost of BiCRS} - \textbf{Revenue from Bioproduct}}{\textbf{Net Carbon Removal}}$$

Equation 2 $$Levelized\ Cost\ (\$/year) = CAPEX + OPEX$$

Equation 3 $$Annual\ OPEX\ (\$/year) = Fixed\ OPEX + Variable\ OPEX$$

Equation 4 $$Annual\ CAPEX\ (\$/year) = Total\ CAPEX \times \frac{capital\ recovery\ factor}{plant\ utilization}$$

Equation 5 $$Capital\ Recovery\ Factor\ [\%] = \frac{i(i+1)^N}{(1+i)^N - 1}$$

Equation 6 $$Total\ CAPEX = Direct\ CAPEX + Indirect\ CAPEX$$

Equation 7 $$\begin{aligned} i\ [\%] &= weighted\ average\ cost\ of\ capital \\ &= (interest\ on\ debt\ capital) \times (\%\ debt\ financing) \\ &+ (return\ on\ equity\ capital) \times (\%\ equity\ financing) \end{aligned}$$

Technologies that generate CO_2-containing gaseous waste streams of compositions less than 90 vol% CO_2 include CO_2 capture, drying, and compression in at least one potential pathway. Streams with greater than 90 vol% CO_2 are assumed to not undergo additional separation. High TRL amine scrubbing technology is assumed to capture CO_2 and the cost of CO_2 capture is determined via a multi-variate regression (Equation 8) that accounts for CO_2 flow rate, concentration, and capture rate [51]. Note Equation 8 contains both capital and operating costs to give a levelized capture cost. The capital and operating costs for CO_2 drying and compression is determined using Equations 9 and 10 to give a levelized drying and compression cost [52].

Equation 8. Cost of CO_2 Capture

$$= 10^{2.18388 - 0.42601 \times \log(Capture\ Rate) - 0.3913 \times \log(Co2\ Concentration) - 0.02825 \times \log(Flow\ rate)}$$

Equation Parameters:

Cost of CO_2 capture	USD per tonne CO_2 captured
Capture rate	Percentage of CO_2 captured (0 – 100)
CO_2 concentration	CO_2 concentration mol% (0 – 1)
Flow rate	Flow rate of CO_2 into the absorber (tonne/day)
Intercept	2.18388
Capture rate coefficient	-0.42601
CO_2 concentration coefficient	-0.39131
Flow rate coefficient.	-0.02825

Equation 9 CO_2 Drying and compression CAPEX (million \$) $= 30.38 \times \left(\frac{tonne\ CO_2/day}{4848.94}\right)^{0.77}$

Equation 10 CO_2 Drying and Compression electricity consumption $= 0.073 \frac{kW}{kg\ CO_2/hour}$

Product Emission Factors

Table A6-9 tabulates the emission factors for all products in the analysis. These emission factors are used to compute the CO_2 generated in end use of product. The emission factors are obtained from a combination of sources including the EIA and Argonne National Laboratory Life Cycle Assessment GREET model. Long-lived products such as bioasphalt, biochar, polyethylene, and lumber emit about 20–50% of their carbon over 100 years when utilized, as shown in Table 6-14 in the main chapter. The emissions generated are very small as compared to the other products as most of the carbon in these products are assumed to remain in the product itself and contribute to carbon removal. The emission factors for all products are assumed to not change over time except for electricity. Electricity is assumed to have no emissions in 2050 based on the assumption of a net-zero grid, proposed by the Biden Administration.

Table A6-9. *Emission factors for all products (These emission factors are used to calculate the CO_2 generated in the end use of the product).*

Product	Emission factors (gCO_2/MJ)	
	2025	2050
Gasoline	73.82	73.82
Diesel	75.10	75.10
Ethanol	70.40	70.40
Sustainable aviation fuel	68.46	68.46
Hydrogen	0	0
Renewable natural gas	50.23	50.23
Electricity	0	0
Bioasphalt	0.47gCO_2/g product	0.47gCO_2/g product
Biochar	0.37 gCO_2/g product	0.37 gCO_2/g product
Lumber	0.92 gCO_2/g product	0.92 gCO_2/g product
Polyethylene	1.26 gCO_2/g product	1.26 gCO_2/g product
Adipic acid	1.81 gCO_2/g product	1.81 gCO_2/g product
Acetone	0.02 gCO_2/MT	0.02 gCO_2/MT
MEK-2-Butanone	0.01 gCO_2/MT	0.01 gCO_2/MT
Wax	0	0

Overview of Major Biomass and Infrastructure Categories

Table A6-10. *Overview of major biomass and infrastructure categories (and assumptions therein) in this BiCRS analysis. Transportation infrastructure refers to both biomass and CO_2 transportation, with the exception of pipeline, which is specific to CO_2.*

BiCRS assessment (#, name)	Ref. year for biomass supply and soil carbon	Crop types	Carbon intensity of grid	Transportation infrastructure	BiCRS product market constraints
(0) **Current biomass (2025)**	2025	Wastes and residues	2023	Truck, rail	Current market
(1) **Baseline Biomass (2050)**	2050	Wastes and residues	Zero emission	Truck, rail, trunk pipeline	Projected 2050
(2) **Zero Cropland Change**	2050	Baseline+ additional carbon crops with no cropland change	Zero emission	Truck, rail, trunk pipeline	Projected 2050
(3) **Maximum Economic Potential**	2050	Baseline+ additional carbon crops (economic potential)	Zero emission	Truck, rail, trunk pipeline	Projected 2050

Wet Waste Life Cycle Assessment Boundaries

The life cycle assessment (LCA) boundary begins with biomass waste entering the biomass conversion facility, either a landfill, wastewater treatment plant, or agricultural anaerobic digester, for pathways with existing biogenic emissions. The biomass carbon that is retained in the landfill is assumed to be non-biodegradable and therefore contributes to removal. The biomass carbon that exits the wastewater treatment plants and agricultural digesters as digestate is assumed to be fully biodegradable within 100 years. Existing biogenic emissions from landfills, wastewater treatment plants, and agricultural digesters are only considered if the biogas flow rates exceed 10 kt biogas/year. Landfill biogas flow is estimated to decrease 2% per year, and wastewater treatment plant and agricultural anaerobic digester biogas flows are estimated to increase in proportion with population growth starting in 2025 and ending in 2050 **[53], [54]**. Similarly for hydrothermal liquefaction, biomass throughput is to exceed 100 tons per day as this scale is deemed to be the minimum capacity required for HTL plants to be commercially viable **[27]**.

Additional Market Demand Assumptions and Product Prices Assumptions

The market for bio-commodities is more uncertain than the market for energy products. For this analysis, we gathered commodity market size and prices from various sources, and we supplemented missing information with market growth rate and price inflation assumptions. The market for bio-oil is based on the asphalt binder industry [55]. We assumed that bio-oil can be mixed at a 1:10 ratio with fossil-asphalt, and the asphalt has a lifetime of 20 years after which time 5% could be lost during recycling. Bio-polyethylene is a feedstock for the plastic and packaging industries. It can replace 100% of fossil-based plastics and be landfilled, incinerated, or recycled after use. For this study, bio-polyethylene demand for 2025 is based on the emerging bioplastic market [56]. The bioplastic market is growing at an annualized growth rate of about 19%, but we assume a conservative growth rate of 3.2% based on the conventional plastic market. The bio-polyethylene price is based on work by NREL [30]. Adipic acid is a high-value by-product of bio-polyethylene production suitable for the polymer industry, as explained in the Biological

BiCRS section [57]. Fermentation-based biorefineries can produce bio-polyethylene and adipic acid, or only bio-polyethylene.

Small dimensional lumber, also referred to as utility grade lumber or #3 common lumber, is a relatively low-value lumber product and the main product from the sawmill pathway modeled in this study [58]. We selected small dimensional lumber as the main product due to the relatively small-sized, small-diameter trees that are used in the sawmill pathway; see section on Feedstock-Technology criteria for more information. An average selling price of \$171 per m^3 is used for the small dimensional lumber **[59]**, which is considerably lower than the average price of \$283 per m^3 for all lumber products **[60]**. We also assumed that the selling price of electricity is 5 cents per kWh which is based on rates typical for electricity generators. This is approximately 56% of total electricity cost (generation, distribution, transmission, and maintenance) **[61], [62]**. Hydrogen predictions are based on the "Road Map to a US Hydrogen Economy" by a consortium of companies **[63]**. Hydrogen is both a fuel and chemical feedstock, and most of its use today is for refining. In 2050, hydrogen is projected to be a key transportation fuel in addition to a refining feedstock. We also consider a low hydrogen price scenario with a price of \$1 per kg, which is a US Department of Energy target. We also consider a scenario for meeting 100% of the aviation fuel demand with sustainable aviation fuel. In this scenario, the underlying assumption is that transportation energy demand has shifted to electricity for consumer vehicles.

Detailed Description of Biocarbon Infrastructure, Logistics, and Transportation

Solution Technique

Biocarbon infrastructure, Logistics, and Transportation (BILT), as used in this analysis for carbon removal, develops the carbon-removal cost curve by solving a series of mixed-integer programming problems. It first determines the maximum amount of carbon that can be removed without regard to cost. If we term this maximum amount of carbon *M*, then stage 2 develops a curve by answering a series of questions of the form, "What is the least cost way of achieving a carbon removal or *p*% of *M*?," for various choices of *p*.

Problem Specification

Stage 1: In stage 1, BILT determines the maximum possible carbon removed without regard to the cost. It is establishing the endpoint of the carbon removal cost curve. Since transporting the biomass causes carbon emissions, the solution to the stage 1 problem typically involves many small facilities located near the biomass sources.

Objective = Maximize the carbon removed, considering the:

- Carbon impacts of soil carbon and land use change
- Carbon uptake of the growing biomass
- Carbon emitted in harvesting the biomass and transporting it to the facilities
- Carbon emitted in converting to fuel products
- CO_2 that can be captured in the conversion process
- Carbon emitted in transporting that CO_2 to a storage facility

Subject to:

- Availability of the biomass at each county at the allowed price levels
- Capacities of the facilities for processing biomass

- Minimum utilization factors for a facility
- Production limits for each product

Stage 2: In stage 2, the constraint set is the same as in stage 1, but it also includes the addition of the objective function from the stage 1 problem (measuring the amount of carbon removed), to become a lower bound on the amount of carbon that must be removed. This stage 2 problem is solved multiple times, varying this lower bound on carbon removed. Typically, the bound is given as *p*% of the optimal objective function value from stage 1, where *p* takes on the values 25, 50, 75, 90, and 99.

Objective = Minimize the total cost, including the:

- Cost of cultivating and harvesting the feedstock
- Cost of transporting the biomass to the facility
- Capital cost of the facility
- Annual operating cost for the facility
- Production cost for converting the biomass
- Cost of transporting the CO_2 to the storage site
- Cost of injecting the CO_2 into the storage basin

Subject to:

- Availability of the biomass at each county at the allowed price levels
- Capacities of the facilities for processing biomass
- Minimum utilization factors for a facility
- Production limits for each product
- A minimum carbon avoidance (or removal) threshold

Solver

The BILT model solves the mixed-integer programming problems using a commercial solver, such as Gurobi or CPLEX. The model stores the detailed results in the database, and then generates Excel workbooks and Google Earth KML files that display the solution summaries.

Additional BILT Results

As shown in **Table A6-11**, the carbon removal potentials for anaerobic digestion (AD) and hydrothermal liquefaction (HTL) of manure and food waste are substantially lower than other BiCRS pathways, which leads to a much higher removal cost. The low carbon removal potential for AD of manure and food waste is due largely to the assumed emissions of CO_2 from digestate decomposition (which is not captured) and RNG combustion. The only carbon that contributes to CO_2 removal in the AD pathway is the CO_2 that is separated from the biogas and compressed and injected for geological sequestration. The low carbon removal potential for HTL of manure and food waste is due largely to the emissions of CO_2 from combustion of liquid fuels. The only carbon that contributes to CO_2 removal in the HTL pathway is the CO_2 that is in the off-gas stream from the HTL process and upgrading of biocrude to liquid fuels. The carbon removal potential for LF and wastewater treatment plant (WWTP) biogas handling is relatively high because of the higher conversion of biomass to biogas and reduced decomposition residues. In landfills, the residual waste biomass that is not converted to biogas is assumed to contribute to carbon removal. In addition, renewable natural gas (RNG) and HTL require construction and operation of new facilities, which

are costly for the small scales of operation employed. The BILT model does not allow for the transport of manure or food waste, and thus new AD and HTL facilities must be constructed onsite to process relatively small quantities of biomass waste. The nonlinear scaling factor makes small-scale AD and HTL biorefineries more costly than the larger biorefineries used in other parts of this study (gasification, combustion, fermentation, etc.). The spatial distributions of BiCRS facilities utilizing wet waste for a 50% removal target is illustrated in Figure A6-8; for a 90% removal target, see main chapter Figure 6-43.

Table A6-11. *Quantities and costs of CO_2 removed for wet waste processing and biogas upgrading for 50% and 90% removal targets*

CO_2 removal target	Anaerobic digestion and hydrothermal liquefaction of manure + food waste		Biogas processes at existing landfills and wastewater treatment plants	
	CO_2 removed	CO_2 removal cost	CO_2 removed	CO_2 removal cost
	tonne CO_2	USD/tonne CO_2	tonne CO_2	USD/tonne CO_2
50%	12,434,596	$770	31,686,056	$40
90%	22,382,272	$1,242	57,034,901	$51

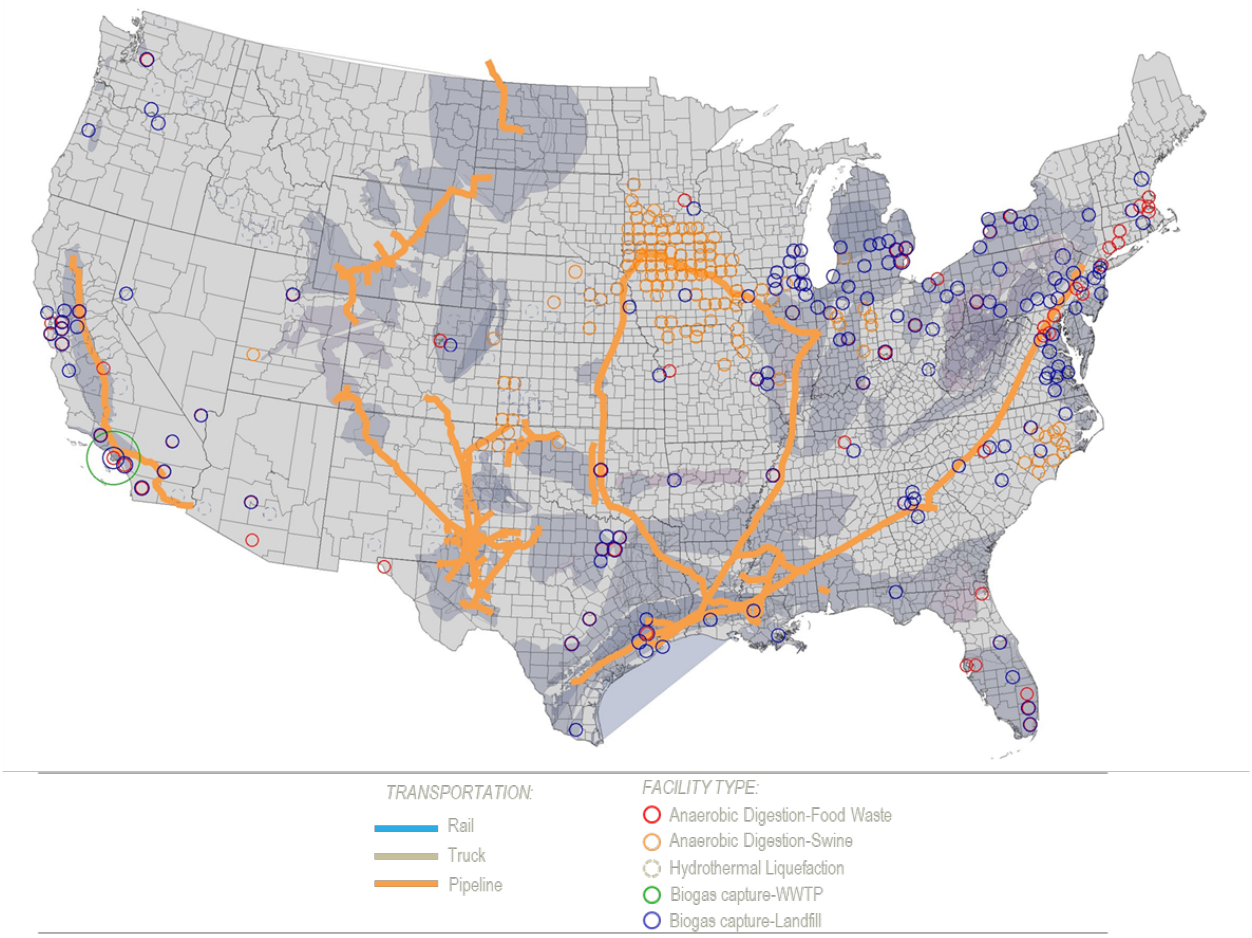

Figure A6-8. BILT result: Wet Waste 50%. *A snapshot of a US BiCRS system that could utilize wet waste to achieve 50% carbon removal capacity (related to total biomass availability) at minimal cost ($/tonne CO_2). The symbol colors represent facility type. The symbol sizes represent facility CO_2 capacity ranging from 1,711 tonnes/year to 7 million tonnes/year. Orange lines represent CO_2 pipelines (current and future). Wet waste biomass is processed locally, and the BiCRS facilities are designed to match the available capacity of the wet waste resources. The total CO_2 removal potential depicted here represents 12 million tonnes/year at an average removal cost of $770/tonne CO_2. (Larger circles represent a larger CO_2 removal capacity)*

Additional results supplementing the results in the main chapter includes the breakdown of total costs by region for the 2050 zero-cropland-change scenario achieving a 90% removal target is depicted in Figure A6-9, and regional bioproduct revenue in Figure A6-10.

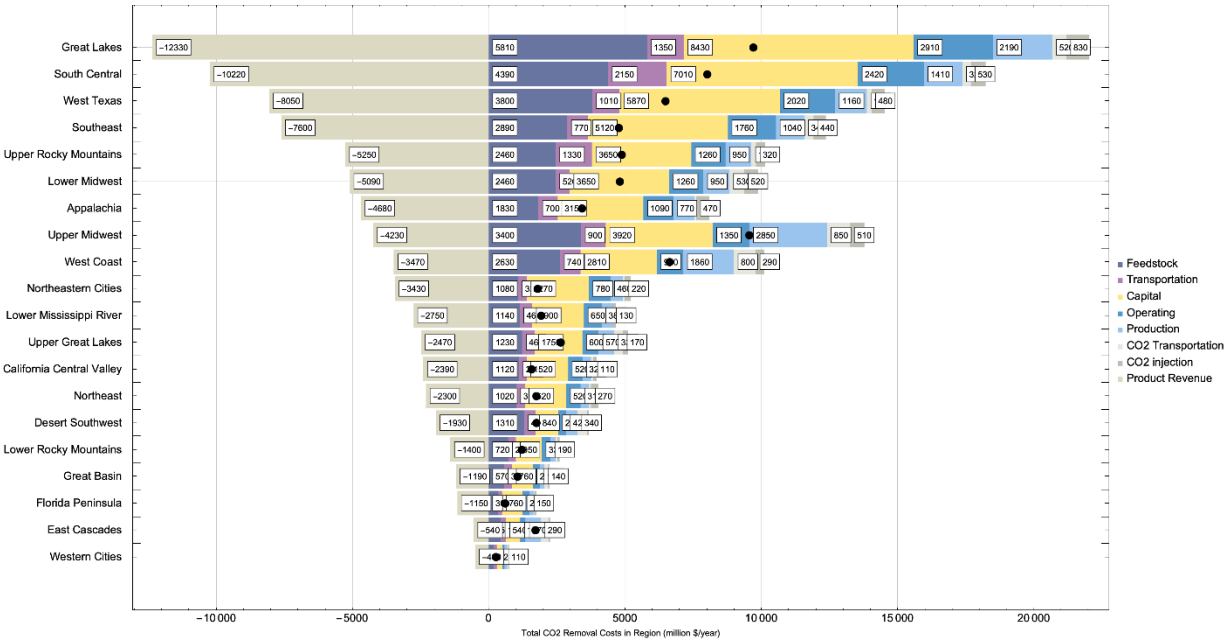

Figure A6-9. *Breakdown of total cost across different regions in US utilizing 2050 zero cropland change biomass that could achieve 90% carbon removal capacity (related to total biomass availability) at minimal cost ($/tonne CO_2).*

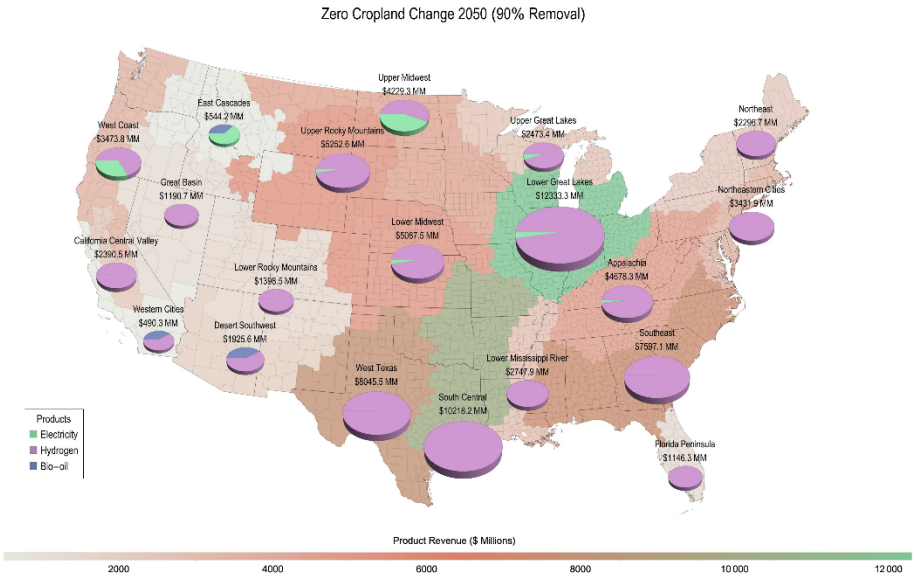

Figure A6-10. Bioproduct Revenue by Region. *Pie size and black font value represent total revenue from selling bio-products. Colors in the pie chart indicate revenues generated from different bio-product: purple for H_2, green for electricity, and darker purple for bio-oil (to make bio-asphalt). Total revenue is estimated by utilizing 2050 zero cropland change biomass that could achieve 90% carbon removal capacity (related to total biomass availability) at minimal cost ($/tonne CO_2).*

In our sensitivity analysis, we explore the impact of varying the CRF (**Figure A6-11**). The CRF is a key factor to depreciate the capital investment into an annualized capital cost. The calculation is represented as:

$$\text{Annual CAPEX (\$/year)} = \text{Total CAPEX} \times (\text{Capital Recovery Factor}) / (\text{Plant Utilization})$$

This approach offers a simplified means of examining how changes in the CRF can influence the capital investment across all pathways under consideration. This variation allows us to assess the economic sensitivity of the different pathways to changes in capital costs.

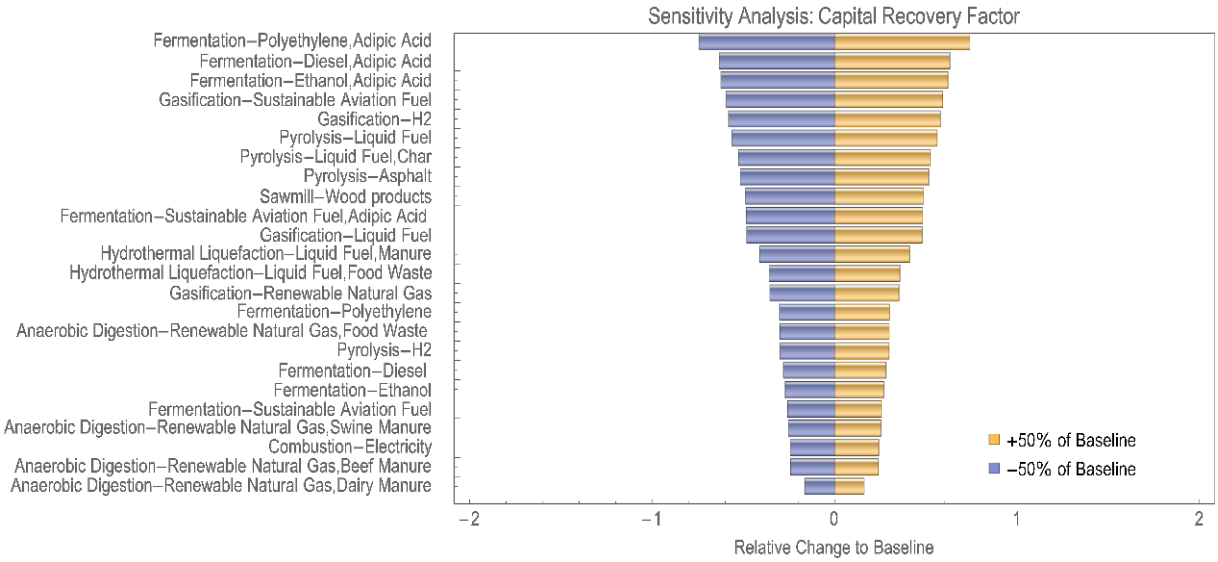

Figure A6-11. *Variation of the CO_2 removal cost relative to the capital recovery factor. The capital recovery factor was varied by both increasing (+50%) and decreasing (-50%) it relative to the baseline capital recovery factor of 11.75%.*

REFERENCES

[1] U.S. Environmental Protection Agency, "Paper and Paperboard: Material-Specific Data." Accessed: Sep. 26, 2023. [Online]. Available: https://www.epa.gov/facts-and-figures-about-materials-waste-and-recycling/paper-and-paperboard-material-specific-data

[2] Environment Research & Education Foundation, "EREF Study Shows Average MSW Tip Fee Decreased in 2020." Accessed: Sep. 26, 2023. [Online]. Available: https://erefdn.org/eref-study-shows-average-msw-tip-fee-decreased-in-2020/

[3] Martin, Ellen, "How to run a profitable MRF in today's market," Resource Recycling News. Accessed: Sep. 26, 2023. [Online]. Available: https://resource-recycling.com/recycling/2018/10/23/how-to-run-a-profitable-mrf-in-todays-market/

[4] USDA Farm Service Agency, "FSA Crop Acreage Data Reported to FSA." 2021. [Online]. Available: https://www.fsa.usda.gov/news-room/efoia/electronic-reading-room/frequently-requested-information/crop-acreage-data/index

[5] B. Basso and J. T. Ritchie, "Simulating Crop Growth and Biogeochemical Fluxes in Response to Land Management Using the SALUS Model," in *The Ecology of Agricultural Landscapes: Long-Term Research on the Path to Sustainability*, Oxford University Press, pp. 225–274.

[6] L. Liu and B. Basso, "Spatial evaluation of switchgrass productivity under historical and future climate scenarios in Michigan," *GCB Bioenergy*, vol. 9, no. 8, pp. 1320–1332, 2017, doi: 10.1111/gcbb.12417.

[7] R. Martinez-Feria and B. Basso, "Predicting soil carbon changes in switchgrass grown on marginal lands under climate change and adaptation strategies," *GCB Bioenergy*, vol. 12, no. 9, pp. 742–755, 2020, doi: 10.1111/gcbb.12726.

[8] R. A. Martinez-Feria, B. Basso, and S. Kim, "Boosting climate change mitigation potential of perennial lignocellulosic crops grown on marginal lands," *Environ. Res. Lett.*, vol. 17, no. 4, p. 044004, Mar. 2022, doi: 10.1088/1748-9326/ac541b.
[9] Oak Ridge National Laboratory, "Policy Analysis System Model (POLYSYS)." 2017. [Online]. Available: https://bioenergymodels.nrel.gov/models/37/
[10] C. Hellwinckel, C. Clark, M. Langholtz, and L. Eaton, "Simulated impact of the renewable fuels standard on US Conservation Reserve Program enrollment and conversion," *GCB Bioenergy*, vol. 8, no. 1, pp. 245–256, 2016, doi: 10.1111/gcbb.12281.
[11] N. Abdoulmoumine, S. Adhikari, A. Kulkarni, and S. Chattanathan, "A review on biomass gasification syngas cleanup," *Appl. Energy*, vol. 155, pp. 294–307, Oct. 2015, doi: 10.1016/j.apenergy.2015.05.095.
[12] A. Kumar, D. D. Jones, and M. A. Hanna, "Thermochemical Biomass Gasification: A Review of the Current Status of the Technology," *Energies*, vol. 2, no. 3, Art. no. 3, Sep. 2009, doi: 10.3390/en20300556.
[13] S. S. Ail and S. Dasappa, "Biomass to liquid transportation fuel via Fischer Tropsch synthesis – Technology review and current scenario," *Renew. Sustain. Energy Rev.*, vol. 58, pp. 267–286, May 2016, doi: 10.1016/j.rser.2015.12.143.
[14] J. Frątczak, H. de Paz Carmona, Z. Tišler, J. M. Hidalgo Herrador, and Z. Gholami, "Hydrocracking of Heavy Fischer–Tropsch Wax Distillation Residues and Its Blends with Vacuum Gas Oil Using Phonolite-Based Catalysts," *Molecules*, vol. 26, no. 23, Art. no. 23, Jan. 2021, doi: 10.3390/molecules26237172.
[15] M. Luberti and H. Ahn, "Review of Polybed pressure swing adsorption for hydrogen purification," *Int. J. Hydrog. Energy*, vol. 47, no. 20, pp. 10911–10933, Mar. 2022, doi: 10.1016/j.ijhydene.2022.01.147.
[16] T. Schaaf, J. Grünig, M. R. Schuster, T. Rothenfluh, and A. Orth, "Methanation of CO2- storage of renewable energy in a gas distribution system," *Energy Sustain. Soc.*, vol. 4, no. 1, p. 2, Dec. 2014, doi: 10.1186/s13705-014-0029-1.
[17] Gas Technology Institute (GTI), "Low-carbon renewable natural gas (RNG) from wood wastes," Feb. 2019. [Online]. Available: https://www.gti.energy/wp-content/uploads/2019/02/Low-Carbon-Renewable-Natural-Gas-RNG-from-Wood-Wastes-Final-Report-Feb2019.pdf
[18] A. V. Bridgwater, "Review of fast pyrolysis of biomass and product upgrading," *Biomass Bioenergy*, vol. 38, pp. 68–94, Mar. 2012, doi: 10.1016/j.biombioe.2011.01.048.
[19] Z. Yang, A. Kumar, and R. L. Huhnke, "Review of recent developments to improve storage and transportation stability of bio-oil," *Renew. Sustain. Energy Rev.*, vol. 50, pp. 859–870, Oct. 2015, doi: 10.1016/j.rser.2015.05.025.
[20] Y. Zhang, T. R. Brown, G. Hu, and R. C. Brown, "Comparative techno-economic analysis of biohydrogen production via bio-oil gasification and bio-oil reforming," *Biomass Bioenergy*, vol. 51, pp. 99–108, Apr. 2013, doi: 10.1016/j.biombioe.2013.01.013.
[21] A. Pafili *et al.*, "Recent Progress in the Steam Reforming of Bio-Oil for Hydrogen Production: A Review of Operating Parameters, Catalytic Systems and Technological Innovations," *Catalysts*, vol. 11, no. 12, Art. no. 12, Dec. 2021, doi: 10.3390/catal11121526.
[22] Avello Bioenergy, "Bioasphalt binder- Avello Bioenergy." Accessed: Sep. 26, 2023. [Online]. Available: http://www.avellobioenergy.com/en/products/bioasphalt_binder/
[23] Z. Zhang, Y. Fang, J. Yang, and X. Li, "A comprehensive review of bio-oil, bio-binder and bio-asphalt materials: Their source, composition, preparation and performance," *J. Traffic Transp. Eng. Engl. Ed.*, vol. 9, no. 2, pp. 151–166, Apr. 2022, doi: 10.1016/j.jtte.2022.01.003.
[24] N. Su, F. Xiao, J. Wang, L. Cong, and S. Amirkhanian, "Productions and applications of bio-asphalts – A review," *Constr. Build. Mater.*, vol. 183, pp. 578–591, Sep. 2018, doi: 10.1016/j.conbuildmat.2018.06.118.

[25] X. Zhou *et al.*, "Life Cycle Assessment of Biochar Modified Bioasphalt Derived from Biomass," *ACS Sustain. Chem. Eng.*, vol. 8, no. 38, pp. 14568–14575, Sep. 2020, doi: 10.1021/acssuschemeng.0c05355.
[26] A. Ganguly, R. C. Brown, and M. M. Wright, "Techno-economic and greenhouse gas emission assessment of carbon negative pyrolysis technology," *Green Chem.*, vol. 24, no. 23, pp. 9290–9302, Nov. 2022, doi: 10.1039/D2GC03172H.
[27] L. J. Snowden-Swan *et al.*, "Conceptual Biorefinery Design and Research Targeted for 2022: Hydrothermal Liquefacation Processing of Wet Waste to Fuels," Pacific Northwest National Lab. (PNNL), Richland, WA (United States), PNNL-27186, Dec. 2017. doi: 10.2172/1415710.
[28] X. Zhang, X. Li, R. Li, and Y. Wu, "Hydrothermal Carbonization and Liquefaction of Sludge for Harmless and Resource Purposes: A Review," *Energy Fuels*, vol. 34, no. 11, pp. 13268–13290, Nov. 2020, doi: 10.1021/acs.energyfuels.0c02467.
[29] D. Humbird *et al.*, "Process Design and Economics for Biochemical Conversion of Lignocellulosic Biomass to Ethanol: Dilute-Acid Pretreatment and Enzymatic Hydrolysis of Corn Stover," NREL/TP-5100-47764, 1013269, Mar. 2011. doi: 10.2172/1013269.
[30] R. E. Davis *et al.*, "Process Design and Economics for the Conversion of Lignocellulosic Biomass to Hydrocarbon Fuels and Coproducts: 2018 Biochemical Design Case Update; Biochemical Deconstruction and Conversion of Biomass to Fuels and Products via Integrated Biorefinery Pathways," National Renewable Energy Lab. (NREL), Golden, CO (United States), NREL/TP-5100-71949, Nov. 2018. doi: 10.2172/1483234.
[31] R. Davis *et al.*, "Process Design and Economics for the Conversion of Lignocellulosic Biomass to Hydrocarbons: Dilute-Acid and Enzymatic Deconstruction of Biomass to Sugars and Catalytic Conversion of Sugars to Hydrocarbons," NREL/TP--5100-62498, 1176746, Mar. 2015. doi: 10.2172/1176746.
[32] International Renewable Energy Agency (IRENA), "Renewable Power Generation Costs in 2017," 2018. [Online]. Available: https://www.irena.org/-/media/Files/IRENA/Agency/Publication/2018/Jan/IRENA_2017_Power_Costs_2018.pdf
[33] W. J. Sagues, H. Jameel, D. L. Sanchez, and S. Park, "Prospects for bioenergy with carbon capture & storage (BECCS) in the United States pulp and paper industry," *Energy Environ. Sci.*, vol. 13, no. 8, pp. 2243–2261, Aug. 2020, doi: 10.1039/D0EE01107J.
[34] C. Li *et al.*, "Recent advancement in lignin biorefinery: With special focus on enzymatic degradation and valorization," *Bioresour. Technol.*, vol. 291, p. 121898, Nov. 2019, doi: 10.1016/j.biortech.2019.121898.
[35] A. Corona, M. J. Biddy, D. R. Vardon, M. Birkved, M. Z. Hauschild, and G. T. Beckham, "Life cycle assessment of adipic acid production from lignin," *Green Chem.*, vol. 20, no. 16, pp. 3857–3866, Aug. 2018, doi: 10.1039/C8GC00868J.
[36] D. R. Vardon *et al.*, "Adipic acid production from lignin," *Energy Environ. Sci.*, vol. 8, no. 2, pp. 617–628, Feb. 2015, doi: 10.1039/C4EE03230F.
[37] S. Brethauer and C. E. Wyman, "Review: Continuous hydrolysis and fermentation for cellulosic ethanol production," *Bioresour. Technol.*, vol. 101, no. 13, pp. 4862–4874, Jul. 2010, doi: 10.1016/j.biortech.2009.11.009.
[38] L. Tao, J. N. Markham, Z. Haq, and M. J. Biddy, "Techno-economic analysis for upgrading the biomass-derived ethanol-to-jet blendstocks," *Green Chem.*, vol. 19, no. 4, pp. 1082–1101, Feb. 2017, doi: 10.1039/C6GC02800D.
[39] W.-D. Huang and Y.-H. P. Zhang, "Analysis of biofuels production from sugar based on three criteria: Thermodynamics, bioenergetics, and product separation," *Energy Environ. Sci.*, vol. 4, no. 3, pp. 784–792, Mar. 2011, doi: 10.1039/C0EE00069H.

[40] C. M. Mendieta, R. E. Cardozo, F. E. Felissia, N. M. Clauser, M. E. Vallejos, and M. C. Area, "Bioconversion of wood waste to bio-ethylene: A review," *BioResources*, vol. 16, no. 2, pp. 4411–4437, Mar. 2021, doi: 10.15376/biores.16.2.Mendieta.
[41] D. Fan, D.-J. Dai, and H.-S. Wu, "Ethylene Formation by Catalytic Dehydration of Ethanol with Industrial Considerations," *Materials*, vol. 6, no. 1, Art. no. 1, Jan. 2013, doi: 10.3390/ma6010101.
[42] J. Han, L. Tao, and M. Wang, "Well-to-wake analysis of ethanol-to-jet and sugar-to-jet pathways," *Biotechnol. Biofuels*, vol. 10, no. 1, p. 21, Jan. 2017, doi: 10.1186/s13068-017-0698-z.
[43] S. Geleynse, K. Brandt, M. Garcia-Perez, M. Wolcott, and X. Zhang, "The Alcohol-to-Jet Conversion Pathway for Drop-In Biofuels: Techno-Economic Evaluation," *ChemSusChem*, vol. 11, no. 21, pp. 3728–3741, 2018, doi: 10.1002/cssc.201801690.
[44] P. T. Benavides, U. Lee, and O. Zarè-Mehrjerdi, "Life cycle greenhouse gas emissions and energy use of polylactic acid, bio-derived polyethylene, and fossil-derived polyethylene," *J. Clean. Prod.*, vol. 277, p. 124010, Dec. 2020, doi: 10.1016/j.jclepro.2020.124010.
[45] A. Dormer, D. P. Finn, P. Ward, and J. Cullen, "Carbon footprint analysis in plastics manufacturing," *J. Clean. Prod.*, vol. 51, pp. 133–141, Jul. 2013, doi: 10.1016/j.jclepro.2013.01.014.
[46] X. Zhong, X. Zhao, Y. Qian, and Y. Zou, "Polyethylene plastic production process," *Insight - Mater. Sci.*, vol. 1, no. 1, Art. no. 1, Dec. 2018, doi: 10.18282/ims.v1i1.104.
[47] Matches, "Matches' 275 Equipment Cost Estimates." Accessed: Sep. 26, 2023. [Online]. Available: https://www.matche.com/equipcost/Default.html
[48] A. Mohsenzadeh, A. Zamani, and M. J. Taherzadeh, "Bioethylene Production from Ethanol: A Review and Techno-economical Evaluation," *ChemBioEng Rev.*, vol. 4, no. 2, pp. 75–91, 2017, doi: 10.1002/cben.201600025.
[49] U.S. Environmental Protection Agency, "Plastics: Material-Specific Data." Accessed: Sep. 26, 2023. [Online]. Available: https://www.epa.gov/facts-and-figures-about-materials-waste-and-recycling/plastics-material-specific-data
[50] J. P. Dees, W. J. Sagues, E. Woods, H. M. Goldstein, A. J. Simon, and D. L. Sanchez, "Leveraging the bioeconomy for carbon drawdown," *Green Chem.*, vol. 25, no. 8, pp. 2930–2957, Apr. 2023, doi: 10.1039/D2GC02483G.
[51] P. Psarras *et al.*, "Cost Analysis of Carbon Capture and Sequestration from U.S. Natural Gas-Fired Power Plants," *Environ. Sci. Technol.*, vol. 54, no. 10, pp. 6272–6280, May 2020, doi: 10.1021/acs.est.9b06147.
[52] S. E. Baker *et al.*, "Getting to Neutral: Options for Negative Carbon Emissions in California," Lawrence Livermore National Lab. (LLNL), Livermore, CA (United States); Univ. of California, Berkeley, CA (United States); Negative Carbon Consulting, Half Moon Bay, CA (United States); Univ. of Calgary, AB (Canada); Univ. of Queensland, Brisbane, QLD (Australia); Univ. of California, Davis, CA (United States); Worcester Polytechnic Institute, MA (United States); Georgetown Univ., Washington, DC (United States); Valence Strategic, Washington, DC (United States), LLNL-TR-796100, Jan. 2020. doi: 10.2172/1597217.
[53] Progressive Management Publications, *21st Century Complete Guide to Biogas and Methane: Agricultural Recovery, Manure Digesters, AgSTAR, Landfill Methane, Greenhouse Gas Emission Reduction and Global Methane Initiative*. Progressive Management Publications, 2015. Accessed: Sep. 26, 2023. [Online]. Available: https://www.academia.edu/40544282/21st_Century_Complete_Guide_to_Biogas_and_Methane_Agricultural_Recovery_Manure_Digesters_AgSTAR_Landfill_Methane_Greenhouse_Gas_Emission_Reduction_and_Global_Methane_Initiative
[54] US Census Bureau, "2017 National Population Projections Tables: Main Series," Census.gov. Accessed: Sep. 27, 2023. [Online]. Available: https://www.census.gov/data/tables/2017/demo/popproj/2017-summary-tables.html

[55] World Highways, “US asphalt market seeing future growth,” World Highways. Accessed: Sep. 26, 2023. [Online]. Available: https://www.worldhighways.com/wh6/news/us-asphalt-market-seeing-future-growth
[56] H. Storz and K.-D. Vorlop, “Bio-based plastics: status, challenges and trends,” *Landbauforsch. - Appl. Agric. For. Res.*, no. 63, pp. 321–332, 2013, doi: 10.3220/LBF_2013_321-332.
[57] Grand View Research, “Adipic Acid Market Size, Share & Trends Analysis Report By Application (Nylon 6, 6 Fiber, Nylon 6, 6 Resin, Polyurethane, Adipate Esters), By Region (North America, Europe, Asia Pacific), And Segment Forecasts, 2023- 2030,” 2023. Accessed: Sep. 26, 2023. [Online]. Available: https://www.grandviewresearch.com/industry-analysis/adipic-acid-market
[58] Sherwood Lumber, “A Guide To Lumber Grades.” Accessed: Sep. 26, 2023. [Online]. Available: https://sherwoodlumber.com/a-guide-to-lumber-grades/
[59] Madison’s Lumber Report, “Utility-grade lumber prices jump, forestry labour stoppage resolved, sawmill capacity utilization improves,” Canadian Forest Industries. Accessed: Sep. 26, 2023. [Online]. Available: https://www.woodbusiness.ca/utility-grade-lumber-prices-jump-forestry-labour-stoppage-resolved-sawmill-capacity-utilization-improves/
[60] Statista, “Monthly price of lumber in the United States from January 2016 to April 2023,” Statista. Accessed: Sep. 26, 2023. [Online]. Available: https://www.statista.com/statistics/1239728/monthly-lumber-price-usa/
[61] P. Sharma, M. Kolhe, and A. Sharma, “Economic Analysis of a Building Integrated Photovoltaic System Without and With Energy Storage,” *IOP Conf. Ser. Mater. Sci. Eng.*, vol. 605, no. 1, p. 012013, Aug. 2019, doi: 10.1088/1757-899X/605/1/012013.
[62] U.S. Energy Information Administration, “Electricity explained: Factors affecting electricity prices.” Accessed: Sep. 26, 2023. [Online]. Available: https://www.eia.gov/energyexplained/electricity/prices-and-factors-affecting-prices.php
[63] Fuel Cell and Hydrogen Energy Association, “Road Map to a US Hydrogen Economy,” Oct. 2020. Accessed: Sep. 26, 2023. [Online]. Available: https://www.fchea.org/us-hydrogen-study

APPENDIX—CHAPTER 7

Land and Renewable Energy Analysis

Classification of Land Suitable for Renewable Energy and DACS Deployment

The goal of our suitable land analysis is to identify the potential areas that fit the physical and regulatory limitations of facility installations using geospatial analysis. We conducted suitable land analysis for the siting of renewable energy facilities (i.e., land-based wind and utility-scale solar photovoltaic) for DACS facilities. DACS facilities are assumed to be located in the same county as and powered by these renewable electricity facilities. Other types of renewables are not taken into consideration because they are projected to be more expensive than land-based wind and utility-scale solar photovoltaic, according to the Annual Technology Baseline [1]. Additionally, land is usually not a main constraint for the development of other types of renewables (e.g., geothermal).

The United States was divided into a grid with 30-meter resolution ("pixels") to align with the resolution of the 2019 National Land Cover Database (NLCD) [2]. The general workflow for determining the suitability of the land in each pixel is shown in **Figure A7-1**. Suitability criteria were applied based on general and technology-specific criteria, as detailed below.

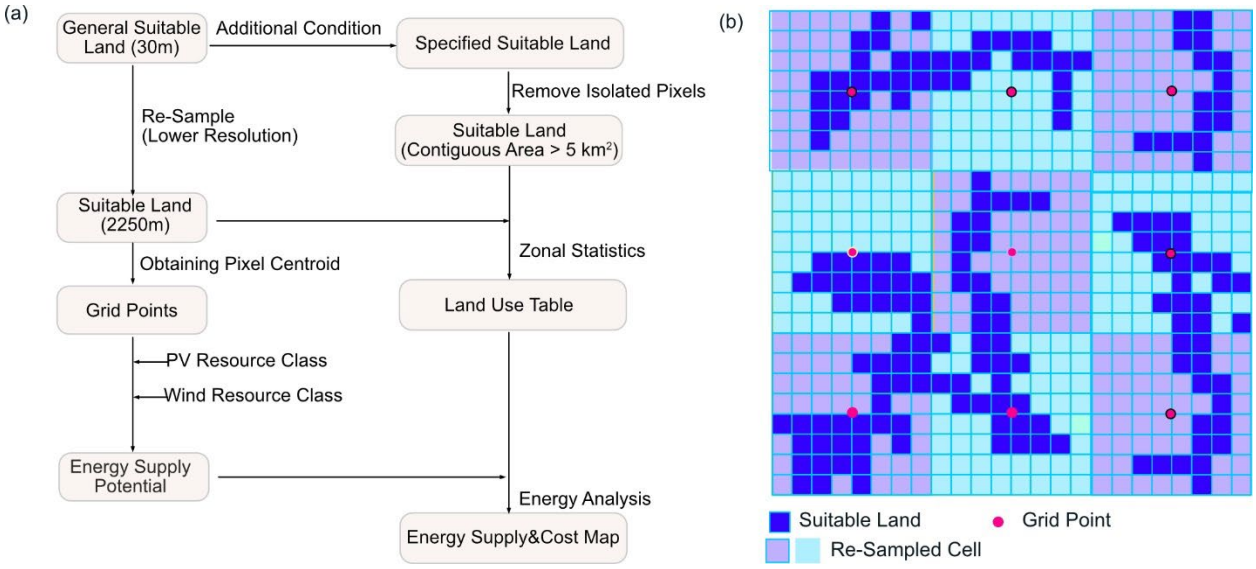

Figure A7-1. (a) Generalized schematic for land suitability analysis workflow. (b) Schematic depicting the process of aggregating the 30-meter resolution grid into 2250-meter grid and identifying grid points. This resampling process retains the information of the fraction of suitable land contained within each resampled cell.

The NLCD represents the land use in the Contiguous United States (CONUS) in 2019 and divides the land cover of the CONUS into 16 classes, including open water, perennial ice/snow, developed (4 subclasses), barren land, forest (3 subclasses), shrub/scrub, grassland/herbaceous, pasture/hay, cultivated crops, and wetlands (2 subclasses). The NLCD layer additionally serves as a reference layer of cell size (i.e., resolution), spatial reference and projection, spatial processing extent as well as a snap raster for any following geospatial analysis when applicable.

Conditions for land suitability are applied in two steps. First, the general criteria, which includes five conditions from the most critical to less critical, were applied to exclude this land from our analysis (Table A7-1). The general criteria can be categorized into three groups: current land cover (developed land, open water, and wetland), regulatory (e.g., the land identified as of critical environmental concern), and existing infrastructure (e.g., airports, railroads, buildings, and existing energy system infrastructure (power plants and transmission lines).

Table A7-1. General buffer conditions applied for land suitability analysis of wind and solar deployment for DACS.

Step	Condition	Notes	Data Source
0	NLCD	Open water excluded	[2]
1	Protected land	Protected Areas Database: Buffer distance = 3 km if GAP[a]-status = 1 or 2 (e.g., national parks) Buffer distance = 0 km if GAP[a]-status = 3 or 4 (e.g., state parks)	[3]
		National Conservation Easement Database: Buffer distance = 3 km if GAP[a]-status = 1 or 2 (e.g., national parks) Buffer distance = 0 km if GAP[a]-status = 3 or 4 (e.g., state parks)	[4]
		Areas of critical environmental concern: buffer distance = 3 km	[5]
		Roadless areas: buffer distance = 3 km	[6]
2	Wetlands	Buffer distance = 0.3 km	[2]
3	Developed	Buffer distance = 0 km	[2]
4	Other developed	Airports: buffer distance = 3 km	[7]
		Railroads: buffer distance = 0.015 km	[7]
		Transmission lines: buffer distance based on voltage	[7]
		Power plants: buffer distance = 3 km	[8]
		Buildings: buffer distance = 0.3 km	[9]
		Wind turbines: buffer distance = 3 km	[10]

[a] GAP = Gap Analysis Project

Second, technology-specific criteria were applied. For land-based wind and utility-scale solar photovoltaic, the criteria are summarized in Table A7-2. Different slope criteria were applied for wind and solar, with utility-scale solar requiring land that had a lower incline. We also excluded land that is projected to be occupied by wind/solar development for US grid decarbonization ("prioritized renewable energy area"), as identified by Denholm, *et al.* [11]. This study projected the US energy demand and obtained spatially explicit results for the expansion of clean energy facilities including wind and solar electricity and associated electricity transmission lines to meet this demand. We considered grid decarbonization to have higher priority than deployment of renewable electricity for DACS because DACS can potentially use electricity from the grid once the grid has been decarbonized, and DACS has the flexibility to use on-site purpose-built renewables when the land is far from population centers and transmission lines. See the subsection below on "Baseline Decarbonization Scenario" for additional discussion.

Table A7-2. Technology-specific conditions applied for land suitability analysis of wind and solar deployment for DACS.

Step	Condition	Data Source
Wind-1	Slope <20% (11.31°)	[12]
Wind-2	Out of prioritized renewable energy area	[11]

Wind-3	>5 km^2 contiguous area	Calculated
Wind-4	Not co-located with forests	[2]
Solar PV-1	Slope <5% (2.86°)	[12]
Solar PV-2	Out of prioritized renewable energy area	[11]
Solar PV-3	>5 km^2 contiguous area	Calculated
Solar PV-4	Not co-located with forests, pasture/hay or cultivated crops	[2]

For the remaining land that met all of the above criteria, we applied a condition of contiguous land area to remove isolated pixels. The contiguous condition excludes any pixels that form a connected area less than 5 km^2. We lastly excluded co-located areas, for wind energy, where forests account for >25% of the suitable land or, for utility-scale solar energy, where forests, pasture/hay or cultivated crops account for >25% of the suitable land. Sensitivity analysis on this co-location condition shows that varying the fraction from 5% (strict constraint) to 100% (no constraint) changes the availability of land by about one order-of-magnitude for both wind and solar (**Figure A7-2**). Compared to the Reference scenario from National Renewable Energy Laboratory's (NREL's) study, our results are more conservative in allowing land to be used for wind or solar, though it should be noted that we have removed the areas prioritized for grid decarbonization. The contiguous land condition accounts for the majority of the remainder of the difference.

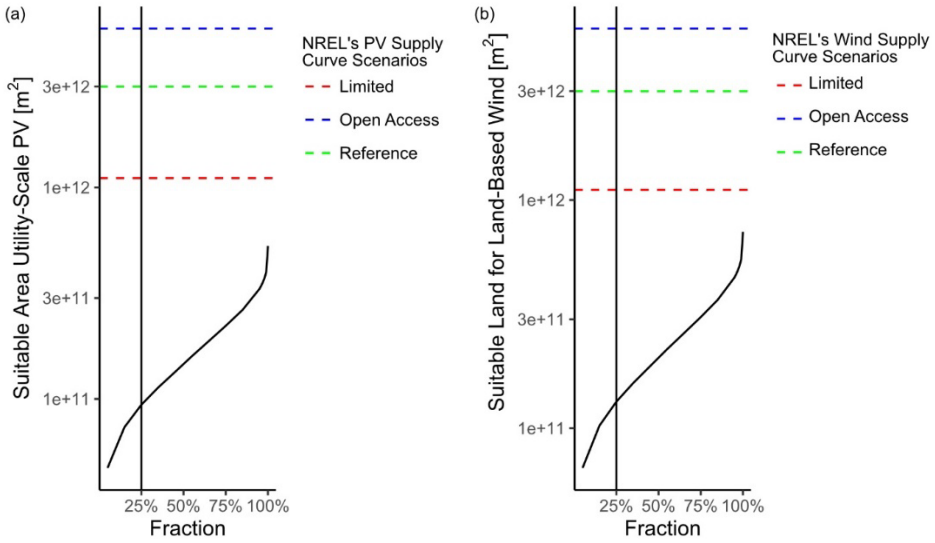

Figure A7-2. Sensitivity analysis on the fraction of some land types allowed to co-locate with renewable energy generation. Larger fraction indicates that the renewable energy is allowed to be co-located with an increasing cover of the excluded land types. (a) Solar photovoltaic, co-located with forests, pasture/hay, or cultivated crops. (b) Wind co-located with forests. Vertical line at 25% represents the cutoff used in our analysis, where no more than 25% of the land could be occupied by the excluded land types to allow development of the renewable energy resource.

At the end of this suitable land analysis, we were left with a 30-meter resolution grid of the United States that classified land as suitable or not suitable for development of renewable wind or solar resources to power DACS (Figure 7-10). We assumed that land deemed suitable for wind or solar energy development would also be suitable for DACS facilities due to the relative small footprint of the DACS facility compared to the renewable energy. DACS facilities are likely to have similar properties to wind turbines (e.g., tower height and noise level).

Our analyses are conducted at a 30-meter resolution, which is higher resolution than the previous studies. For example, Omitaomu, *et al.* used 100-meter resolution for identifying thermal power generating sites [13]. Lopez, *et al.* used 90-meter resolution for wind power siting [14]. Leslie, *et al.* used 4-kilometer resolution for solar and wind energy siting [15]. The higher resolution of our analysis led to several changes. First, by retaining high resolution, pixels of land use classes that would be excluded from use remain in the dataset, rather than disappearing when they are merged with neighbors at lower resolution. As a result, more pixels/land are identified as not suitable due to the land cover type. This results in a higher level of fragmentation in the land and more potential discontinuity, impacting the analysis from the contiguous land condition (Figure A7-3). Additionally, the slope calculated can vary based on the resolution. Buakhao and Kangrang show that, for the same area, the slope calculated at 90-meter resolution is 25% percent lower than the slope calculated at 30-meter resolution [16]. Finally, roads, railways, and low-voltage transmission lines disappear at lower resolution and so they are not properly accounted.

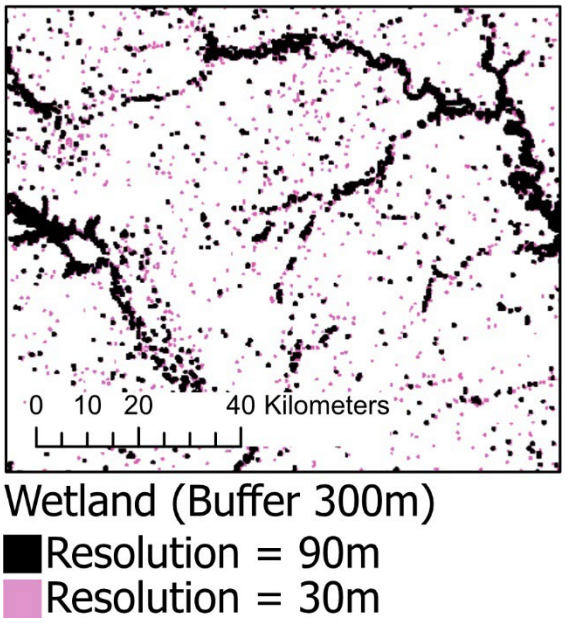

Figure A7-3. Example of land excluded by the wetland condition when the map is gridded with 30-meter resolution (excluded land shown in pink) vs. 90-meter resolution (excluded land shown in black). More pixels are excluded at the higher resolution due to the retention of land class information compared to lower resolution. This additionally impacts the areas that remain after application of the contiguous land condition.

We conducted land suitability and energy potential analysis for Alaska following a similar procedure with a few differences. We only considered wind energy and excluded solar photovoltaic as a primary renewable energy option because of the low solar resource in Alaska. Second, we calculated the capacity factor (CF) for wind energy based on a linear regression model using data from the wind energy supply curve (Figure A7-4). Finally, limited by data availability, fewer exclusion conditions representing the existing infrastructure were applied.

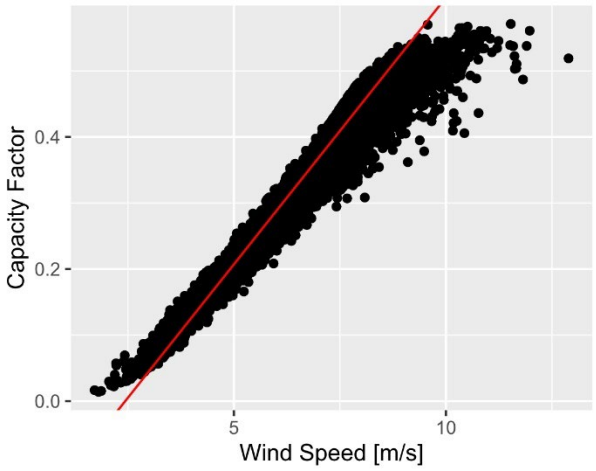

Figure A7-4. The capacity factor for land-based wind energy in Alaska was estimated based on wind speed.

Renewable Electricity Potential and Cost Analysis

After determining suitable land, the 30-meter resolution grid map was resampled into a 2250-meter resolution grid map to calculate the electricity generation potential of wind and solar (Figure A7-1). In this resampled map, each grid pixel represents approximately 5 km^2. The centroid of each pixel was identified as a grid point. At each grid point, the information about suitable land area is retained but information about land continuity is lost. We consider this an acceptable tradeoff to improve computational efficiency.

At each grid point *i*, the electricity generation potential $E_{i,j}$ in MWh/year with technology *j* (*j* is wind or solar) can be calculated as:

$$E_{i,j} = C_{i,j} \times CF \times 8760$$

where *CF* is the capacity factor, indicating the fraction of the year (8760 hours) that a facility is running at its nominal capacity and $C_{i,j}$ is the capacity of technology *j* that could be installed at grid point *i*, in MW, and is calculated as:

$$C_{i,j} = A_{i,j} \times PD_j$$

where $A_{i,j}$ is the area of land determined from the suitable land analysis, in km^2, and PD_j is the power density of the technology, in MW/km^2.

In our study, we considered constant power density for both technology classes across the United States. For utility-scale solar photovoltaic, we used the median value, 45 W/m^2 from a study by Bolinger and Bolinger [17]. By conducting a geospatial analysis of >90% of the existing utility-scale solar photovoltaic facilities in the United States, they found that the power density had increased by 52% and by 43% for fixed-tilt plants and tracking plants, respectively, from 2011 to 2019. This suggests that our median value is likely a conservative underestimate of power density for future solar installations.

The trend of power density of land-based wind energy remains unresolved. Earlier studies used a power density of ~3 W/m^2 but suggested that the power density would decrease as different turbines were selected [14,18,19]. A recent large-scale study found that the median power density of wind energy is closer to 4.3 W/m^2, but with substantial variation [20]. We used this median value in our study and note that studies on the methodology on power density of wind energy still need to be improved.

We estimated the costs of electricity from wind and solar using the results of the levelized cost of energy (LCOE) analysis in the Electricity Annual Technology Baseline (ATB), which projects the cost of renewable energy technologies through 2050 [1]. In all cases, we used the Moderate scenario.

We obtained spatially explicit estimates of LCOE based on the resource class of wind or solar, Table A7-3 and Table A7-4. For wind electricity, the resource class is based on the wind speed at a 120-meter height. For solar electricity, the resource class is based on the global horizontal irradiance (GHI). Both of these parameters have spatially explicit variation across the United States and are expressed in wind and solar supply curves [21,22].

Table A7-3. Land-based wind resource classes and levelized cost of electricity from the Electricity ATB.

Type	Min. wind speed (*m/s*)	Max. wind speed (*m/s*)	LCOE (*$/MWh*)
Land-based wind – Class 1	9.01	12.89	15.4
Land-based wind – Class 2	8.77	9.01	16.6
Land-based wind – Class 3	8.57	8.77	17.0
Land-based wind – Class 4	8.35	8.57	17.5
Land-based wind – Class 5	8.07	8.35	18.0
Land-based wind – Class 6	7.62	8.07	18.9
Land-based wind – Class 7	7.10	7.62	20.8
Land-based wind – Class 8	6.53	7.10	23.3
Land-based wind – Class 9	5.90	6.53	27.9
Land-based wind – Class 10	1.72	5.90	42.5

Table A7-4. Utility-scale solar photovoltaic resource classes and levelized cost of electricity from the Electricity ATB.

Type	Min. GHI (*kWh/m²/day*)	Max. GHI (*kWh/m²/day*)	LCOE (*$/MWh*)
Utility-scale solar– Class 1	5.75		13.2
Utility-scale solar– Class 2	5.50	5.75	13.6
Utility-scale solar– Class 3	5.25	5.50	14.3
Utility-scale solar– Class 4	5.00	5.25	15.1
Utility-scale solar– Class 5	4.75	5.00	16.1
Utility-scale solar– Class 6	4.50	4.75	16.8
Utility-scale solar– Class 7	4.25	4.5	17.6
Utility-scale solar– Class 8	4.00	4.25	18.5
Utility-scale solar– Class 9	3.75	4.00	19.4
Utility-scale solar– Class 10	0	3.75	21.2

In our analysis of renewable energy for DACS deployment shown in the main text of the report, we selected the technology with higher generation potential at each grid point and used state-level 2050-projected costs for electricity. However, we could have selected the technology with lower expected cost at each grid point using the analysis above. In this case, we obtain similar results—the land requirement, total generation potential, and median cost of electricity are all similar when comparing selecting technology based on generation capacity or cost (Figure A7-5). This is because wind and solar energy

have similar projected costs in 2050, particularly for comparable resource classes, although wind energy can potentially be more expensive. Wind power has a looser constraint on land use (i.e., slope and co-location limitations) but solar photovoltaic has almost an order of magnitude higher power density. As a result, lands that are only suitable for wind power development can have a low wind resource class, leading to a broader distribution of costs in the maximum potential scenario.

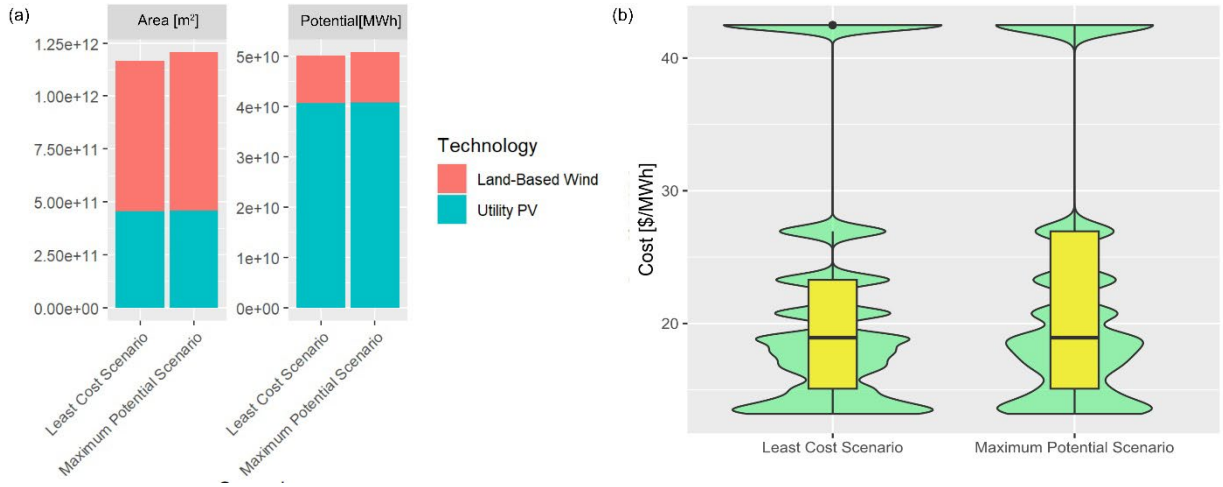

Figure A7-5. Impact of selecting grid-level electricity generation technology based on least cost vs. maximum generation potential. Similar results are obtained when comparing land use, generation potential, and median cost of electricity.

Baseline Decarbonization Scenario

The exclusion of land that would be prioritized for grid decarbonization (and thus unavailable for CO_2 removal) was based on a previous study examining the transition to a 100% clean electricity system [11] This study first determined two demand scenarios, the "Reference-AEO," which represents the electricity demand under current policy, and the "Reference-ADE," which represents an accelerated electrification scenario and has a much higher load growth. The study then evaluated four primary scenarios that achieve 100% clean electricity supply in 2035 and afterwards to meet such a demand. These scenarios include "All-Options," which assumes continuous improvement of electricity generation technologies and deployment of DACS; "Infrastructure Renaissance," which allows greater expansion of electricity transmission deployment; "Constrained," which limits the deployment of new generation capacity and transmission; and "No CCS," which assumes CCS technologies on power plants will not achieve a cost-competitive deployment status by 2035. For our analysis, we used the results in year 2050 from the "All-Options" scenario as the baseline decarbonization scenario, as it is the only scenario that deployed DACS.

NREL's 100% clean electricity used their wind [21] and solar supply curves [22] for the energy facility siting analysis [14]. Our land suitability and renewable energy supply analysis applied similar constraints as the wind and solar supply curves but with some notable differences. In NREL's supply curve, all land cover types are considered as suitable, which allows the co-location of solar with forested, pasture/hay, or cultivated lands. Our approach, on the other hand, posed some restrictions on this type of land use change. We first identified the fraction of each land cover type (i.e., barren, forest, shrubland, herbaceous, pasture/hay, and cultivated crops) in each analysis grid space. Co-location criteria were then applied, which excluded wind energy development in areas with more than 25% forest, and solar development in areas with more than 25% of forest, pasture/hay, or cultivated crops. We consider this a

more conservative approach to land use change that additional helps deconflict land use for other types of CO_2 removal.

It is important to note that recent analysis suggests that existing estimates of renewable-energy technical potential, such as those used in the NREL grid decarbonization report and our report, may be too high due to emerging development of local zoning ordinances around setbacks on wind and solar installations [23].

DACS Cost Model

Direct Air Capture Cost Models, Methodology and Parameters

Overviews of the liquid solvent and solid adsorbent DAC processes modeled are given in the main text. For solid adsorbent DAC, we developed a cost model based on a modular, amine-based adsorbent DAC system featuring vacuum-steam-swing adsorption [24]. We used a fixed cycle time (adsorption + desorption) and a fixed cycle working capacity for each cycle, modulated by local climate (temperature and humidity). The working capacity was modeled to degrade over time (Table A7-5), which determined an adsorbent lifetime as well as the lifetime-integrated average working capacity. These values, along with capacity factor and net CO_2 removal efficiency, were used to determine the quantity of adsorbent required for a fixed plant scale. We used an arbitrary monolithic contactor with specified channel sizes to determine pressure drop and fan power. The contactor was assumed to have a much longer lifetime than the adsorbent itself, as amine-based adsorbents suffer from oxidative (and other) degradation modes [25,26].

The first-of-a-kind (FOAK) value for steam requirement (Table A7-5) was a conservative value as the midpoint of the "today" and "future" steam requirements from Deutz and Bardow [27]. In our technology learning model, the required amount of steam for regeneration decreased following a learning curve with fixed endpoints (FOAK value at initial deployment, fully learned at 2050 deployment). Improvements in adsorbent lifetime are assumed to be captured by the relatively high component learning rate used for the adsorbent cost that effectively results in a lower cost for adsorbent.

Geospatially resolved costs for solid adsorbent DACS (Figure 7-13) were computed using local projected CO_2 storage costs, state-level electricity costs (Table A7-8), a plant scale based on nearby renewable generation potential (Table A7-6), and local climate data.

For liquid solvent DAC, we adapted a cost model from Keith, *et al.* and our previous report [24,28]. We adjusted some economic factors and included updated natural gas cost, local CO_2 storage costs, and technology learning (Table A7-7). In general, we used a fixed plant scale of 1,000,000 tonnes of CO_2 per year due to the significant economies of scale for equipment used in the liquid solvent process and the condition of siting these facilities in regions with natural gas reserves.

We determined that electrification via electric kiln technologies is feasible for liquid solvent DAC, which are available from some suppliers today, but we currently do not have sufficient information regarding the cost, lifetime, maintenance, and overall process balance and modeling using an electric kiln to make confident projections of cost and deployment. This does not imply that this is not a plausible technology development pathway, especially considering the joint interest in electrified kiln technologies for solid mineral-based DAC technologies and potential synergies with the cement and other high-temperature industries.

Table A7-5. Solid adsorbent DACS air contactor parameters.

Parameter	Units	Baseline value
Baseline adsorbent cycle working capacity (@ 30°C, dry)	$mol_{CO2}/kg_{adsorbent}$	0.8
Structured contactor requirement	$kg_{contactor}/kg_{adsorbent}$	0.2
Average CO_2 removal efficiency	%	75
Full cycle time	min	20
Degradation rate constant, k [a]		5.1×10^{-5}
Fractional capacity at sorbent replacement	%	70
Adsorbent lifetime	y	0.3
Contactor lifetime	y	10
Contactor length	m	0.3
Contactor channel size	mm	0.5
Regeneration steam requirement [b]	GJ/t_{CO2}	12.1
Heat pump coefficient of performance [c]		2.5

[a] Based on 30% loss of initial working capacity after 7000 cycles. Residual capacity = $(1–k)^n$ where n is the number of cycles.

[b] First-of-a-kind steam requirement based on a midpoint between "today" and "future" steam requirement from Deutz and Bardow [27]. Steam requirement decreases with technology learning toward a target value as described in the main text.

[c] Based on a hybrid heat pump system using recovered heat from excess steam and air and/or low-grade process, waste, or renewable heat sources (Figure 7-4).

Table A7-6. Solid adsorbent DACS facility scale and cost parameters.

Parameter	Units	Baseline value
Plant scale a (low nearby generation)	tCO_2/y	100,000
Plant scale a (moderate nearby generation)	tCO_2/y	300,000
Plant scale a (high nearby generation)	tCO_2/y	1,000,000
Capacity factor		0.9
Average storage cost b	$\$/tCO_2$	7.75
Storage cost range	$\$/tCO_2$	3.95 - 135
Labor and maintenance	% total OPEX	4.5
Balance of plant CAPEX	% total CAPEX	10
Capital scaling factor	$\$_{overnight}/\$_{bare}$	4.5
Plant lifetime	y	20
Capital discount rate	%	12.5

[a] Based on nearby potential renewable energy generation. Low nearby generation: <10,000 MWh per year; Moderate nearby generation: between 10,000 and 100,000 MWh per year; High nearby generation: >100,000 MWh per year.

[b] An average storage cost across likely DAC deployment regions, see Chapter 4.

Table A7-7. Liquid solvent DACS facility scale and cost parameters.

Parameter	Units	Baseline value
Plant scale [a]	t_{CO2}/y	1,000,000
Capacity factor		0.9
Weighted average storage cost	$\$/t_{CO2}$	7.75
Storage cost range	$\$/t_{CO2}$	3.95 - 135
Balance of plant CAPEX	*% total CAPEX*	18
Installation factor	$\$_{overnight}/\$_{bare}$	3.2
Plant lifetime	*y*	20
Capital discount rate	*%*	12.5
Unit Scaling Factor		**Value**
Calciner, slaker		0.745
Contactors (including fans)		1
Pellet reactor		1
Air supply unit		0.6
Compressors		0.77
Filters		1
Power island		0.6

[a] A fixed plant scale of 1,000,000 tonnes of CO_2 per year was used for cost modeling due to the availability of natural gas resources. In some cases, e.g. FOAK cost modeling, a different plant scale was used (e.g. 300,000 tonnes of CO_2 per year).

Additional Assumptions for Near-term DAC Costs

The costs of three processes were estimated for near-term deployment: solid adsorbent direct air capture and storage (DACS) with electrified heat-pump-generated steam, solid adsorbent DACS with natural-gas-generated steam, and liquid solvent DACS with natural-gas-fired kiln. The natural-gas-powered solid adsorbent DAC process was based on a previous report [24] and was only modeled for 2025. Compared to the process modeled for 2050, the heat pump steam generation system was removed and was replaced by natural gas-fired steam purchased at $3.20/GJ and generated without capturing the natural gas combustion emissions. This significantly decreased the net carbon removed from this process. The natural-gas-powered liquid solvent DAC process was based on peer-reviewed literature and other publications [28,29].

For cost parity, liquid solvent and solid adsorbent plant scales were fixed at nameplate capacity of 300,000 tonnes of CO_2 per year for near-term deployments. Technology learning was not applied. No CO_2 transport costs were used, as facilities were assumed to be constructed with co-located storage due to the high cost of transport and relative abundance of locations with the potential for storage, in agreement with 2050 deployment projections. A fixed cost of storage was used based on long-term projections for storage cost; this is likely an underestimate for near-term deployments.

For location-agnostic cost estimates (Figure 7-6), fixed conditions of 15°C and 55% relative humidity were used. These values are roughly the average of those from two representative regions for DAC deployment (West Texas and Upper Rocky Mountains). A detailed description of the impact of local climate on DACS costs is found below. For spatially resolved climate data in a state, the data were averaged across all geographic points to generate a single series of daily average temperature and relative humidity. Using representative cases, the error generated by this approach rather than projecting cost for each geographic point and time series was negligible. For state-level, near-term DACS cost projections (Figure 7-8), state-specific climate [30], electricity purchase price, and electricity grid carbon intensity (**Table A7-8**) were used.

Utilizing single, state-level electricity prices is a simplified approach to analyzing the real cost of electrical power for DACS. The next level of refinement of this analysis would treat electricity prices at the independent service operator (ISO) level rather than a state-level. Realistically, electricity prices would be set by power purchase agreements between DACS developers and electricity providers. It is unlikely that near-term DACS deployments would primarily be powered by grid-connected electricity, so 2025 state-level electricity prices are merely a representative data input. In the case of a future decarbonized grid, the optimal approach to grid integration and balancing of significant electrically powered DACS deployment is itself an open research question. While utilizing single average state-level prices is reductive, detailed integration with highly variable electricity pricing at the service operator level was outside the scope of this work.

Table A7-8. U.S. state-specific electricity price, grid carbon intensity, and natural gas price data used in cost modeling.

State	"2025" electricity purchase price ($/MWh)[a]	"2025" grid carbon intensity (gCO_2/kWh)[b]	"2025" natural gas price ($/1000 cu. ft.)[c]	2050 electricity purchase price ($/MWh)[d]
Alabama	72.1	538	4.85	92.2
Alaska	192	347	5.20	217
Arizona	77.4	483	6.41	80
Arkansas	74.9	315	7.76	74.7
California	169	228	9.75	93.8
Colorado	91.3	547	7.13	53.8
Connecticut	110	248	7.63	130
Delaware	86.6	571	11.59	127
D.C.	89.7	531	—	101
Florida	87.2	390	6.40	104
Georgia	74	350	5.44	106
Hawaii	309	699	25.10	349
Idaho	72.8	152	3.88	89.1
Illinois	83.2	314	7.57	81.4
Indiana	84.2	747	6.86	87.5
Iowa	75.6	430	7.08	67.3
Kansas	84.1	401	5.22	57.2
Kentucky	67.8	801	4.99	99.4
Louisiana	70.8	464	4.03	80.3

State	"2025" electricity purchase price ($/MWh)[a]	"2025" grid carbon intensity (gCO_2/kWh)[b]	"2025" natural gas price ($/1000 cu. ft.)[c]	2050 electricity purchase price ($/MWh)[d]
Maine	109	209	9.18	116
Maryland	96.4	314	9.10	122
Massachusetts	173	430	10.13	127
Michigan	87.6	475	6.70	90.9
Minnesota	94.5	391	5.47	65.5
Mississippi	67.8	378	5.66	83
Missouri	81	774	6.53	71.2
Montana	71.1	511	7.14	76.6
Nebraska	82.7	559	5.36	57.1
Nevada	68.6	332	5.59	87
New Hampshire	157	131	9.53	122
New Jersey	122	240	9.42	130
New Mexico	70.2	488	6.03	50
New York	72.2	226	8.38	115
North Carolina	70	317	6.33	105
North Dakota	84	640	4.63	45.1
Ohio	74.6	547	8.00	101
Oklahoma	62.7	344	4.52	60.6
Oregon	68	142	5.07	94.2
Pennsylvania	74.5	331	8.51	118
Rhode Island	183	381	9.81	128
South Carolina	69.2	255	5.60	99.7
South Dakota	91.4	145	6.06	55.3
Tennessee	62.8	342	5.50	91.8
Texas	69.7	427	4.96	66.3
Utah	70.5	697	5.43	81.1
Vermont	130	4.99	5.15	110
Virginia	74	294	5.16	116
Washington	66.2	99.3	8.21	97.6
West Virginia	69.2	877	3.76	109
Wisconsin	86.9	565	6.98	78.2
Wyoming	77.8	843	5.76	54.4
US average	94.1	388	—	65.1

[a] U.S. Energy Information Administration, EIA-861 (https://www.eia.gov/electricity/data/state/), 2021, Total Electric Industry, Industrial price, projected to 2025 from 2021 (14% increase)

[b] U.S. Energy Information Administration, 2021 Total Emission Rate from Table 7. Electric power industry emissions estimates (State Electricity Profiles: https://www.eia.gov/electricity/state/<statename>/)

[c] U.S. Energy Information Administration, 2022. For 2050, a fixed natural gas price of $3.98/1000 cu. ft. was used.

[d] NREL, Cambium 2022, Mid-case with 100% decarbonization by 2035, 2050 projected. US average is a weighted average of state-level 2050 projected electricity prices by potential renewable generation capacity.

Impact of Local Climate on DAC Performance

Local temperature and humidity impact the performance (i.e., CO_2 productivity or capture rate) as well as energy efficiency of DAC processes. We incorporated productivity data from Sendi, *et al.* [31] (for adsorbent) as well as capture rate and energy requirement data from An, *et al.* [32] (for solvent) into our geospatial analysis. **Figure A7-6** shows the relative productivity coefficients from the references used in our model for adsorbent and solvent DAC. Process productivity can vary by as much as two-fold across typical seasonal climatic conditions. For solid adsorbent DAC, we adapted process productivity data from Sendi, *et al.* to adjust the cycle working capacity of the adsorbent as a process input (Table A7-5). For liquid solvent DAC, we adjusted the process capture efficiency (and, as a result, CO_2 productivity) as well as calciner and combined cycle thermal loads with data from An, *et al*.

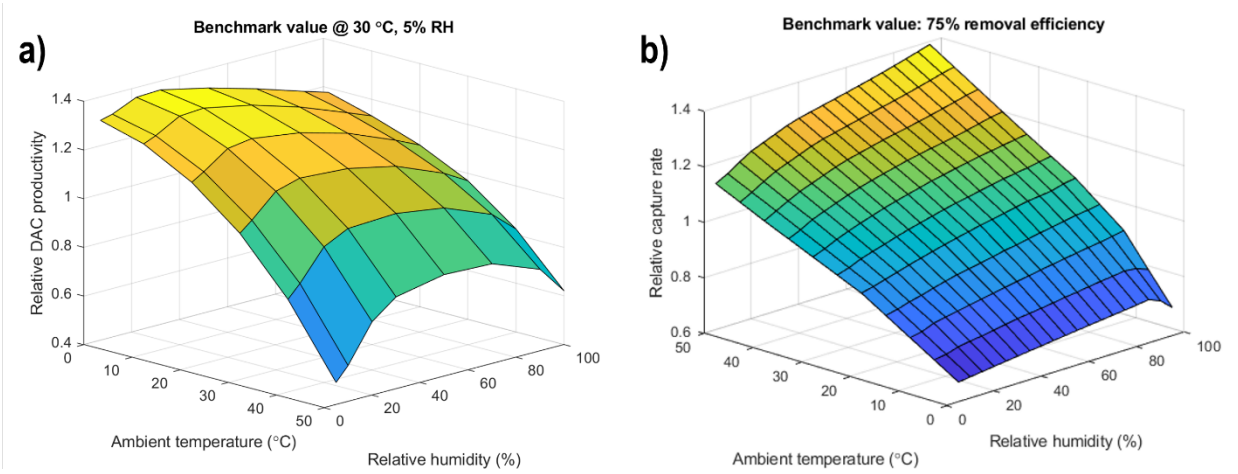

Figure A7-6. (a) Relative solid amine-based adsorbent DAC productivity as a function of temperature and relative humidity (adapted from Sendi, et al. [31]). (b) Relative capture rate for liquid hydroxide solvent DAC as a function of temperature and relative humidity (adapted from An, et al. [32]). Color indicates the relative productivity/capture rate value on the vertical axis. Values were interpolated from reference data.

For our long-term (2050) analysis, we used spatially-resolved projected climate data (NASA, NEX GDDP CMIP6, SSP2-4.5, 2050 projected) [33], which feature daily temperature and humidity averages at a 25 km resolution. For each geographic point considered, we selected the nearest point in the 2050 climate dataset. For adsorbent DAC, an adjusted daily cycle working capacity was computed and then averaged to yield a climate-adjusted average working capacity model input. Calculating a daily average working capacity and then averaging was a more robust approach than utilizing a single yearly averaged climate input due to the non-linearity of the productivity response. We compared daily vs. hourly resolved climate data [30] and found a ≤5% deviation when using daily averaged climate data compared to hourly. Representative daily temperature, temperature differential (T_{max}–T_{min}), and dewpoint data for three locations of interest for DACS (Wyoming, Louisiana, and West Texas) from the 2050 climate dataset used are shown in **Figure A7-7**.

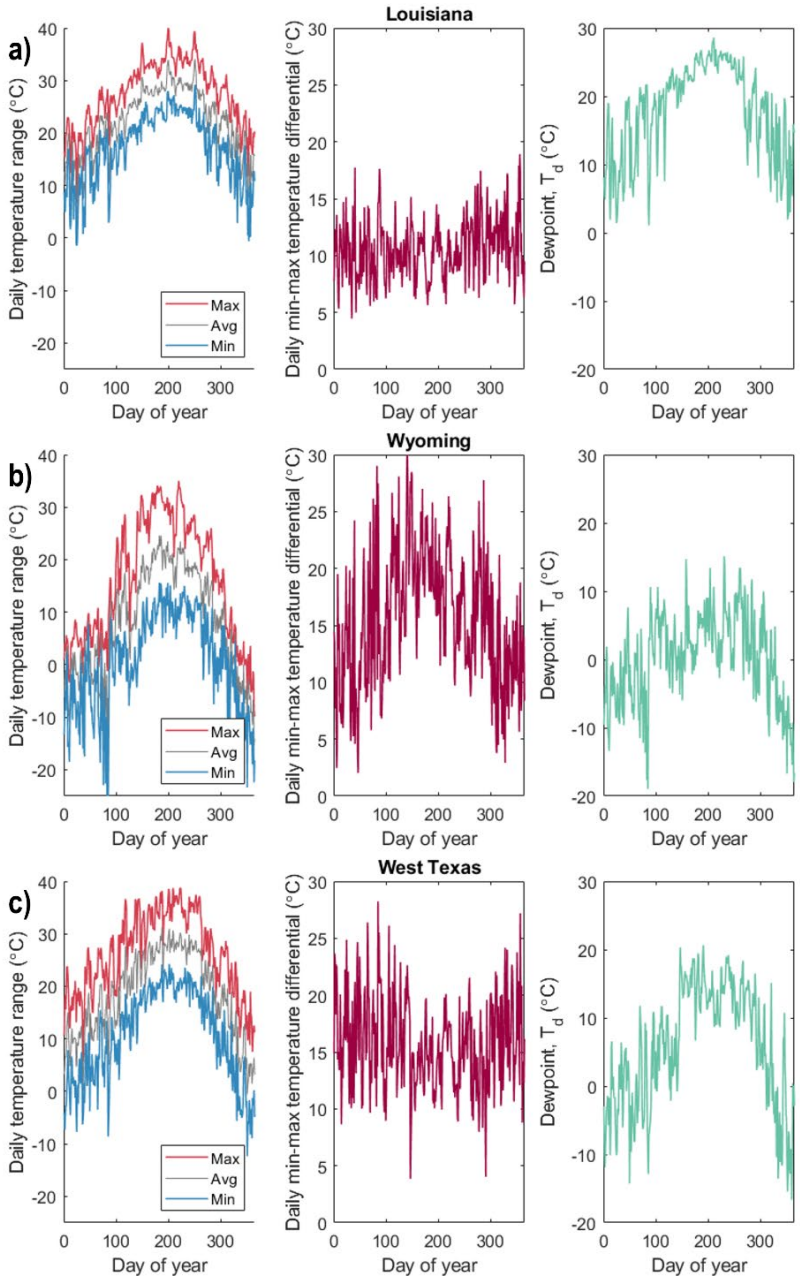

Figure A7-7. Daily mean temperature range (min, max, average), maximum temperature differential (max–min), and average dewpoint for (a) Louisiana, (b) Wyoming, and (c) West Texas, locations likely relevant for DACS deployment. Data from NASA, NEX GDDP CMIP6, SSP2-4.5, 2050 projected [33].

Determination of Net CO_2 Removed

For a DACS facility with a given nameplate operating capacity, the net CO_2 removed will be less than the gross CO_2 captured from the atmosphere after accounting for energy and resource utilization. For a real facility, a full lifecycle analysis (LCA) is necessary to determine the true net CO_2 removed, accounting for resource intensity during construction and facility startup, operation, and at end of life. In this analysis, we did not perform a full LCA, but we do account for the embodied CO_2 emissions, or carbon intensity, of the energy inputs of the DACS processes modeled, as described below.

The processes considered in this analysis utilized electricity and/or natural gas as primary energy inputs, each of which has associated emissions. Electricity has a certain carbon intensity depending on its origin, which can be very low if using renewable electricity or a decarbonized grid, or very high if using electricity from fossil-fueled power plants that do not capture their emissions. Combusted natural gas has positive CO_2 emissions, if not captured, as well as potential methane emissions from upstream leakage; we considered both of these emissions in calculating net CO_2 removed. Unless otherwise noted, a 100-year global warming potential was used for methane.

In certain cases, such as a natural gas-powered liquid solvent DAC system that captures most of the CO_2 emissions from natural gas combustion, the total CO_2 stored is partially the captured emissions from natural gas and partially the CO_2 removed from the atmosphere. The cost of handling, transporting, and storing all of the CO_2 was considered, but only the CO_2 originating from the atmosphere was considered in the gross CO_2 removed.

For a given process, the net CO_2 removed is determined by:

$$CO_{2,net} = CO_{2,gross} - \left(CO_{2,elec} + CO_{2,NGcombust} + CO_2e_{NGleak}\right)$$

and

$$\alpha_{rem} = \frac{CO_{2,net}}{CO_{2,gross}}$$

with

$$CO_{2,gross} + CO_{2,NGcombust} = CO_{2,stored}$$

$$CO_{2,elec} = P_{elec} \times CI_{elec}$$

$$CO_{2,NGcombust} = f_{CH4} \times (1 - \alpha_{CH4}) \times \frac{M_{W,CO2}}{M_{W,CH4}}$$

$$CO_2e_{NGleak} = f_{CH4} \times \alpha_{leak} \times GWP_{CH4}$$

where $CO_{2,net}$ is the net CO_2 removed by a DACS facility, $CO_{2,gross}$ is the gross CO_2 captured and removed from the atmosphere, $CO_{2,elec}$ is the CO_2 emissions associated with the input electricity, $CO_{2,NGcombust}$ is the un-captured CO_2 emissions from natural gas combustion, CO_2e_{NGleak} is the equivalent CO_2 emissions from upstream natural gas leakage, and $CO_{2,stored}$ is the total CO_2 geologically stored, all in tonnes CO_2 equivalent per year. α_{rem} is the fraction of CO_2 captured from the air that is net removed. P_{elec} is the electricity input requirement of the DAC facility in MWh per year, CI_{elec} is the carbon intensity of the input electricity in kg CO_2 per MWh. f_{CH4} is the input flow rate of natural gas required for DACS operation in tonnes per year, α_{CH4} is the fraction of CO_2 emissions from natural gas combustion that is captured and stored, α_{leak} is the upstream leakage rate of methane, GWP_{CH4} is the global warming potential of methane, and M_W is the molecular weight of CO_2 or CH_4.

State-specific Building Costs

Our baseline cost models reported in the main report do not consider variations in local building costs across the United States. Generally, there is strong correlation between state-level electricity costs and state-level building costs. As a result, projected deployment of grid-connected electrically powered DACS already contains a significant state-level cost factor. However, the 2050 natural gas price for natural gas-powered solvent DACS was a fixed value for all states, thus eliminating a significant source of geospatial cost variance. We performed an additional analysis using state-specific building costs from the US DoD Facilities Pricing Guide [34]. State-specific building cost coefficients were calculated by averaging the area cost factor for all sites per state (Table A7-9). The overnight capital costs of each component were

multiplied by these factors. To note, for adsorbent DAC, the adsorbent and contactor costs were not multiplied by the state-level cost coefficient. The resulting change in total cost of DACS for 2050 adsorbent and solvent DACS by county is shown in **Figure A7-8**. The change in total cost for solvent DACS is much more greatly affected by the inclusion of state-level building costs. The most significant impact is on Alaska, which has a building cost coefficient of 2.7, which *greatly* increases the overall modeled cost of DACS.

Table A7-9. State-level building cost coefficients used in the analysis contained within this Appendix section.

State	Average area cost factor [a]	State	Average area cost factor [a]
Alabama	0.835	Montana	1.084
Alaska	2.718	Nebraska	0.913
Arizona	0.935	Nevada	1.150
Arkansas	0.910	New Hampshire	1.080
California	1.205	New Jersey	1.192
Colorado	1.037	New Mexico	0.933
Connecticut	1.136	New York	1.127
Delaware	1.121	North Carolina	0.879
D.C.	1.04	North Dakota	1.118
Florida	0.858	Ohio	0.961
Georgia	0.859	Oklahoma	0.909
Hawaii	2.175	Oregon	1.168
Idaho	0.988	Pennsylvania	1.090
Illinois	1.078	Rhode Island	1.138
Indiana	0.916	South Carolina	0.926
Iowa	0.988	South Dakota	0.982
Kansas	0.911	Tennessee	0.846
Kentucky	0.914	Texas	0.894
Louisiana	0.887	Utah	1.093
Maine	1.077	Vermont	1.001
Maryland	0.995	Virginia	0.973
Massachusetts	1.180	Washington	1.142
Michigan	1.021	West Virginia	0.972
Minnesota	1.102	Wisconsin	1.092
Mississippi	0.798	Wyoming	1.022
Missouri	0.949		

[a] US DoD Facilities Pricing Guide (UFC 3-701-01) [34]. Average of area cost factors by state (Table 4-1, CONUS).

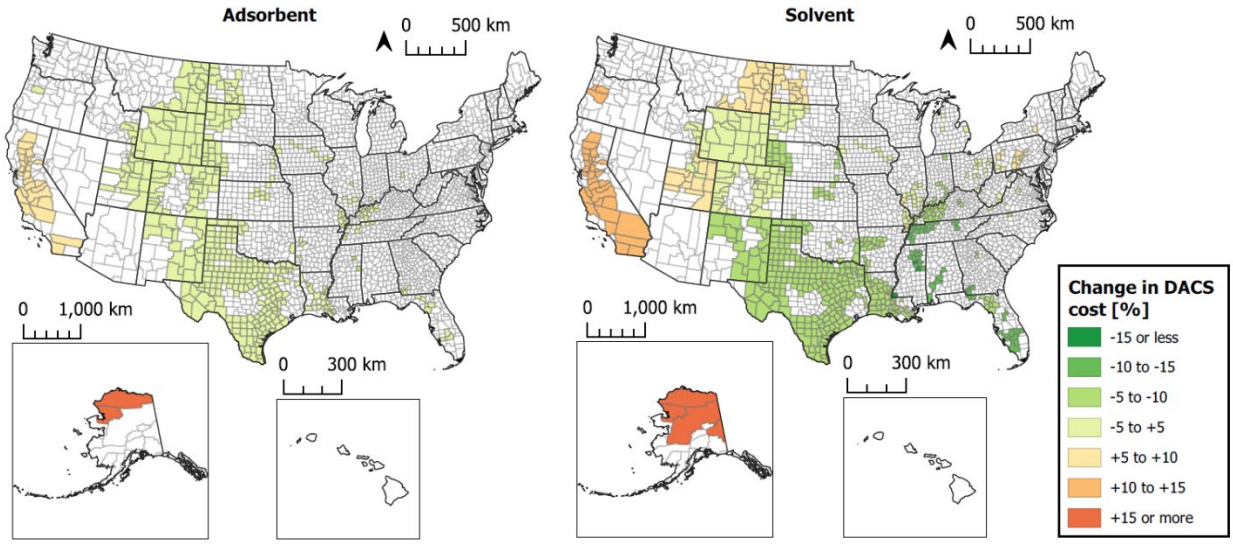

Figure A7-8. Percent change in total cost for adsorbent and solvent DACS (2050) after applying state-specific cost factors.

Technology Learning

Learning curves for solid adsorbent and liquid solvent DAC were constructed using component-specific learning rates following typical learning curve models (Figure 7-12). This approach was chosen to reflect a more nuanced approach to technology learning, particularly in a field where some components are taken directly from mature industries (e.g., kilns) while other components are emergent, modular, and rapidly evolving (e.g., solid adsorbent contactor modules). Still, this approach is not meant to be precise to a component level; the overall learned cost, reflecting a sum of components with different learning rates, is the main result worth considering. Overall, learning and costs on individual components may evolve at different rates, and integration and efficiencies would be largely reflected in difficult-to-project costs such as balance of plant and installation factors. Component learning was calculated as:

$$C_i = C_{i,0} \times (1 - L_r)^d$$

where C_i is the learned cost of a component, $C_{i,0}$ is the FOAK cost of a component, L_r is the learning rate, and d is the number of doublings in deployment from the FOAK scale:

$$d = \log_2(D/D_0)$$

where D is the global deployment of a specific DAC technology and D_0 is the FOAK scale of that technology.

For cost analyses used to compute technology learning curves, we generally used the assumptions for long-term (2050) DAC deployment (i.e., renewable electricity grid and carbon intensity). As with generic FOAK costs, we assumed a location-agnostic climate of 15°C and 55% RH. We used fixed prices for electricity and natural gas (2050, Table A7-8) and assumed a 100-year global warming potential and 2.3% natural gas upstream leakage rate. We used fixed plant scales of 300,000 and 1,000,000 tonnes of CO_2 per year for solid adsorbent and liquid solvent DAC, respectively. We computed a weighting factor for the long-term (2050) cost of DAC for each technology based on a weighted average cost over the learning curve. These factors were 1.04 and 1.09 for solvent and adsorbent DAC, respectively.

Using Natural Gas for DAC

Estimation of Natural-Gas Reserves for Liquid Solvent DACS

We estimated the amount of US domestic natural-gas reserves based on the amount of technically recoverable resources of dry natural gas reported by the US Energy Information Administration [35]. These reserves are broken down into two types: proved and unproved resources. Proved reserves of natural gas are the volumes that are currently estimated to be produced under existing economic conditions. Unproved resources have been confirmed by exploratory drilling and are technically recoverable based on current technology but without consideration of economic or other operating conditions. Despite increased natural-gas consumption, estimates of proved reserves have steadily increased over the past two decades due to the introduction of horizontal drilling and hydraulic fracturing that have increased production of natural gas from shale formations [36]. Given the long-term outlook of this report, we chose to examine both proved and unproved reserves, assuming that recovering unproved reserves would eventually become economically feasible (Table A7-10). Therefore, our estimates represent an upper bound to the amount of natural gas that will be available in the future.

Table A7-10. Estimates of domestic natural gas reserves, by region identified in this report. Data from the U.S. EIA [35,36].

Roads to Removal region	Proved natural gas reserves (Tcf)[a]	Unproved natural gas reserves (Tcf)[a]
Alaska	98	241
Appalachia	99	544
California Central Valley	1	—
Desert Southwest	—	—
East Cascades	—	—
Florida Peninsula	—	—
Great Basin	—	—
Hawaii	—	—
Lower Great Lakes	32	122
Lower Midwest	—	—
Lower Mississippi River	—	—
Lower Rocky Mountains	23	74
Northeast	53	93
Northeastern Cities	—	—
South Central	126	360
Southeast	8	21
Upper Great Lakes	1	10
Upper Midwest	9	20
Upper Rocky Mountains	16	117
West Coast	—	2
West Texas	117	491
Western Cities	—	—

[a] Tcf = trillion cubic feet

Unproved reserves are tabulated based on the shale play in which they exist. These plays do not necessarily line up neatly with the regions identified in this report. To come up with a region-level assessment of natural gas that could be available for DACS, we assigned the natural-gas reserves in a play to a region based on geographic overlap. This was not a rigorous analysis, and different assignments would result in a different distribution of natural gas reserves amongst the regions. We elected not to perform this analysis at the county level by dividing the plays over given counties because this would introduce artificial boundaries based on the land area, rather than the subsurface geology. Regardless, the calculated total amount of natural-gas reserves, approximately 2700 trillion cubic feet, would remain the same.

Next, we estimated the amount of natural gas that would continue to be consumed for non-DACS purposes through 2100. We assumed that the rate of natural-gas usage would decline following an exponential decay, starting from the 2022 value of 32.3 trillion cubic feet [37]. The decay rate constant was calculated based on the estimate presented in Denholm, *et al.* for natural gas consumption in 2035 [11], resulting in a decline in natural-gas usage of approximately 4.1%/year. This decay rate results in significant continued natural gas use at mid-century, approximately a third of usage today, and continued use through the end of the century. Integrating this usage through 2100 results in approximately 750 trillion cubic feet of natural gas, or 28% of reserves, that would be consumed for non-DACS purposes. We applied this consumption across all regions proportional to their reserves.

The remaining US domestic natural-gas reserves were used to calculate the quantity of CO_2 that could be removed via liquid solvent DACS (Figure 7-14). To convert the quantity into an annual rate, we assumed that liquid solvent DACS would operate for 50 years. As noted in the main text of the report, this comes out to over 4 billion tonnes per year of CO_2 removal.

We note that this is a highly simplified analysis that depends on many assumptions regarding natural-gas recovery, continued natural-gas use, and natural-gas consumption for DACS. Some unproven natural-gas reserves may be prohibitively expensive to recover, reducing the maximum estimate for DACS capacity. Similarly, significant continued usage of natural gas for industrial or other domestic uses would reduce the amount of natural gas available for DACS. Conversely, new technologies or more rapid decarbonization would lead to increasing the natural-gas reserves available for DACS, if we decide as a society to use these resources for CO_2 removal.

Using Flared Natural Gas for DACS

Natural gas flaring is the process of natural gas combustion using a dedicated flame at the wellhead and has become a more common practice over the past two decades for the safe development of unconventional oil and gas. For example, for tight oil production, the associated gas produced in the first two years is usually flared because of the relatively lower value compared to oil and because of the limited capacity for gas transportation [38]. The associated gas may still continue to be flared after the production well is connected to pipelines, when the amount of gas exceeds the capability of the gas gathering system. In the United States, the flared gas emissions are concentrated in the upstream of the natural gas supply (e.g., the Bakken basin, the Eagle Ford basin, and the Barnett basin) (Figure A7-9). The North Slope of Alaska is a potential hotspot for future sites that will flare natural gas due to its tight oil production potential. In total, the annual flared gas in the United States is around 10–15 billion cubic meters (on the order of 10^8 GJ).

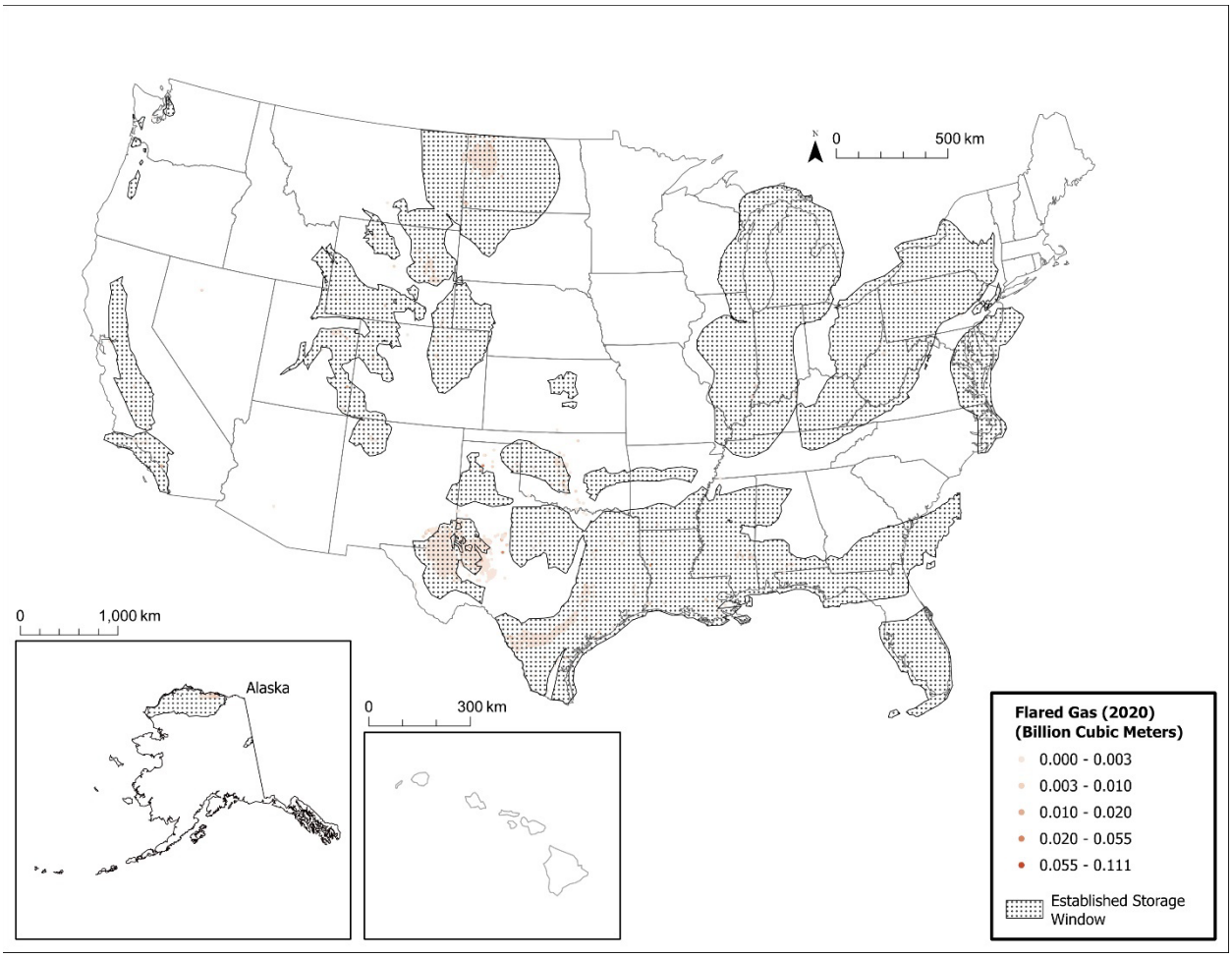

Figure A7-9. Spatial distribution of flared natural gas in the United States in 2020 with respect to established geologic storage areas.

Natural gas flaring is a waste of energy and contributes to climate change. Therefore, utilizing this natural gas, rather than flaring it, is listed as one of the research and development efforts in the DOE's "Stranded Natural Gas Roadmap" [39] and a variety of usage technologies have been proposed [40]. These technologies include compressing natural gas and trucking, extracting natural gas liquids, gas-to-methanol or gas-to-liquids conversion plants, and natural gas to electric power. Other proposed uses for flared gas include distributed generation [41], a combination of cryptocurrency mining and CO_2 capture [42], and water treatment [43].

Among the utilization options, compressing natural gas and trucking is a proven and flexible technology that could potentially be combined with DAC. In compressing natural gas and trucking, natural gas is first compressed to <1% of its volume and loaded into compressed natural gas trucks. During the compression process, valuable heavier components (e.g., natural gas liquids) can be collected. The compressed gas can then be trucked to DAC facilities for usage. However, there are a few concerns for building such a system. First, the cost benefits of compressing and trucking natural gas for powering DACS facilities needs to be justified. Existing techno-economic analysis has pointed out that the pay-back time is 1–1.5 years when trucking the natural gas to gas processing stations. As a result, building DACS near natural gas pipelines or gas processing stations and trucking the compressed gas to gas processing facilities may be more profitable. Second, the trucking system has limited scalability. The amount and time period of gas that

can be used is limited in a small-scale system. Third, flared gas is not a steady source. The amount of associated gas declines by 50–60% in the first year and has high variability. Meanwhile, DACS facilities are not likely to be mobile and have longer lifetime. If a DACS facility is designed for 30 years, natural gas from pipelines may be needed. However, if fully utilized for powering DAC facilities, the flared gas could potentially help remove 27–93 million tonnes of CO_2 annually.

Alternative Low-Carbon Heat Sources

Conventional Hydrothermal

Geothermal brine can commonly be found at temperatures exceeding 70°C, making it suitable for upgrading of process steam used for regeneration, reducing the electricity requirement of the heat pump used in the process. The cost of adsorbent DACS utilizing hydrothermal resources was modelled using a heat pump with an increased coefficient of performance compared to the modeling described in the main narrative of the report. Heat from the hydrothermal resource, with an assumed re-injection temperature of 70°C, was upgraded using a heat pump to produce steam. A minimum heat source temperature of 70°C increased the estimated heat pump coefficient of performance to approximately 4.

DACS capacity utilizing heat from hydrothermal sources, calculated in tonnes per year, was calculated using the following equations:

$$Capacity_{hydrothermal\ DAC} = \frac{Q_{steam}}{\left(E_{steam}/t_{CO_2}\right)}$$

$$Q_{steam} = Q_{hydrothermal} \times \frac{COP_{HP}}{COP_{HP} - 1}$$

$$COP_{HP} = \frac{Q_{steam}}{W_{in}} = \frac{Q_{hydrothermal} + W_{in}}{W_{in}} = 4$$

where Q_{steam} is the quantity of steam thermal energy produced by the hydrothermal-source heat pump (GJ/year), E_{steam}/t_{CO2} is the steam thermal energy required by the adsorbent DAC process (GJ/t_{CO2}), $Q_{hydrothermal}$ is the energy available as heat in the hydrothermal resource (assuming a re-injection temperature of 70°C) (GJ/year) determined by the resource temperature and flow rate, and W_{in} is the heat pump work input, as electrical energy (GJ/year).

Resource temperatures and flow rates were sourced from the NREL Geothermal Prospector [44,45] and only included resources that possessed both fluid flow information and with temperatures equal to or above 70°C. Duplicates were removed by cross-referencing latitude, longitude, flowrate, and temperature. Utilization of waste geothermal heat from geothermal power plants was not included in this analysis.

Overall cost of adsorbent DAC was then calculated for a plant scale determined by the availability of thermal energy for each hydrothermal resource and a levelized cost of hydrothermal heat, determined using the System Advisory Model [46]. This levelized cost of heat only accounted for capital and operating costs from drilling and pumping of the geothermal brine and did not include costs related to electricity generation (heat exchangers, turbines, etc.). The levelized cost of geothermal heat was found to depend strongly on resource temperature. The cost model assumptions were otherwise in line with the assumptions used in the 2050 adsorbent DACS cost analysis: state-level electricity pricing, renewable grid electricity, and full-scale (500 million tonnes per year deployed) learning. The cost of DAC does not include the cost of CO_2 storage or transport, which may be important because geothermal resources do not frequently overlap with geologic storage (**Figure A7-10**).

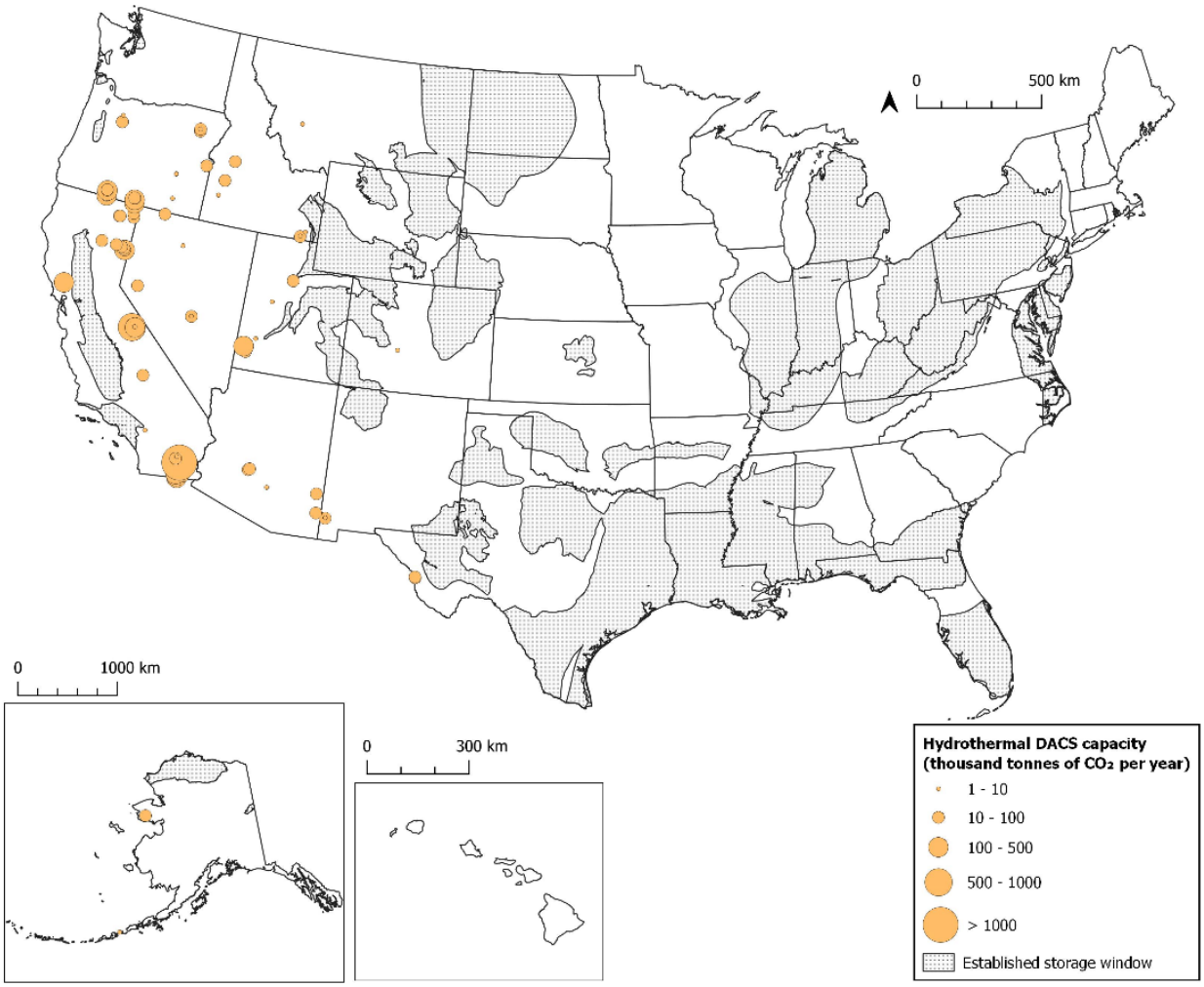

Figure A7-10. DACS potential utilizing conventional hydrothermal resources in the United States.

Enhanced Geothermal

Deep enhanced geothermal systems (EGS), human-made reservoirs at >4 km depth that enable thermal energy extraction from the earth for electricity generation or heating, have massive potential for low-carbon energy production. Compared to other forms of geothermal energy—conventional hydrothermal, unidentified hydrothermal, and enhanced geothermal with depth less than 4 km (i.e., near-field EGS), deep enhanced geothermal systems have a more than 2 order-of-magnitude increased potential. However, EGS is still a technology under development. The DOE Enhanced Geothermal Shot aims to reduce the cost of EGS by 90% to $45/MWh by 2035 [47].

There are two methods used for estimating the EGS potential. The *Future of Geothermal Energy* study assumes that the average reservoir temperature decline is 10°C, which leads to a fixed amount of recoverable heat in the reservoir per unit rock volume regardless of the resource temperature [48]. The second approach, developed by the USGS, assumes the recoverable heat in the reservoir is related to a reference temperature so that the recoverable heat is dependent on the reservoir temperature [49]. The first approach is used here for simplicity. Assuming a reservoir dimension 1 km in depth, the geothermal potential can be calculated as the product of recoverable heat and the area of suitable land. The recoverable heat in the reservoir based on the model is 5.12×10^{12} MJ/km^2, with a recovery factor of 20%,

as used in previous studies [50,51], the heat for DAC is dependent on the efficiency of the system, η_{DAC}. For electricity generation, the overall efficiency can be calculated as:

$$\eta_e = \dot{m}_s \times \Delta h \times \eta_t \times \eta_g \times \eta_{ncg} \times \eta_{apc} \times \eta_{pipe}$$

where m_s is the steam flow rate in the turbine, Δh is the enthalpy difference between the facility inlet and outlet, and η_t, η_g, η_{ncg}, η_{apc}, η_{pipe} are turbine efficiency, generation efficiency, efficiency decrease due to non-condensable gases content in the geothermal fluids, efficiency due to auxiliary power consumption, and heat loss due to the pipe system. Because the majority of the energy requirement for adsorbent DACS is thermal, we calculate the efficiency for the EGS-powered DACS system removing the turbine and generation efficiencies:

$$\eta_{DAC} = \frac{\eta_e}{\eta_t \times \eta_g}$$

Similar to the DACS facilities discussed in the main report, we assumed EGS-powered DACS facilities would be co-located with geologic storage, which constrained the available land area for enhanced geothermal. The total heat supply potential can be calculated as:

$$E_{th} = A_t \times \eta_{DAC} \times Q_{th}$$

where A_t is the land available at temperature range t and Q_{th} is the recoverable thermal energy in MJ_{th}/km^2. We assume the land suitability for geothermal recovery is similar to the wind power development and quantified the area in each temperature range based on 3000-meter depth estimated from the geothermal prospector. For any location that has a temperature less than 150°C, we estimated the required depth with a temperature gradient of 25°C/km. The land and enhanced geothermal heat for DACS is shown in **Table A7-11**.

Table A7-11. The potential of enhanced geothermal as a heat supply source for DAC.

Depth (*km*)	Available land (km^2)	Heat supply potential (*MJ*)
≤3	18,200	1.20×10^{16}
4	192,000	1.27×10^{17}
5	147,000	9.74×10^{16}
6	9,470	6.27×10^{15}

Solar Thermal

Concentrated solar thermal processes collect sunlight to heat a fluid to temperatures from 80°C to above 550°C, depending on the choice of the heat transfer fluid [52]. Typically, these processes are used to produce electricity, but the heat can potentially be used to power DACS facilities instead. The heat generation potential of solar thermal processes can be calculated taking into account the land availability, power density, capacity factor, and the number of hours of sunlight each year.

We first explored the relationship between heat sink power and the levelized cost of heat (LCOH) using the parametric function in the System Advisor Model (SAM) [46], varying the heat sink power from 1.39 to 30 MW_{th}. The heat sink power is the thermal input to the potential DAC facility and is proportional to the number of loops of the solar collectors (**Figure A7-11**). We set the loop inlet HTF temperature at 90°C and the loop outlet HTF temperature at 150°C. Other parameters are left as default if not specifically mentioned.

The results show the levelized cost increases slightly as the heat sink power increases until the heat sink power reaches 5.56 MW_{th} and remains relatively steady heat afterwards. As the overall variation is

relatively small, we chose 8 loops as a representative solar thermal system for the DACS analysis; this represents a worst-case scenario as the levelized cost is the highest. For a solar industrial process heat system with 8 loops, the direct land use is 127,000 m^2. The power density of the heat sink is then calculated as 43.7 MW_{th}/km^2. It should be noted that the power density represents only the thermal energy that could be potentially used by the DACS facilities, so it does not account for the entire technical potential. As a result, the power density we obtained is smaller than the commonly used 139.3 MW_{th}/km^2 in other studies [52,53].

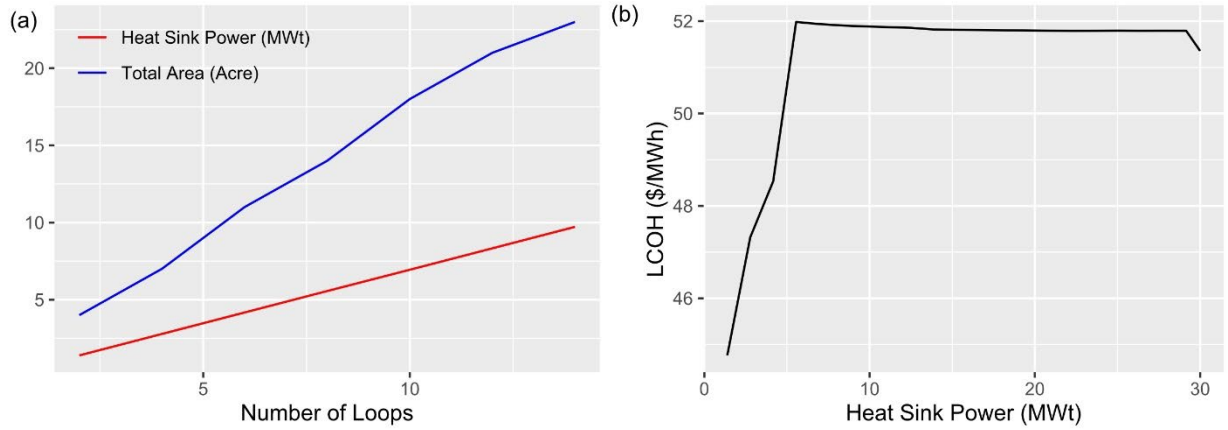

Figure A7-11. (a) The heat sink power and the total land use of a solar thermal industrial heat process facility is proportional to the number of loops in the solar field. (b) Trend of levelized cost of heat to the heat sink power.

The LCOH and CF of solar thermal industrial process heat facilities are related to the solar direct normal irradiation (DNI). We examined these relationships using the Industrial Process Heat-Trough model in the SAM. This model includes configurations of facilities with both solar collectors and thermal storage. The LCOH and CF are dependent on local weather, temperature, and elevation. Therefore, we performed case studies for several cities to examine the relationship between DNI and LCOH or CF (Table A7-12). Generally, the results show that the LCOH decreases and the CF increases as the DNI increases, but local weather conditions also impact, leading to scatter in the data (Figure A7-12).

Table A7-12. Case studies of levelized cost of heat and capacity factor of solar industrial heat process system.

City	Direct normal irradiation (*kWh/m²/day*)	Levelized cost (*$/MWh-thermal*)	Capacity factor
Fargo, ND	4.12	69.9	28.1
Helena, MT	4.2	51.2	38.6
Des Moines, IA	4.36	62.6	31.5
New Orleans, LA	5.04	50.5	39.1
Austin, TX	5.09	49.8	39.7
San Antonio, TX	5.3	48.3	40.9
Dallas, TX	5.38	48.6	40.8
Idaho Falls, ID	5.54	53.6	36.8
Cape Coral, FL	5.55	44.7	44.3
Wright, WY	5.77	52.0	38.0

City	Direct normal irradiation (*kWh/m²/day*)	Levelized cost (*$/MWh-thermal*)	Capacity factor
Ogden, UT	5.79	50.6	39.1
Lubbock, TX	5.95	40.4	49.2
Denver, CO	6.11	47.7	41.5
Sacramento, CA	6.66	43.4	45.7
Reno, NV	6.9	43.5	45.6
Santa Fe, NM	7.19	41.4	48.0
Los Lunas, NM	7.32	40.0	49.8
Tucson, AZ	7.36	38.4	51.9
Phoenix, AZ	7.41	38.0	52.5
Imperial, CA	7.61	37.3	53.5
Daggett, CA	7.67	38.1	52.8
Blythe, CA	7.93	36.8	54.2

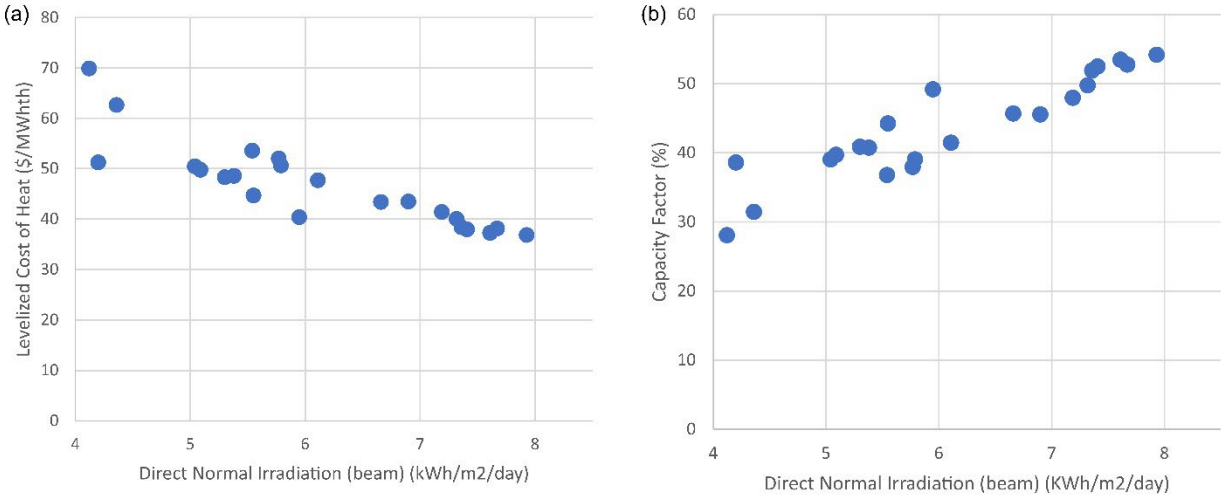

Figure A7-12. The levelized cost of heat (a) and the capacity factor (b) of a solar industrial heat process system is dependent on the direct normal irradiation.

We derived worst-case scenario relationships between DNI and the LCOH and CF. Using the above analysis, the technical potential ($E_{th,i,j}$) of a solar thermal industrial process heat system was then calculated at the grid points (j) defined in our main analysis:

$$LCOH = \begin{matrix} -0.869 \times DNI + 10.569 & DNI < 7.93 \\ 3.68 & DNI \geq 7.93 \end{matrix}$$

$$CF = \begin{matrix} 6.85 \times DNI - 0.124 & DNI < 7.93 \\ 54.2 & DNI \geq 7.93 \end{matrix}$$

$$E_{th,i,j} = A_{i,j} \times PD_j \times CF_i \times 8760$$

where $A_{i,j}$ is the suitable land area for the solar thermal technology j at grid point i, PD_j is the power density defined above, and CF is the CF at grid point i based on the relationship with DNI. We assume that

the solar thermal industrial heat process has similar land suitability restrictions as utility-scale solar photovoltaic, though it needs to be acknowledged that there is a small slope difference in the suitable land criteria that will change the actual available land (5% for utility-scale solar photovoltaic but 3% for concentrated solar power). By integrating the DNI map from the NREL National Solar Radiation Database (NSRDB) [54] and the identified geologic storage regions, we obtained maps of the technical potential and cost for solar thermal heat suitable for DACS (**Figure A7-13**).

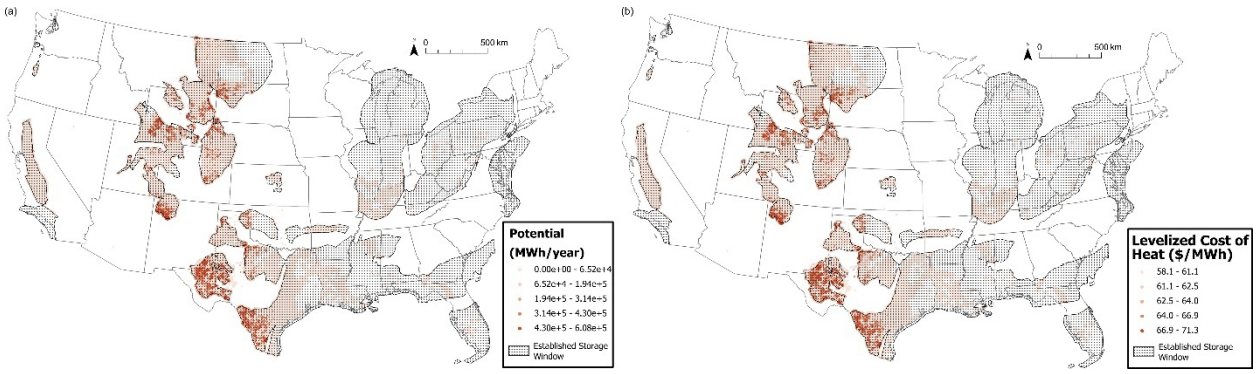

***Figure A7-13**. (a) The annual potential of heat from the solar industrial heat process system. (b) The levelized cost of heat of the solar industrial heat process system above identified storage areas.*

Ammonia Emissions from Adsorbent DACS

When amine-based DAC adsorbents degrade, they can release ammonia (NH_3) and possibly other volatile compounds. We calculated possible NH_3 emissions from amine-based solid adsorbent DACS based on a 1 million tonne per year facility, which would require approximately 1100 metric tonnes of adsorbent, based on a capacity of 35 kilograms of CO_2 per tonne of adsorbent per cycle and a cycle time of 20 minutes. Assuming 40% of the adsorbent's mass is branched poly(ethylenimine) with a molecular weight of 800 grams per mole, a 1 million tonne per year capture facility would contain 550 moles of polymer.

Based on a study by Racicot, *et al.* [55], the quantity of NH_3 released after 30% oxidation (see cost model parameters, Table A7-5) would be 0.065 moles of per mole of polymer, resulting in ~0.61 tonnes being released over the course of oxidation. Husk and Wenz [56] estimate that current adsorbent DAC captures between 50–65% of the CO_2 from the air it processes, requiring 2.5 trillion cubic meters of air for a 1 million tonne per year facility.

If we assume that oxidation occurs over the span of 6 months, and a worst-case capture fraction of 65%, the concentration of NH_3 in the post-process air would increase by approximately 0.8 parts per billion. However, the amount released depends on several factors: oxidation rate, which in turn depends on regeneration conditions and local environmental factors; allowable oxidation extent, assumed to be 30% in this case; replacement rate, i.e., how often the adsorbent needs to be replaced; capture fraction; and size of DACS facility. Future study is needed to better quantify the volatile compounds that may be released from a DACS facility and their time evolution profile over the course of facility operation.

References

[1] National Renewable Energy Laboratory (NREL), *2023 Annual Technology Baseline*. https://atb.nrel.gov/electricity/2023/index (accessed 2023-11-04).

[2] Jon Dewitz and U.S. Geological Survey, National Land Cover Database (NLCD) 2019 Products (Ver. 2.0, June 2021): U.S. Geological Survey Data Release, 2021. https://doi.org/10.5066/P9KZCM54.

[3] U.S. Geological Survey (USGS) Gap Analysis Project (GAP), Protected Areas Database of the United States (PAD-US) 3.0 (Ver. 2.0, March 2023): U.S. Geological Survey Data Release, 2022. https://doi.org/10.5066/P9Q9LQ4B.

[4] *National Conservation Easement Database | NCED*. https://www.conservationeasement.us/ (accessed 2023-11-04).

[5] Bureau of Land Management, *Areas of Critical Environmental Concern*. https://www.blm.gov/programs/planning-and-nepa/planning-101/special-planning-designations/acec (accessed 2023-11-04).

[6] USDA Forest Service, *USDA Forest Service FSGeodata Clearinghouse - Download National Datasets*. https://data.fs.usda.gov/geodata/edw/datasets.php (accessed 2023-11-04).

[7] U.S. Department of Homeland Security, *Homeland Infrastructure Foundation-Level Data (HIFLD)*. https://hifld-geoplatform.opendata.arcgis.com/ (accessed 2023-11-04).

[8] *Power Plants*. https://atlas.eia.gov/maps/power-plants (accessed 2023-11-05).

[9] Microsoft/USBuildingFootprints, 2023. https://github.com/microsoft/USBuildingFootprints (accessed 2023-11-04).

[10] Joseph T. Rand, *et al.*, A Continuously Updated, Geospatially Rectified Database of Utility-Scale Wind Turbines in the United States. *Scientific Data* 2020, *7* (1), 15. https://doi.org/10.1038/s41597-020-0353-6.

[11] Paul Denholm, *et al.*, *Examining Supply-Side Options to Achieve 100% Clean Electricity by 2035*; NREL/TP6A40-81644; National Renewable Energy Laboratory, 2022. https://www.nrel.gov/docs/fy22osti/81644.pdf.

[12] A. Jarvis, *et al.*, *Hole-filled SRTM for the globe : version 4 : data grid*. https://srtm.csi.cgiar.org/ (accessed 2023-11-07).

[13] Olufemi A. Omitaomu, *et al.*, Adapting a GIS-Based Multicriteria Decision Analysis Approach for Evaluating New Power Generating Sites. *Applied Energy* 2012, *96*, 292–301. https://doi.org/10.1016/j.apenergy.2011.11.087.

[14] Anthony Lopez, *et al.*, Land Use and Turbine Technology Influences on Wind Potential in the United States. *Energy* 2021, *223*, 120044. https://doi.org/10.1016/j.energy.2021.120044.

[15] Emily Leslie, *et al.*, *Princeton's Net-Zero America Study Annex D: Solar and Wind Generation Transitions*; Princeton University, 2021.

[16] Waranyu Buakhao and Anongrit Kangrang, DEM Resolution Impact on the Estimation of the Physical Characteristics of Watersheds by Using SWAT. *Advances in Civil Engineering* 2016, *2016*, e8180158. https://doi.org/10.1155/2016/8180158.

[17] Mark Bolinger and Greta Bolinger, Land Requirements for Utility-Scale PV: An Empirical Update on Power and Energy Density. *IEEE Journal of Photovoltaics* 2022, *12* (2), 589–594. https://doi.org/10.1109/JPHOTOV.2021.3136805.

[18] Lee M. Miller and David W. Keith, Observation-Based Solar and Wind Power Capacity Factors and Power Densities. *Environmental Research Letters* 2018, *13* (10), 104008. https://doi.org/10.1088/1748-9326/aae102.

[19] Lee M. Miller and David W. Keith, Addendum: Observation-Based Solar and Wind Power Capacity Factors and Power Densities (2018 Environ. Res. Lett. 13 104008). *Environmental Research Letters* 2019, *14* (7), 079401. https://doi.org/10.1088/1748-9326/ab12a2.

[20] Dylan Harrison-Atlas, *et al.*, Dynamic Land Use Implications of Rapidly Expanding and Evolving Wind Power Deployment. *Environmental Research Letters* 2022, *17* (4), 044064. https://doi.org/10.1088/1748-9326/ac5f2c.

[21] National Renewable Energy Laboratory (NREL), *Wind Supply Curves*. https://www.nrel.gov/gis/wind-supply-curves.html (accessed 2023-11-04).

[22] National Renewable Energy Laboratory (NREL), *Solar Supply Curves*. https://www.nrel.gov/gis/solar-supply-curves.html (accessed 2023-11-04).

[23] Anthony Lopez, *et al.*, Impact of Siting Ordinances on Land Availability for Wind and Solar Development. *Nature Energy* 2023, *8* (9), 1034–1043. https://doi.org/10.1038/s41560-023-01319-3.

[24] Briana Mordick Schmidt, *et al.*, *Carbon Negative by 2030: CO2 Removal Options for an Early Corporate Buyer*; LLNL-TR-832071; Lawrence Livermore National Laboratory, 2022. https://www-gs.llnl.gov/content/assets/docs/energy/LLNL-MSFT-CarbonRemoval_Final_28Feb22.pdf.

[25] Aliakbar Heydari-Gorji and Abdelhamid Sayari, Thermal, Oxidative, and CO2-Induced Degradation of Supported Polyethylenimine Adsorbents. *Industrial & Engineering Chemistry Research* 2012, *51* (19), 6887–6894. https://doi.org/10.1021/ie3003446.

[26] Juliana S. A. Carneiro, *et al.*, Insights into the Oxidative Degradation Mechanism of Solid Amine Sorbents for CO2 Capture from Air: Roles of Atmospheric Water. *Angewandte Chemie International Edition* 2023, *135* (24), e202302887. https://doi.org/10.1002/anie.202302887.

[27] Sarah Deutz and André Bardow, Life-Cycle Assessment of an Industrial Direct Air Capture Process Based on Temperature–Vacuum Swing Adsorption. *Nature Energy* 2021, 1–11. https://doi.org/10.1038/s41560-020-00771-9.

[28] David W. Keith, *et al.*, A Process for Capturing CO2 from the Atmosphere. *Joule* 2018, *2* (8), 1573–1594. https://doi.org/10.1016/j.joule.2018.05.006.

[29] Oxy Low Carbon Ventures, *Stepping Up to Bring Emissions Down*; Investor Update; 2022.

[30] *gridMET*. Climatology Lab. https://www.climatologylab.org/gridmet.html (accessed 2023-11-04).

[31] Marwan Sendi, *et al.*, Geospatial Analysis of Regional Climate Impacts to Accelerate Cost-Efficient Direct Air Capture Deployment. *One Earth* 2022, *5* (10), 1153–1164. https://doi.org/10.1016/j.oneear.2022.09.003.

[32] Keju An, *et al.*, The Impact of Climate on Solvent-Based Direct Air Capture Systems. *Applied Energy* 2022, *325*, 119895. https://doi.org/10.1016/j.apenergy.2022.119895.

[33] NASA Earth Exchange Global Daily Downscaled Projections (NEX-GDDP-CMIP6), 2021. https://doi.org/10.7917/OFSG3345.

[34] U.S. Department of Defense, *UFC 3-701-01 DoD Facilities Pricing Guide, with Change 3 | WBDG - Whole Building Design Guide*. https://www.wbdg.org/ffc/dod/unified-facilities-criteria-ufc/ufc-3-701-01 (accessed 2023-11-04).

[35] U.S. Energy Information Administration, Assumptions to the Annual Energy Outlook 2023: Oil and Gas Supply Module. 2023.

[36] U.S. Energy Information Administration, Proved Reserves of Crude Oil and Natural Gas in the United States, Year-End 2021. 2021.

[37] U.S. Energy Information Administration, *Use of natural gas*. https://www.eia.gov/energyexplained/natural-gas/use-of-natural-gas.php (accessed 2023-11-04).

[38] Anders Pederstad, *et al.*, *Improving utilization of associated gas in US tight oil fields*. https://www.catf.us/wp-content/uploads/2015/04/CATF_Pub_PuttingOuttheFire.pdf (accessed 2023-11-04).

[39] National Energy Technology Laboratory (NETL), *Stranded Natural Gas Roadmap*; 2020. https://netl.doe.gov/sites/default/files/2020-12/Stranded-Natural-Gas-Roadmap-04142020.pdf.

[40] U.S. Department of Energy, *Flaring and Venting Reduction Research & Development Activities*; 2021. https://www.energy.gov/sites/default/files/2021-08/Flaring%20and%20Venting%20Report%20to%20Congress%20Report.pdf.

[41] Deepika Bishnoi, *et al.*, Utilizing Flared Gas for Distributed Generation: An Optimization Based Approach. *AIP Conference Proceedings* 2019, *2091* (1), 020007. https://doi.org/10.1063/1.5096498.

[42] Pavel Snytnikov and Dmitry Potemkin, Flare Gas Monetization and Greener Hydrogen Production via Combination with Cryptocurrency Mining and Carbon Dioxide Capture. *iScience* 2022, *25* (2). https://doi.org/10.1016/j.isci.2022.103769.

[43] Yael R. Glazer, *et al.*, Potential for Using Energy from Flared Gas for On-Site Hydraulic Fracturing Wastewater Treatment in Texas. *Environmental Science & Technology Letters* 2014, *1* (7), 300–304. https://doi.org/10.1021/ez500129a.

[44] Daniel Getman, *et al.*, *Geothermal Prospector: Supporting Geothermal Analysis Through Spatial Data Visualization and Querying Tools*; NREL/CP-6A20-66435; Davis, CA: Geothermal Resources Council, 2015. https://www.osti.gov/biblio/1253709 (accessed 2023-11-04).

[45] Geothermal Prospector. https://maps.nrel.gov/?da=geothermal-prospector (accessed 2023-11-04).

[46] Nate Blair, *et al.*, *System Advisor Model (SAM) General Description (Version 2017.9.5)*; NREL/TP-6A20-70414; 2018. https://doi.org/10.2172/1440404.

[47] *Enhanced Geothermal Shot*. Energy.gov. https://www.energy.gov/eere/geothermal/enhanced-geothermal-shot (accessed 2023-11-04).

[48] Jefferson W. Tester, *et al.*, *The Future of Geothermal Energy*; INL/EXT-06-11746; Idaho National Lab. (INL), Idaho Falls, ID (United States), 2006. https://doi.org/10.2172/911903.

[49] Colin F. Williams, *et al.*, *A Review of Methods Applied by the U.S. Geological Survey in the Assessment of Identified Geothermal Resources*; 2008–1296; U.S. Geological Survey, 2008. https://doi.org/10.3133/ofr20081296.

[50] S Petty and G. Porro, Updated U.S. Geothermal Supply Characterization; 2007.

[51] C. Augustine, *Updated U.S. Geothermal Supply Characterization and Representation for Market Penetration Model Input*; NREL/TP-6A20-47459; 2011. https://doi.org/10.2172/1027673.

[52] Parthiv Kurup and Craig Turchi, *Initial Investigation into the Potential of CSP Industrial Process Heat for the Southwest United States*; NREL/TP-6A20-64709; 2015. https://doi.org/10.2172/1227710.

[53] Parthiv Kurup, *et al.*, *Initial Thermal Energy Yield Potential for the Use of Concentrating Solar Power (CSP) for Coal Hybridization in India*; NREL/TP-6A20-74024; 2019. https://doi.org/10.2172/1560125.

[54] *NSRDB: National Solar Radiation Database*. https://nsrdb.nrel.gov/ (accessed 2021-11-10).

[55] Joan Racicot, *et al.*, Volatile Products of the Autoxidation of Poly(Ethylenimine) in CO2 Sorbents. *The Journal of Physical Chemistry C* 2022, *126* (20), 8807–8816. https://doi.org/10.1021/acs.jpcc.1c09949.

[56] Jason C. Husk and Graham B. Wenz, Inside-Out: Driving Down Direct Air Capture Costs With High-Efficiency Adsorbents. *Frontiers in Climate* 2022, *3*.

APPENDIX—Chapter 8

Land Suitability Analysis for BiCRS and DAC

The goal of the land suitability analysis is to identify the potential areas that fit the physical and regulatory requirements for development using geospatial analysis. We conducted land suitability analysis for the siting of **biomass carbon removal and storage** (BiCRS) facilities and renewable energy facilities (i.e., land-based wind and utility-scale PV). Direct air capture (DAC) facilities are assumed to be co-located with and powered by these wind and solar facilities. Other types of renewables are not taken into consideration because they are projected to be more expensive than land-based wind and utility-scale PV, according to the Annual Technology Baseline 2022 [1], and land is usually not a main constraint for the development of other types of renewables (e.g., geothermal).

The land suitability analysis starts with applying general siting criteria on the 30-meter resolution 2019 National Land Cover Database (NLCD) [2]. Technological-specified criteria were then applied separately for the renewables and BiCRS facilities. The NLCD represents land use in the Contiguous United States (CONUS) in 2019, which classifies the land cover of the CONUS into 16 classes, including open water, perennial ice/snow, developed (4 sub-classes), barren land, forest (3 subclasses), shrub/scrub, grassland/herbaceous, pasture/hay, cultivated crops, and wetlands (2 subclasses). The NLCD layer additionally serves as a reference layer of cell size (i.e., resolution), spatial reference and projection, spatial processing extent as well as a snap raster for any following geospatial analysis when applicable.

Conditions for land suitability are applied in two steps. First, the general criteria, which includes five conditions, were applied in sequence (from the most critical to less critical) to identify the impact of each of the conditions (**Table A8-1**). The general criteria can be categorized into three groups: current land cover (developed land, open water, and wetland), regulatory (e.g., the land identified as of critical environmental concern), and existing infrastructure (e.g., airports, railroads, buildings, and existing energy system infrastructure (power plants and transmission lines).

Table A8-1. General suitability conditions applied on land suitability analysis of wind, solar, and BiCRS.

Step	Condition	Data Source	Notes	Data Source
0	NLCD	NLCD	Class water excluded	Dewitz and U.S. Geological Survey (2021) [2]
1	Protected land	PAD-US 3.0	Buffer distance = 3 km if GAP-status = 1 or 2 (e.g., national parks)* Buffer distance = 0 if GAP-status = 3 or 4 (e.g., state parks)	U.S. Geological Survey (USGS) Gap Analysis Project (GAP) (2022) [3]
		NCED	Buffer distance = 3 km for GAP-status = 1 or 2 (e.g., national parks) Buffer distance = 0 for GAP-status = 3 or 4 (e.g., state parks)	National Conservation Easement Database [4]
		ACEC	Buffer distance = 3 km in designed area	Bureau of Land Management [5]

		Roadless area	Buffer distance = 3 km	USDA-Forest Service [6]
2	Wetlands	Wetlands in NLCD 2019	Buffer distance = 0.3 km	Dewitz and U.S. Geological Survey (2021) [2]
3	Developed	Developed in NLCD 2019	Buffer distance = 0	Dewitz and U.S. Geological Survey (2021) [2]
4	Other developed	Airports	Buffer distance = 3 km	Homeland Infrastructure Foundation-Level Data [7]
		Railroad	Buffer distance = 0.015 km	Homeland Infrastructure Foundation-Level Data [7]
		Transmission Line	Buffer distance based on voltage	Homeland Infrastructure Foundation-Level Data [7]
		Power Plants	Buffer distance = 3 km	U.S. Energy Information Administration [8]
		Building Envelop	Buffer distance = 0.3 km	Microsoft (2018) [9]
		Wind Turbines	Buffer = 3 km	Rand et al. (2020) [10]

*GAP = Gap Analysis Project

Second, technological-specified criteria were applied. For BiCRS facilities, the technological criteria are assumed to be similar to the thermal power plant requirements, as discussed in Omitaomu et al. [11] except the population density condition, which is assumed as an overlapping of the developed class and the other occupation class (typically, the buffer area of the building envelope). Table A8-2 summarizes the conditions and data sources. Starting from the landslide condition, the processes are performed at a 100-meter resolution.

Table A8-2. Technological-specified conditions applied in BiCRS land suitability analysis.

Step	Condition	Data source
BiCRS-1	Slope >12%	Calculated from elevation data
BiCRS-2	Landslide hazard	Omitaomu et al. (2012) [11]
BiCRS-3	100-year floodplain	Omitaomu et al. (2012) [11]
BiCRS-4	Cooling water of 473 m^3/min with 32 km	Omitaomu et al. (2012) [11]

For land-based wind power and utility-scale PV, the criteria are summarized in Table A8-3 and the workflow is shown in Figure A8-1(a). Notably, we excluded land that is projected to be occupied by wind/PV development for the grid decarbonization in the United States by 2050, and the grid

decarbonization data is obtained from the 100% clean energy study by Denholm et al. (2022) [12]. Denholm et al. (2022) projected future energy demand and supply in the United States with a baseline year of 2020. Denholm et al. obtained spatially explicit results for the expansion of the transmission lines and the clean energy facilities, which mainly include cheaper wind and solar energy among all the optional renewables. The land we excluded for wind and PV development in this report is from the "Moderate" progress and the "All Options" scenario as defined by National Renewable Energy Laboratory (NREL) 2050. The "All Options" scenario is the only scenario in NREL's study that treats direct air capture (DAC) as a mature technology by 2050, available to offset carbon emissions from power plants. Throughout the report, we treat grid decarbonization as a top priority, allowing for DAC co-located with renewables only on land that is not required for decarbonization.

Table A8-3 Technological-specified conditions applied in land suitability analysis of land-based wind and utility-scale PV.

Step	Condition	Data Source
Wind-1	Slope <20% (11.31°)	Jarvis et al. (2008) [13]
Wind-2	Out of prioritized renewable energy area	Denholm et al. (2022) [12]
Wind-3	>5 km^2 contiguous area	Calculated
PV-1	Slope <5% (2.86°)	Jarvis et al. (2008) [13]
PV-2	Out of prioritized renewable energy area	Denholm et al. (2022) [12]
PV-3	5 km^2 contiguous area	Calculated

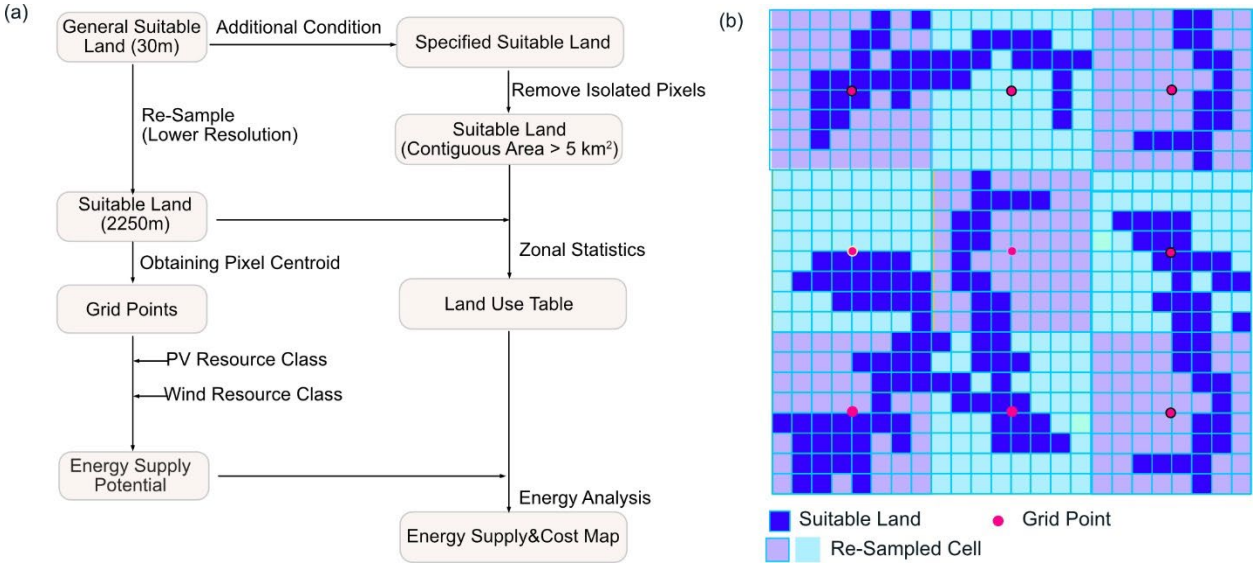

Figure A8-1. (a) The workflow of grid-level analysis (b) The resampling process keeps the information of the suitable land in the grid points

In the next step, we calculated the electricity generation potential of wind and PV using the 30-meter resolution map of suitable land from the previous steps. To determine the generation potential, spatially explicit data of the area of suitable land and the resource class of wind and solar irradiation are needed.

This step is conducted at a grid-point level. The grid points are obtained by first resampling the 30-meter resolution map to a 2250-meter resolution map, and the centroids of each pixel in the resampled map were then identified as grid points, as shown in **Figure A8-1(b)**. The resampled map has also been used for calculating the area of available land in the original map by counting the number of pixels of suitable land that is overlapped by each pixel in the resampled map. In the resampled map, each pixel represents ~5 km^2. After this aggregation process, the values of the area of suitable land were transferred to each grid point as their original resolution, although the continuity information was lost. The resolution of the grid-level analysis (i.e., how many 30-meter resolution pixels are merged together) will impact the maximum suitable land per grid and thus the upper limit of energy generation for each grid point. The overall generation potential could also be impacted due to the spatial variations of the corresponding generation capacity parameters (e.g., energy resources such as wind speed and solar irradiation). We obtained energy resource class parameters based on the grid points. The resource classes are determined by the 120-meter height wind speed for wind power and the global horizontal irradiation for utility-scale PV. These parameters are obtained by spatial-join grid points with the NREL wind supply curves [14] and solar supply curves [15]

We included all the suitable land that is of class barren, forest, shrub/scrub, grassland/herbaceous, pasture/hay, and cultivated crops, and then applied a "contiguous" condition, considering the renewable energy facilities could potentially be co-located in these areas. The contiguous condition excludes any connected pixels that form an area less than 5 km^2. We then excluded areas where forests account for >25% of wind energy suitable land or where forests, pasture/hay or cultivated crops occupy >25% of suitable land for utility-scale PV. Finally, the energy option for a typical location is selected based on the energy potential. The sensitivity analysis based on co-location condition (i.e., the fraction of suitable land) shows that varying the fraction of 5% (strict constraint) to 100% (no constraint) impacts the availability of land by about 1 order of magnitude for both wind and solar. Overall, our results show a more conservation estimation of suitable land. For example, compared to the NREL supply curves in a reference scenario (**Figure A8-2**), the total suitable land in our analysis is ~1/23 and 1/32 for wind energy and solar PV, respectively, when a 25% co-location condition was applied, and is ~1/4 and ~1/6, respectively, when a 100% co-location was applied, although it should be noted that we have removed the areas occupied by the prioritized renewables for grid decarbonization. The other differences are mainly from the contiguous condition, as illustrated in Chapter 8, main document which requires a contiguous land larger than 5 km^2.

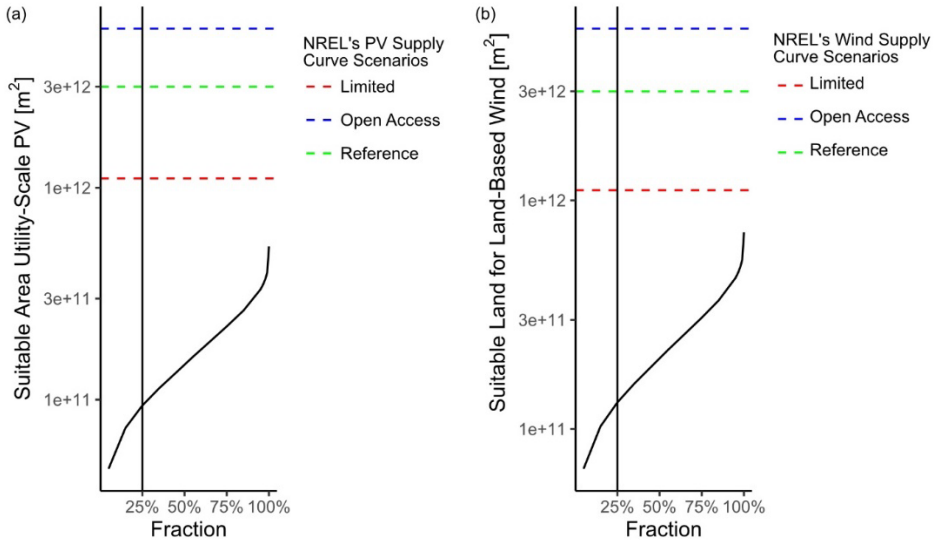

Figure A8-2. Sensitivity analysis of the impact of the fraction of co-location limit to the total area of suitable land (a) PV co-location with forests, pasture/hay or cultivated crops (b) Wind co-location with forests.

We assumed that land that is suitable for wind energy development is suitable for DAC facilities. In this way, we assumed DAC facilities have similar properties to wind energy (e.g., tower height and noise level). Additionally, we assume that DAC plants have a higher siting flexibility compared to other carbon neutral technologies.

Our analyses are conducted at a 30-meter resolution when applicable, which is higher than previous studies. For example, Omitaomu et al. used 100-meter resolution for identifying thermal power generating sites [11]. Lopez et al. used 90-meter resolution for wind power siting [16]. Leslie et al. used 4-kilometer resolution for solar and wind energy siting [17]. A higher resolution led to several changes. First, without resampling to lower resolution, small clusters of pixels of land use classes remain in the dataset rather than integrated into the neighbor pixels. As a result, more pixels (or land) will be identified as unsuitable due to their current land cover. The results (i.e., the suitable land map after applying the exclusion conditions) show a higher level of fragmentation and discontinuity as shown in Figure A8-3, which is critical for the application of the continuity condition. Additionally, the slope calculated based on different resolutions can vary multiple times when using different resolutions of digital elevation models. For example, Buakhao and Kangrang show that, for the same area, the slope calculated at a 90 meters resolution is 10 percent lower than the slope calculated at a resolution of 30 meters [18]. Some criteria need to be processed at a resolution equal or higher than 30 meters to be effective in geospatial processing. These include thin road pixels in the NLCD 2019, railways, which are polylines and buffered for 15 meters, and the low voltage transmission lines. These conditions will disappear when using a lower resolution.

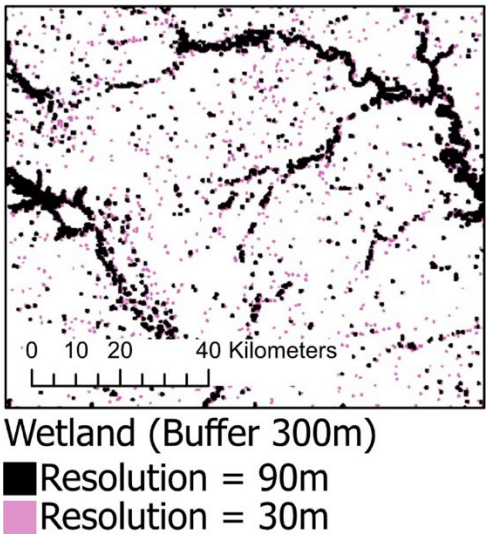

Figure A8-3. More areas are excluded when using a 30-meter resolution. Image shows pink pixels overlayed by black pixels).

Renewable Electricity Potential and Cost Analysis

The electricity generation potential analysis is conducted at a grid point level obtained from the previous step. For each grid point in the dataset, the electricity generation potential $E_{i,j}$ in MWh/year at grid point i with technology j (j = Wind/PV) can be calculated as:

$$E_{i,j} = C_{i,j} \cdot CF \cdot 8760$$

where $C_{i,j}$ is the installed capacity in MW that could be installed in the grid point i with technology j and is calculated as:

$$C_{i,j} = A_{i,j} \cdot PD_j$$

where $A_{i,j}$ is the area of suitable land in km^2 and PD_j is the power density of the technology in MW/km^2 for the technology j, which shows the nominal capacity can be built in a unit of suitable land; CF is the capacity factor indicating the fraction of a facility running at its nominal capacity in the time of the whole year or 8760 hours.

Power density is currently considered as constant across the United States. Temporarily, the power density for utility-scale PV has been increasing. Bolinger and Bolinger [19] conducted geospatial analysis for >90% of existing solar PV plants in the United States and found that the median power density has increased by 52% and by 43% for fixed-tilt plants and tracking plants, respectively, from 2011 to 2019. We used the median value, 45 W/m^2, from this study. The trend of power density of land-based wind energy remains unresolved. Earlier studies used ~3 W/m^2 and considered the power density of wind energy would decrease as companies are choosing turbines with lower specific power of wind turbines (i.e., the ratio of a wind turbine's rated capacity to its rotor swept area) [16], [20]. However, a recent large-scale study [21] has found that the median power density of wind energy is 4.3 W/m^2 but with substantial variation. We used this median value in our study as methodology on power density of wind energy still needs to be improved. Figure A8-4 shows the energy potential is proportional to the power density value being selected, and as solar PV has a power density that is ~1 order of magnitude higher than wind power and a larger varying interval, technological improvements in PV may introduce a large impact on the overall electricity generation potential.

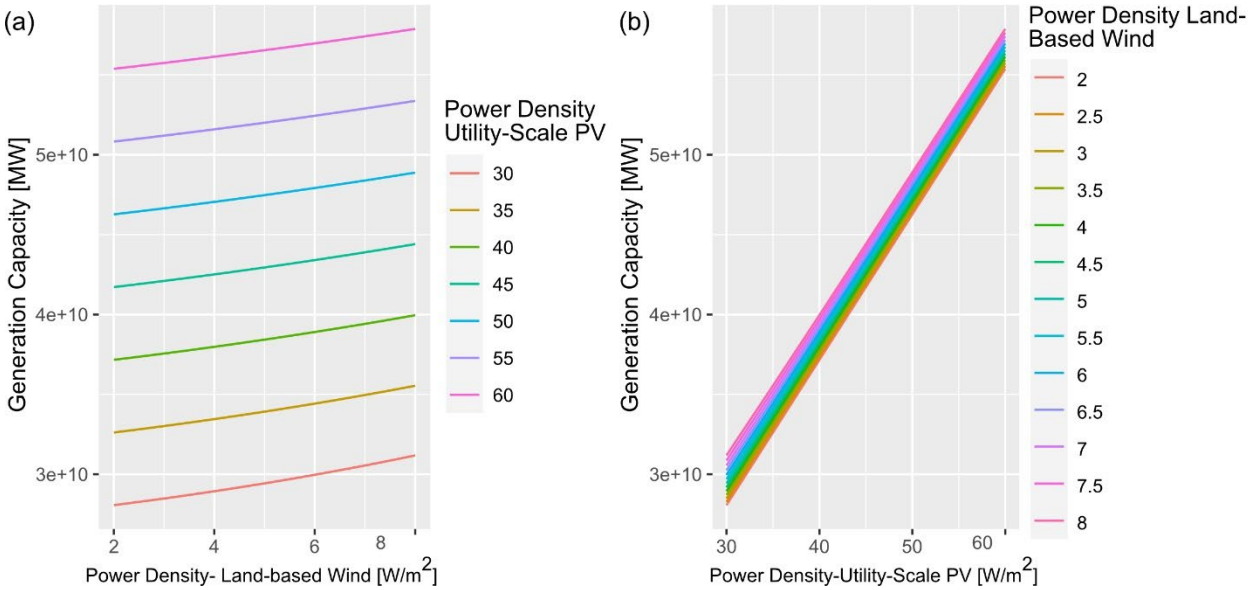

Figure A8-4. Results of sensitivity analysis of the impact of power density on the generational capacity of (a) utility-scale PV and (b) land-based wind.

We estimate the cost of electricity from wind and PV using the results of the levelized cost of energy (LCOE) analysis in the 2022 Electricity Annual Technology Baseline (Electricity ATB) [22]. The Electricity ATB estimates technology-specific cost and performance considering a variety of resource classes and research and development scenarios. The electricity ATB projects the cost from 2022 through 2050. The levelized cost of energy (LCOE) ($/MWh) in Electricity ATB is calculated as:

$$LCOE = ((CRF \cdot PFF \cdot CFF \cdot (OCC \cdot CRM + GCC) + FOM) \cdot 1000)/(CF * 8760) + VOM + FUEL$$

where CRF is the capital recovery factor; PFF is the project finance factor; CFF is the construction finance factor; OCC is the overnight capital cost; CRM is the capital regional multiplier; GCC is the grid connection costs; FOM is the fixed operating expenses ($/kW); VOM is the variable operating expenses in $/MWh; and $FUEL$is the fuel input in $/MWh.

Spatially explicit estimates of $LCOE$ are obtained based on the resource class of wind and solar. The land-based wind resource is divided into ten classes based on wind speed class and the utility-scale PV resource classes are determined based on the level of global horizontal irradiance (GHI) class. The costs per resource classes were then matched with the corresponding parameters obtained in the land suitability analysis.

For each grid point, we choose the technology with a higher generation potential. Compared to choosing technology based on a lower cost, the land requirement, the generation potential, and the median of cost are similar to the chosen higher generation potential scenario, as shown in Figure A8-5. This is because wind energy and solar PV has a similar projected cost in 2050, especially when the resource class is comparable, although the cost of wind energy is much higher (reaching >$40/MWh), as shown in Table A8-4 to Table A8-6. Wind power has a looser constraint on land use (e.g., slope and co-location limitations) but solar PV has almost an order of magnitude higher power density. As a result, lands that are only suitable for wind power development can have a low wind resource class, which leads to a higher third-quarter cost in the maximum potential scenario.

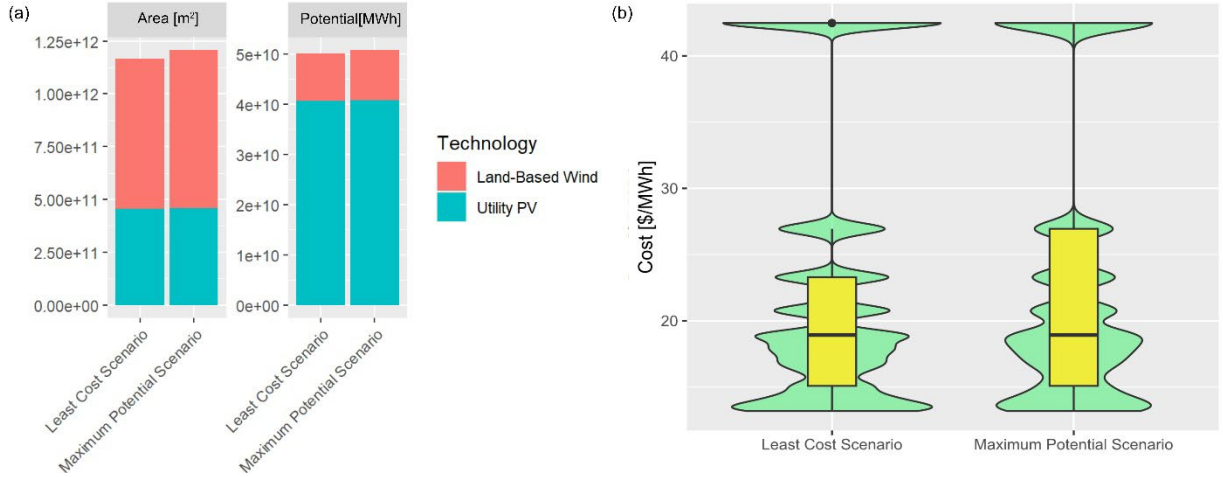

Figure A8-5. Results of scenario analysis of the impact of grid-level generation technology choice on land use, generation potential, and cost of electricity.

Table A8-4. Energy cost models from the ATB 2022.

Technology	Model	Scenario	Year
PV	Solar - utility PV	Moderate	2050

Wind	Land-based wind	Moderate	2050
Battery	Utility-scale battery storage – 4 Hr.	Moderate	2050

Table A8-5. Wind energy class and levelized cos.t

Type	Min. wind speed (m/s)	Max. wind speed (m/s)	LCOE ($/MWh)
Land-based wind - Class 1	9.01	12.89	15.4
Land-based wind - Class 2	8.77	9.01	16.6
Land-based wind - Class 3	8.57	8.77	17.0
Land-based wind - Class 4	8.35	8.57	17.5
Land-based wind - Class 5	8.07	8.35	18.0
Land-based wind - Class 6	7.62	8.07	18.9
Land-based wind - Class 7	7.10	7.62	20.8
Land-based wind - Class 8	6.53	7.10	23.3
Land-based wind - Class 9	5.90	6.53	27.9
Land-based wind - Class 10	1.72	5.90	42.5

Table A8-6. Solar energy class and levelized cost.

Type	Min. GHI (kWh/m^2/day)	Max. GHI (kWh/m^2/day)	LCOE ($/MWh)
Utility PV - Class 1	5.75		13.2
Utility PV - Class 2	5.50	5.75	13.6
Utility PV - Class 3	5.25	5.50	14.3
Utility PV - Class 4	5.00	5.25	15.1
Utility PV - Class 5	4.75	5.00	16.1
Utility PV - Class 6	4.50	4.75	16.8
Utility PV - Class 7	4.25	4.5	17.6

Utility PV - Class 8	4.00	4.25	18.5
Utility PV - Class 9	3.75	4.00	19.4
Utility PV - Class 10	0	3.75	21.2

Baseline Decarbonization Scenario

NREL conducted a study on the transition to a 100% clean energy system [23]. The study first determined two demand scenarios, the Reference-AEO, which represents the "current policy" electricity demand, and the Reference-ADE, which represents an accelerated electrification scenario and has a much higher load growth. NREL's study then evaluated four primary scenarios that achieve 100% clean electricity supply in 2035 and afterwards to meet such a demand. These scenarios include (1) All-Options, which assumes continuous improvement of electricity generation technologies and a development a deployment of DAC; (2) Infrastructure Renaissance, which allows greater levels of deployment of transmission; (3) Constrained, which limits the deployment of new generation capacity and transmission; and (4) No CCS, which assumes CCS technologies will not achieve a cost-competitive deployment status by the study's temporal scope. We use results in the year 2050 from the All-Options scenario as a baseline decarbonization scenario.

NREL's 100% clean electricity used NREL's wind supply curve and NREL's solar supply curve for the energy facility siting analysis. Our land suitability and renewable energy supply analysis (see first section above) applied similar constraints as the supply curves but with a noticeable difference. In NREL's supply curve, land cover types in suitable land are considered as suitable regardless of the land cover, which allows the co-location of solar with a land cover of forest, pasture/hay, or cultivated land. Our approach, on the other hand, first identified the fraction of each suitable land cover type (i.e., barren, forest, shrubland, herbaceous, pasture/hay, and cultivated crops) in each analysis grid. The co-location criteria were then applied, which excluded wind energy development to develop in areas with more than 25% of forest, and solar development in areas with more than 25% of forest, pasture/hay, or cultivated crops.

Water Impacts

To estimate the water resource impacts of large-scale carbon dioxide removal, we required data on future water shortages by region across the United States as well as the water consumption (evaporative losses and water incorporated into products) for each technology. Projected water shortage frequency by hydrologic basin for the years 2046 through 2070 based on 14 different climate scenarios is shown in Figure A8-6 and this was used in the report to identify regions where high water requirements coincide with frequent future water scarcity. Water consumption factors per tonne of CO_2 captured for BiCRS technologies are shown in Table A8-7.

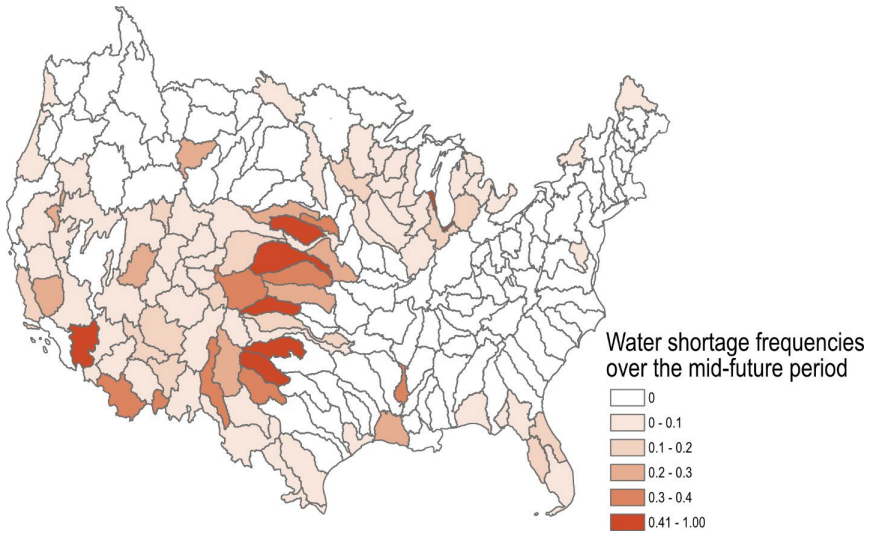

Figure A8-6. HUC-4 basins and water shortage frequency by basin (reproduced from Brown et al. (2019) [24]).

Table A8-7. Water consumption factors for different BiCRS configurations.

Configuration	Water consumption (tonne / tonne CO_2 captured)	Notes
Diesel and adipic acid	3.00	Calculated based mass/energy balances in Appendix 6
Diesel (no co-product)	2.42	Calculated based mass/energy balances in Appendix 6
Ethanol and adipic acid	3.09	Calculated based mass/energy balances in Appendix 6
Ethanol (no co-product)	2.48	Calculated based mass/energy balances in Appendix 6
Jet fuel and adipic acid	3.09	Calculated based mass/energy balances in Appendix 6
Jet fuel (no co-product)	2.48	Calculated based mass/energy balances in Appendix 6
Polyethylene and adipic acid	3.09	Calculated based mass/energy balances in Appendix 6
Polyethylene (no co-product)	2.48	Calculated based mass/energy balances in Appendix 6
Sawmill	negligible	Calculated based mass/energy balances in Appendix 6
Electricity	0.74	Calculated based mass/energy balances in Appendix 6
RNG	1.43	Calculated based mass/energy balances in Appendix 6
Biomass to H2, pyrolysis	1.85	Source: Cui et al. (2021) [25]
Biomass to H2, gasification	1.85	Same footprint as pyrolysis to H_2

Air Quality Impacts

To understand the potential air quality impacts associated with constructing new BiCRS facilities across the United States, we used the Maximum Potential scenario, optimized for carbon removal as a test case. Assuming, conservatively, thermal decomposition of solvents to ammonia and 90% capture rates of all other pollutants in the carbon capture solvent for post-combustion streams, we found that ammonia would dominate any potential negative air quality impact and would be primarily concentrated in the eastern half of the United Sates. Emissions were converted to changes in fine particulate matter concentration using InMAP (**Figure A8-7**). However, this ignores the net positive impacts on air quality that would result from large-scale decarbonization and uptake of carbon capture systems. On the whole, the combination of decarbonization and large-scale CO_2 removal should result in substantial reductions in air pollutant emissions. Future versions of integrated assessment models such as InMAP will require updates to account for the dramatic changes in background pollutant concentrations, which will impact their predictions of secondary $PM_{2.5}$ formation.

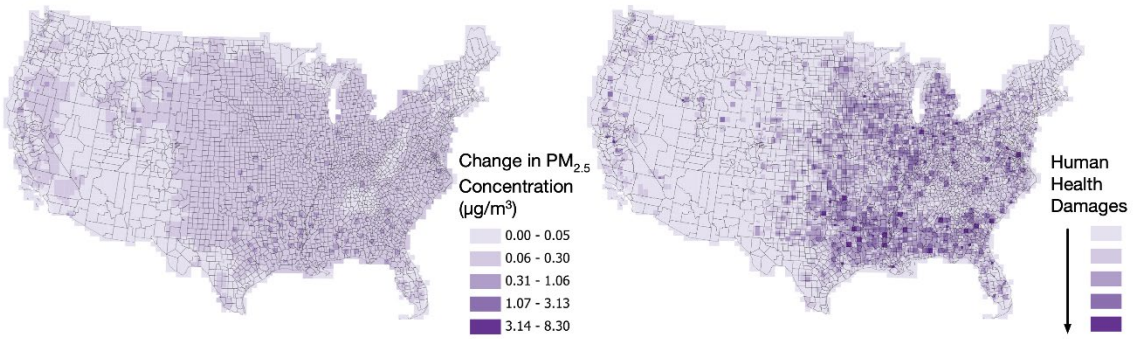

Figure A8-7. Impact of BiCRS facilities on fine particulate matter concentrations in the United States and monetized health damages if facilities operated in the context of current background pollutant concentrations and population distribution.

References

[1] U.S. Energy Information Administration, "Annual Energy Outlook 2022," 2021. https://www.eia.gov/outlooks/aeo/ (accessed Dec. 31, 2021).

[2] J. Dewitz and U.S. Geological Survey, "National Land Cover Database (NLCD) 2019 Products (ver. 2.0, June 2021): U.S. Geological Survey data release," 2021. .

[3] U.S. Geological Survey (USGS) Gap Analysis Project (GAP), "Protected Areas Database of the United States (PAD-US) 3.0: U.S. Geological Survey data release," 2022. .

[4] National Conservation Easement Database, "No Title." https://www.conservationeasement.us/.

[5] Bureau of Land Management, "Areas of Critical Environmental Concern," [Online]. Available: https://www.blm.gov/programs/planning-and-nepa/planning-101/special-planning-designations/acec.

[6] USDA-Forest Service, "https://data.fs.usda.gov/geodata/edw/datasets.php." https://data.fs.usda.gov/geodata/edw/datasets.php.

[7] Geospatial Management Office, "Homeland Infrastructure Foundation-Level Data." https://hifld-geoplatform.opendata.arcgis.com/.

[8] U.S. Energy Information Administration, "Layer Information for Interactive State Maps." https://www.eia.gov/maps/layer_info-m.php (accessed Nov. 03, 2022).

[9] Microsoft, “US Building Footprints,” 2018. https://github.com/microsoft/USBuildingFootprints.

[10] J. T. Rand *et al.*, “A continuously updated, geospatially rectified database of utility-scale wind turbines in the United States,” *Sci. Data*, vol. 7, no. 1, pp. 1–12, 2020, doi: 10.1038/s41597-020-0353-6.

[11] O. A. Omitaomu *et al.*, “Adapting a GIS-based multicriteria decision analysis approach for evaluating new power generating sites,” *Appl. Energy*, vol. 96, pp. 292–301, Aug. 2012, doi: 10.1016/J.APENERGY.2011.11.087.

[12] P. Denholm, P. Brown, W. Cole, T. Mai, and B. Serg, “Examining Supply-Side Options to Achieve 100 % Clean Electricity by 2035 Examining Supply-Side Options to Achieve 100 % Clean Electricity by 2035,” 2022.

[13] A. Jarvis, H. I. Reuter, A. Nelson, and E. Guevara, “Hole-filled SRTM for the globe Version 4,” *available from CGIAR-CSI SRTM 90m Database (http//srtm. csi. cgiar. org)*, vol. 15, no. 25–54, p. 5, 2008.

[14] National Renewable Energy Laboratory, “Wind Supply Curves.” https://www.nrel.gov/gis/wind-supply-curves.html.

[15] National Renewable Energy Laboratory, “Solar Supply Curves.” https://www.nrel.gov/gis/solar-supply-curves.html.

[16] A. Lopez, T. Mai, E. Lantz, D. Harrison-Atlas, T. Williams, and G. Maclaurin, “Land use and turbine technology influences on wind potential in the United States,” *Energy*, vol. 223, p. 120044, 2021, doi: 10.1016/j.energy.2021.120044.

[17] E. Leslie, A. Pascale, and J. D. Jenkins, “Princeton’s Net-Zero America Study Annex D: Solar and Wind Generation Transitions,” 2021, [Online]. Available: https://netzeroamerica.princeton.edu/img/NZA Annex D - Solar and wind generation.pdf.

[18] W. Buakhao and A. Kangrang, “DEM resolution impact on the estimation of the physical characteristics of watersheds by using SWAT,” *Adv. Civ. Eng.*, vol. 2016, 2016.

[19] M. Bolinger and G. Bolinger, “Land Requirements for Utility-Scale PV: An Empirical Update on Power and Energy Density,” *IEEE J. Photovoltaics*, vol. 12, no. 2, pp. 589–594, 2022, doi: 10.1109/JPHOTOV.2021.3136805.

[20] L. M. Miller and D. W. Keith, “Addendum: Observation-based solar and wind power capacity factors and power densities (Environ. Res. Lett. (2018) 13 (104008) DOI: 10.1088/1748-9326/aae102),” *Environ. Res. Lett.*, vol. 14, no. 7, 2019, doi: 10.1088/1748-9326/ab12a2.

[21] D. Harrison-Atlas, A. Lopez, and E. Lantz, “Dynamic land use implications of rapidly expanding and evolving wind power deployment,” *Environ. Res. Lett.*, vol. 17, no. 4, p. 044064, 2022, doi: 10.1088/1748-9326/ac5f2c.

[22] National Renewable Energy Laboratory, “Annual Energy Baseline,” 2022. https://atb.nrel.gov/.

[23] P. Denholm, “NREL ’ s 100 % Clean Electricity by 2035 Study,” 2022.

[24] T. C. Brown, V. Mahat, and J. A. Ramirez, “Adaptation to Future Water Shortages in the United States Caused by Population Growth and Climate Change,” *Earth’s Futur.*, vol. 7, no. 3, pp. 219–234, 2019, doi: 10.1029/2018EF001091.

[25] P. Cui *et al.*, “Life cycle water footprint comparison of biomass-to-hydrogen and coal-to-hydrogen processes,” *Science of the Total Environment*, vol. 773. 2021, doi: 10.1016/j.scitotenv.2021.145056.

APPENDIX—CHAPTER 9

A link to the tabulated data used in the Energy Equity and Environmental Justice (EEEJ) chapter is available at https://roads2removal.org/. This appendix is meant to address the following:

1. Detail methods on the construction of the 'EEEJ indices' and 'EEEJ and SVI-weighted CDR indices'
2. Detail methods on the estimation of 'county job losses,' 'minority-owned cropland,' 'minority-owned woodland,' and 'minority-owned animal farm,' including listing data sources for each variable with links.

Methods for Index Construction

EEEJ Indices

The general process to calculate each chapter's EEEJ index is as follows:

1. Gather or calculate county-level data for each underlying variable in the EEEJ index.
2. Check each variable for normality using the Anderson Darling Normality test.
3. If the normality test fails, apply a Box-Cox transformation.
   3.1. In most cases, while the Box-Cox transformation still results in a distribution significantly different from the normal distribution, the resulting distribution is still closer to normal, and the transformation is kept.
4. Min–Max scale each resulting variable to a scale of 0–1.
   4.1. In cases for which high values for an underlying variable indicate lower EEEJ co-benefits, then the 0–1 values for this variable are reversed by subtracting each value from 1.
   4.2. For each underlying variable, values closer to 1 correlate with higher co-benefits opportunities, while values closer to 0 correlate with lower co-benefits opportunities.
5. Any counties with missing data in an underlying variable category are filled in with 0 for this variable (i.e., counties with missing data are assumed to have no co-benefits in this category).
6. Take the average across all processed underlying variables to calculate the overall EEEJ index.

EEEJ and Social Vulnerability Index-weighted CO_2 Removal Indices

Two types of overall CO_2 removal scores were calculated—protective and collaborative. The protective scores were designed to identify vulnerable counties where CO_2 removal could offer additional protective co-benefits. Northeast forests, western forests, and soils were calculated as protective indexes using the following formula:

$$Protective\ Index\ Score = EEEJ\ Average\ Index * CDR\ Metric * MAX(SVI, 0.6)$$

The collaborative scores were designed to identify lower-vulnerability collaborators where CO_2 removal would have less risk of disrupting an already vulnerable population. CO_2 removal should still be explored in vulnerable regions, but must be done so with great care to engage, empower, and get buy-in from the local communities. Southeastern forests, biomass carbon removal and storage (BiCRS), geologic storage, and DAC were all calculated as collaborative scores using the following formula:

$$Collaborative\ Index\ Score = EEEJ\ Average\ Index * CDR\ Metric * (1 - MAX(SVI - 0.6, 0))$$

In each case, a social vulnerability index (SVI) limit of 0.6 was used to prevent extremely low SVI values from skewing the data. Due to the different nature and different estimations of each CO_2 removal method, different CO_2 removal metrics were needed for each method:

- Forests: CO_2 removal per woodland area
- Soils: CO_2 removal per cropland area
- BiCRS: regional CO_2 removal capacity / regional cost, divided equally across counties in region
- Geologic storage: storage capacity per USD
- DAC:
  - Sorbent DAC: CO_2 removal capacity / cost
  - Solvent DAC: regional CO_2 removal capacity / regional cost, divided equally across counties in the region
  - Report the greater value between Sorbent and Solvent DAC for a single DAC index.

Since each method used a different CO_2 removal metric, each calculated score was min–max scaled from 0–1 within each method and used to rank the viability of each CO_2 removal method within each county. The min–max scaling was not done across CO_2 removal methods. Since all CO_2 removal technologies will have a part to play, this index isn't answering the question, "Which CO_2 removal technology is best overall?" but rather, "Which counties have substantial CO_2 removal opportunities in which technologies compared to the rest of the nation?"

Underlying Variable Data Gathering and Calculations

County Job Losses

Annual job losses were estimated in each county using the Census Quarterly Workforce Indicator (QWI) data for all states except Alaska; the Alaska data was taken separately from the Quarterly Census of Employment and Wages (QCEW).

https://qwiexplorer.ces.census.gov/#x=0&g=0

https://live.laborstats.alaska.gov/article/current-quarterly-census-employment-and-wages-qcew

The data were analyzed as follows for each industry in each county:

1. Calculate the average quarterly employment data for each year between 2015 and 2020.
2. For each entry with at least 3 years of employment data available, perform a linear regression on the yearly data. The slope of this regression equation estimates the number of jobs lost per year in each county and industry.
3. Ignore any entries that have $R^2 < 0.4$.
4. Divide the calculated slope by the total number of jobs in each county across all industries in 2015.
5. Any counties with positive slopes were labeled as having job increases. The extent of job increases was not considered for further numerical analysis.
   5.1. For the job losses EEEJ underlying index variables, counties with job increases were considered to have scores of 0 (i.e., no job losses).
   5.2. County job losses were calculated for the following NAICS industries: 23; 31-33; 56; 112; 113; 325; 321; 324; 332; 3233; 335; 325; 482; 484; 486; 2111; 2121; 2211County job losses were calculated for the following NAICS industries: 23; 31-33; 56; 112; 113; 325; 321; 324; 332; 3233; 335; 325; 482; 484; 486; 2111; 2121; 2211

Minority-owned Woodland

Percent of minority-owned woodland was taken from the USDA National Agriculture Statistics service:

https://quickstats.nass.usda.gov/results/E665EE7A-3BD1-33A6-91E7-00886A82504D

The percent of minority-owned woodland was calculated as 100 – percent of white-owned woodland. In some cases, the percent of white ownership was undisclosed (marked as '(D)' in the data). In these cases, 0% minority ownership was assumed.

Minority-owned Cropland

Percent of minority-owned cropland was taken from the USDA National Agriculture Statistics quick stats database: https://quickstats.nass.usda.gov/

Percent of minority cropland was calculated as follows:

1. From the Quickstats database, gather both total acres harvested and acres harvested by white owners for barley, corn, soybeans, sorghum, and wheat.
2. In some cases, the white ownership data was undisclosed (marked as '(D)' in the data). In these cases, it was assumed that all acres were harvested by white-owned enterprises.
3. Sum the total acres harvested across all types of crops for both the overall total and by white-owned enterprises.
4. Calculate the percentage of white-owned cropland as Total Acres Harvested / White-owned Acres Harvested
5. Calculate percent of minority-owned cropland as 100 – percentage of white-owned cropland

Minority-owned Animal Farms

Minority-owned animal farm data was taken from the USDA National Agriculture Statistics quick stats database: https://quickstats.nass.usda.gov/

It was estimated as the proportion of cattle + hogs heads owned by non-white enterprises. It was calculated as follows:

1. From the Quickstats database, gather the total and white-owned heads of cattle and heads of hogs.
   1.1. For cattle, the only commodity class description with disclosed racial demographic data was 'INCL CALVES'.
2. In some cases, the white ownership data was undisclosed (marked as '(D)' in the data). In these cases, it was assumed that all acres were harvested by white-owned enterprises.
3. Sum the total heads of hogs + cattle for both the overall total and by white-owned enterprises.
4. Calculate the percentage of white-owned cropland as Total Hogs + Cattle / White-owned Hogs + Cattle.
5. Calculate percent of minority-owned cropland as 100 – percentage of white-owned Hogs + Cattle.

Annual Average Excessive Smoke Days

To quantify each county's smoke exposure, we calculated how many days per year on average each county exceeded the EPA daily PM2.5 threshold of 35 micrograms per cubic meter of air (µg/m3). For all states excluding Alaska, we estimated this from this dataset:

https://www.dropbox.com/sh/wh45f4uf7gpb3ct/AADj0qBSaKUT9YUUjPrZifola/county/smokePM2pt5_predictions_daily_county_20060101-20201231.csv?dl=0

This dataset contains daily county-level, non-zero PM2.5 predictions due to wildfire from 2006 through 2020. We calculated the average days per year above the EPA threshold as follows:

- Fill each zero smoke day.
- Count the days above of 35 µg/m^3 for each county for each year.

- Average each year together to get the average days per year with air quality above 35 µg/m^3 due to wildfire smoke.

The Alaska data was calculated as follows:

Annual average number of days with $PM_{2.5}$ concentrations greater than 35 ug/m^3 in Alaska census areas are derived from simulated $PM_{2.5}$ concentrations from 2001 to 2015 between May and September (Chen et al. 2023). Concentrations outside of these months, and therefore outside of the typical fire season, are assumed to be 0 ug/m^3. Figures from the supplementary material of Chen et al. representing the simulated dataset contains colored pixels identifying the number of days with $PM_{2.5}$ concentrations greater than 35 ug/m^3 on a scale of 0, 1–5, 6–10, 11–15, 16–20, 21–30, 31–40, and greater than 40 days. The pixel color scale is converted to 0, 3, 8, 13, 18, 26, 36, and 50 days, respectively, for use in calculating the average number of days. Each year's map is then sub-divided by census area, and the average annual is calculated across the 15-year period. Some census areas are not included in the simulated dataset, and therefore, are not included in this calculation.

Water Consumption

Water consumption data was taken from the National Water Economy Database:

Rushforth, R., B. Ruddell (2018). National Water Economy Database, version 1.1, HydroShare, https://doi.org/10.4211/hs.84d1b8b60f274ba4be155881129561a9

From this data, we summed the total water consumed in each county (combining ground water and surface water).

Minority Business Index

The minority business index was calculated by taking the ratio of minority-owned business to the population of non-white residents. The goal was to highlight counties with a healthy ecosystem of diverse business ownership while reducing bias towards counties with inherently large non-white populations. The data come from two different census data sets. Business data comes from the Census's 2012 Survey of Business Owners (SBO), since this is the most recent dataset with county-level racial demographic business data:

https://www.census.gov/library/publications/2012/econ/2012-sbo.html

The population estimate data comes from the Census's 2019 Population Estimates Program:

https://www.census.gov/data/developers/data-sets/popest-popproj/popest.Vintage_2019.html#list-tab-2014455046

Small Business Index

The small business index was calculated as the number of small firms (firms with less than 100 employees) per total county employee. This metric was chosen over a seemingly more straightforward metric such as the ratio of small firms to total firms, since considering total employees in a county could better discern counties with a healthy ecosystem of small business versus counties where employment is dominated by large employers.

The data come from the Census's 2021 County Business Patterns (CBP):

https://www.census.gov/data/developers/data-sets/cbp-nonemp-zbp/cbp-api.html

County and Adjacent County Nitrogen Pollution

Adjacent counties were located using the Census County Adjacency file:

https://www.census.gov/geographies/reference-files/time-series/geo/county-adjacency.html

For each county, the maximum nitrogen pollution of any adjacent county was reported. For counties with no adjacent counties, or counties with data missing from the County Adjacency files, null data was reported, so neither case would penalize the overall EEEJ index value.

County Glyphosate Pollution

County resolution glyphosate data were sourced from the US Geologic Survey at:

https://www.sciencebase.gov/catalog/item/6081a924d34e8564d68661a1

County Nitrogen Leaching Reduction Potential

We sampled a total of 37,283 cropland sites from across 2057 cropland-containing counties to model representative biogeochemical responses to cropland management practices. Using the DayCent biogeochemical model, we modeled mineral nitrogen leaching combined in baseflow and runoff in each site both with the practice (cover crops, carbon crops, or field borders) implemented, and without the practice (baseline crop rotation). DayCent calculates mineral nitrogen leaching based on nitrogen inputs, water inputs, and soil hydraulic conductivity between each soil layer, as a function of soil texture. We subtracted total cumulative nitrogen leaching given the new practice from total cumulative nitrogen leaching in the counterfactual scenario from 2025 through 2050 to calculate a per-area, cumulative reduction in nitrogen leaching under each new practice, for each site.

Public Land Percentage

The Surface Management Area (SMA) dataset, from the US Bureau of Land Management, was downloaded here:

https://gbp-blm-egis.hub.arcgis.com/datasets/blm-national-sma-surface-management-agency-area-polygons/about

"Public land" was classified as the summation of all data layers in the GIS downloadable file (e.g., SurfaceMgtAgy_FWS, SurfaceMgtAgy_BLM, etc.), except for 'SurfaceMgtAgy_PRIUNK,' which refers to private and/or unclassified lands; county-resolution percentages of public land were calculated with ArcGIS.

Burn Probability Index

Right before this report was published, a 2023 update to the USDA's Burn Probability Index was published, but this was too late for this report to incorporate. Future projects building upon these efforts should use the more updated dataset. However, data downloaded from the USDA's Research Data Archive and used for the report is available here (Short et al., 2016):

https://www.fs.usda.gov/rds/archive/Catalog/RDS-2016-0034

Soil Erodibility

The soil erodibility data was calculated from Figure S7-B of Shojaeezadeh et al., 2020: "Soil Erosion in the United States." Their figure was based on POLARIS : a 30-meter probabilistic soil series map of the contiguous United States, available here :

https://pubs.usgs.gov/publication/70170912

Figure S7-B in Shojaeezadeh et al. (preprint; https://doi.org/10.48550/arXiv.2207.06579), based on the POLARIS model, was graphically translated into data ranges using the color-coded legend, then averages

were calculated to yield county resolution, average soil erodibility values across the contiguous United States.

Average Farm Net Income

Average farm net income data was downloaded from the USDA National Agriculture Statistics quick stats database:

https://quickstats.nass.usda.gov/

Nitrogen Loading Data

County resolution data for total nitrogen and phosphorous loading, derived from manure and from fertilizer, was derived from this USGS database:

https://www.sciencebase.gov/catalog/item/5ebad56382ce25b51361806a

In the construction of the 'eutrophication risk' and 'contiguous nitrogen pollution' variable construction for the EEEJ indices, we opted to use the sum of (farmfertN-kg-2017, nonffertN-kg-2017) in file N-P_from_fertilizer_1950-2017-july23-2020 and (Total_N_kg-2017) in N-P_from_manure_1950-2017-july23-2020 to reflect the overall water quality risks that counties face from nutrient loading, regardless of agricultural source.

Population and Population Density Data

County resolution population data were sourced from the most recent US Census available (2022) here:

https://www.census.gov/data/tables/time-series/demo/popest/2020s-counties-detail.html

PM2.5 from Cropland and Rangeland Burning Data

County resolution data were requested from the lead author of Pouliot et al., 2017; publication available here:

https://www.tandfonline.com/doi/full/10.1080/10962247.2016.1268982

Premature Deaths Avoided by Long Haul Truck and Rail Freight Decarbonization

County resolution data were requested via email from Dr. Shuai Pan, lead author of the study that evaluated potentially avoidable premature deaths from diesel-derived PM2.5 through decarbonization of the freight industry (long-haul trucking and rail). Paper available here:

https://www.sciencedirect.com/science/article/pii/S0160412019300376

Publicly Owned Forestland

County resolution forest ownership data was access in Sass et al., 2020, here:

https://www.fs.usda.gov/rds/archive/catalog/RDS-2020-0044

To calculate the percentage of a county's publicly owned forestland, we summed: 'Percent_Tribal,' 'Percent_Local,' Percent_State,' and 'Percent_Federal,' then divided by 'Total_Forest' to yield a percentage value.

A correlation matrix of all variables analyzed in this chapter is provided below for the reader to assess potential correlations (positive or negative) between variables, including the CDC's SVI and CO_2 removal opportunity calculations.

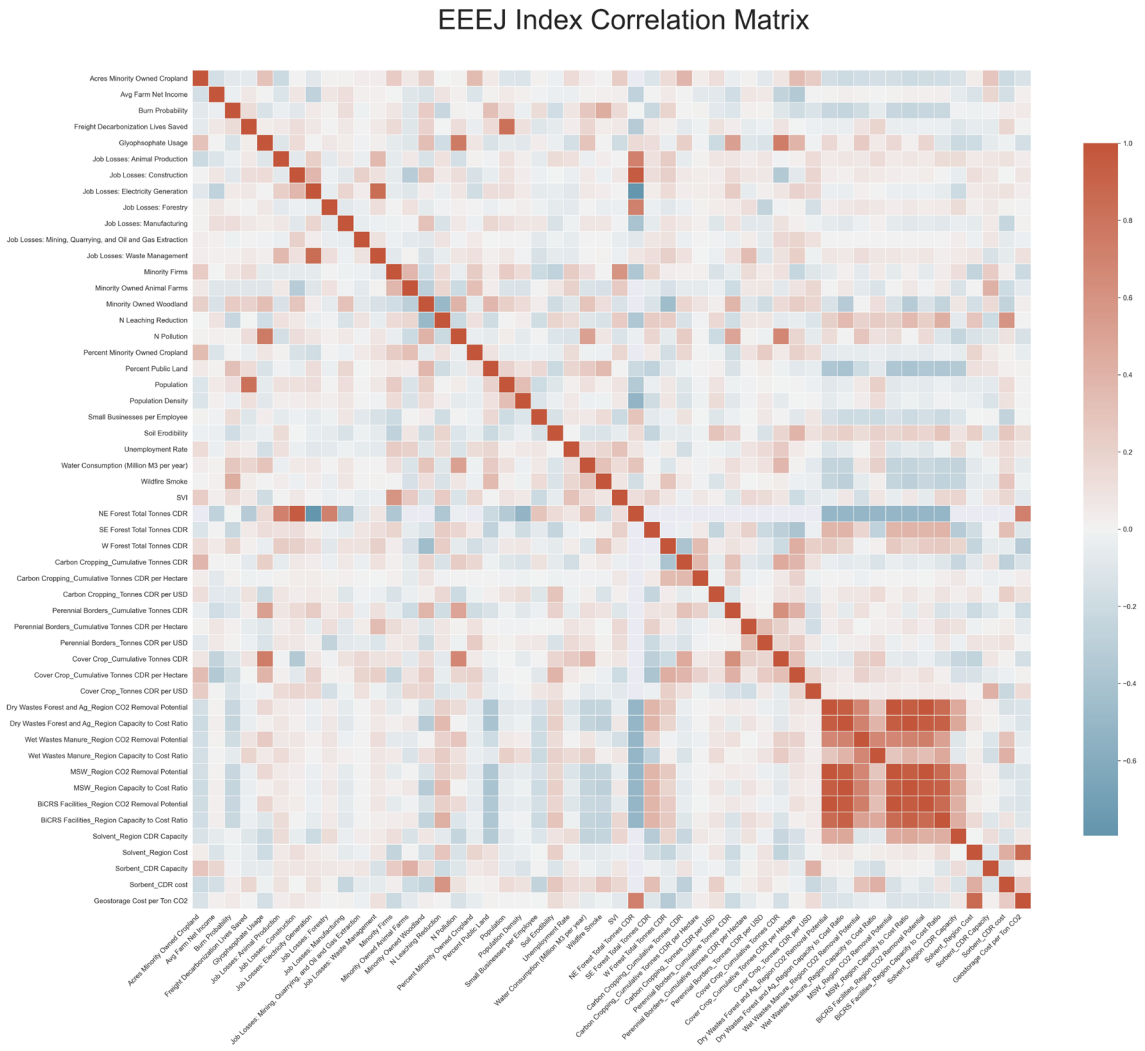

Figure A9-1 *Correlation matrix of every county-organized variable included in the EEEJ Indices constructed in this report, as well as CO_2 removal potential and SVI. Negative values (blue) represent an inverse correlation and positive values (red) represent a positive correlation.*

APPENDIX—CHAPTER 10

This paper intentionally left blank.